Doctoral theses at NTNU, 2023:40

Iman Taji

Hydrogen embrittlement and corrosion evaluation of Alloy 725 alloyed with B and Cu

Doctoral thesis

NTNU
Norwegian University of Science and Technology
Thesis for the Degree of Philosophiae Doctor
Faculty of Engineering
Department of Mechanical and Industrial Engineering

NTNU
Norwegian University of Science and Technology

Iman Taji

Hydrogen embrittlement and corrosion evaluation of Alloy 725 alloyed with B and Cu

Thesis for the Degree of Philosophiae Doctor

Trondheim, February 2023

Norwegian University of Science and Technology
Faculty of Engineering
Department of Mechanical and Industrial Engineering

NTNU
Norwegian University of
Science and Technology

NTNU
Norwegian University of Science and Technology

Thesis for the Degree of Philosophiae Doctor

Faculty of Engineering
Department of Mechanical and Industrial Engineering

ISBN 978-82-326-6371-2 (printed ver.)
ISBN 978-82-326-5952-4 (electronic ver.)
ISSN 1503-8181 (printed ver.)
ISSN 2703-8084 (online ver.)

Doctoral theses at NTNU, 2023:40

Printed by NTNU Grafisk senter

Preface

This thesis is submitted to the Norwegian University of Science and Technology (NTNU) for partial fulfillment of the requirements for the degree of *Philosophiae Doctor*.

The Ph.D work was carried out from November 2018 to April 2022 at the department of Mechanical and Industrial Engineering under supervision of Professor Afrooz Barnoush (until January 2020) and Professor Roy Johnsen. Dr. Tarlan Hajilou was appointed as a co-supervisor in this work.

This work has been done under the scope of the COMET program within the K2 Center "Integrated Computational Material, Process and Product Engineering (IC-MPPE), Astria" (Project No. 859480). This program is supported by Equinor, Norway and Voestalpine BÖHLER Edelstahl GmbH & Co KG, the Austrian Federal Ministries for Climate Action, Environment, Energy, Mobility, Innovation and Technology (BMK) and for Digital and Economic Affairs (BMDW), represented by the Austrian Research Funding Association (FFG), and the federal states of Styria, Upper Austria, and Tyrol. The computational results presented have been obtained using the Vienna Scientific Cluster (VSC). The Research Council of Norway is acknowledged for the support to the Norwegian Micro- and Nano-Fabrication Facility, NorFab, Norway (Project No. 245963/F50).

Abstract

The need to achieve materials with higher strength and better corrosion resistance results in producing new alloys. Nickel base alloys are among the materials which have been subjected to several studies related to producing new alloys. Nickel based superalloys, in particular, drew a lot of attention. Nickel superalloys are durable materials in mechanical loadings while having good performance against corrosive media, simultaneously.

In this work the effect of heat treatment and chemical alloying with boron and copper on hydrogen embrittlement (HE) and corrosion resistance have been investigated. The role of sulfur segregation at grain boundaries (GB) on HE of nickel is also studied. HE studies have been done in micro-scale by in-situ electrochemical micro-cantilever bending test. The cantilevers made either inside the grains to investigate the role of alloying elements and precipitates on HE, or on two grains to study the effect of GBs on the HE.

By heat treatment of Alloy 725 in three conditions, the different effects of GB on HE is studied. One sample is solution annealed (SA) in order to remove the effect of any precipitates, another sample is aged (AG) based on the heat-treatment standard guideline normally used in industries and the last sample is over-aged (OA) to reach coarser precipitates. All the single-crystal cantilevers were made on three samples which were cracked under the H-charging condition, however, crack propagation was more severe in the OA sample. Bi-crystal micro-cantilevers bent under H-free and H-charged conditions revealed the significant role of the GB in the HE of the beams. The results indicated that the GB in the SA sample facilitated dislocation dissipation, whereas for the OA sample, it caused the retardation of crack propagation. For the AG sample, testing in an H-containing environment led to the formation of a sharp, severe crack along the GB path.

The effect of boron and copper alloying on HE is also investigated in this thesis. Three samples were used. The standard Alloy 725 (Mod A) was used as a control group, comparing with the one alloyed with 250-350 wt%.ppm B (Mod B) and <100 wt%.ppm B + 2.3 wt% Cu (Mod C). Cross-sectional view of the bent beams taken by scanning electron microscopy (SEM) showed the superior resistance of Mod B against HE by facilitating the GB dislocation transfer/generation. While bending Mod A sample in hydrogen environment leads to form a sharp intergranular cracking, Mod B showed some nano-voids/cracks mostly in dislocation

slip bands and rarely in GB path. However, a reduction of strength was observed in load-displacement (L-D) curves of Mod B. The addition of Cu, although not participated in GB segregation, compromised the lost strength of Mod B. In Mod C, after bending in H-charged condition, the nano-voids were formed in GB, but no load drop in L-D curves nor crack propagation in post-deformation observations was detected. The micro-alloying proposed in this study could be an important contribution to the future developing of H resistant alloys via GB segregation engineering.

Sulfur is among the elements that have a detrimental effect on the mechanical properties of the metals if segregated at the GBs. The effect of co-segregation of S and H is investigated in this thesis on pure Ni. A pure Ni GB shows completely plastic behavior with no fracture observed in the experiments. Electrochemical H-charging of the sample with no S present in the GB leads to a crack formed at the notch tip, which propagates by means of the mixed plastic–brittle fracture mode. Cantilever testing of the H-charged GB with S results in a clear brittle fracture of the GB. The co-segregation of S and H shifts the sudden drop in the load–displacement curves to smaller values of displacement.

Finally, intergranular corrosion passive layer properties of Mod A, B and C is investigated in this thesis. Intergranular corrosion test showed continuous corrosion at the GB in Mod A while Mod C remains completely intact without any corrosion attack. Mod B corroded in the areas around the Mo-rich boride phases formed due to abundant of B element in this alloy. Mod C showed the least defect density in the passive layer while the passive layer of Mod B thicker. The incorporation of Mo in Mod C was proposed to be the responsible for less defect density of Mod C compared to Mod B. Mod A on the other hand had the most defect density and shows higher passive current density in potentiodynamic polarization test.

Acknowledgement

First, I would like to express my deep gratitude to Professor Afrooz Barnoush who gave me the opportunity to perform this PhD. I believe that it is blessed for any researcher to have Afrooz beside. I am grateful to had him during part of my PhD and it is a pity that I lost him almost half of it.

I should thank Professor Roy Johnsen, my supervisor, for his kind support within the hardest days that I experienced during my PhD.

Finishing my PhD would not be possible without having my friend and co-supervisor Dr. Tarlan Hajilou who totally dedicated herself to help me during this journey.

I was lucky to have such a good friend and colleague, Shabnam Karimi, beside me. Being together helped me to pass dark, chaotic, and stressful days in which no one bothers him/herself to be alongside me.

I appreciate Professor Mariano Iannuzzi and Dr. Sofia Hazarabedian for their kind generosity to provide their results of intergranular corrosion tests before publishing them.

I also thank all my co-authors in the published papers, especially Professor Vsevolod Razumovskiy, Dr. Anna Sophie Ebner, Dr. Daniel Scheiber, Dr. Shuang He, Dr. Ernst Plesiutschnig and Florian Schott for their contribution and fruitful discussion.

Table of Contents

Preface I
Abstract II
Acknowledgement IV
List of Figures VII
List of Tables VIII
Nomenclature IX
1 Introduction and Methods 1
1.1 Motivation for this study 1
1.2 Research objectives 2
1.3 Nickel Superalloys 3
1.4 Influence of minor alloying addition 3
1.5 Hydrogen uptake in metals 4
1.6 Hydrogen diffusion 6
1.7 Hydrogen Embrittlement mechanisms 7
1.7.1 Hydride formation 7
1.7.2 Hydrogen-enhanced decohesion 8
1.7.3 Hydrogen-enhanced localized plasticity 8
1.8 Hydrogen Embrittlement of Nickel superalloys 8
1.9 Small scale HE studies 9
1.10 Corrosion of Nickel superalloys 10
1.11 Intergranular corrosion 10
1.12 Materials 11
1.13 Micro-cantilever fabrication 11
1.14 X-ray photo-electron spectroscopy 16
1.15 Intergranular corrosion testing 17
1.16 Thermal desorption spectroscopy 17
1.17 List of publications and contributions 19
1.18 Summary of papers 24
2 Recommendations and Future works 29
2.1 The effect of GB type 29
2.2 Formation of Ni-hydride 29
2.3 In-situ stress corrosion cracking by micro-cantilever bending 30
3 Appended papers 35
Paper I: Role of Grain Boundaries in Hydrogen Embrittlement of Alloy 725: Single and Bi-Crystal Microcantilever Bending Study 36
Paper II: Hydrogen Assisted Intergranular Cracking of Alloy 725: The Effect of Boron and Copper Alloying 48

Paper III: Hydrogen-enhanced intergranular failure of sulfur-doped nickel grain boundary: In situ electrochemical micro-cantilever bending vs. DFT 63
Paper IV: Intergranular Corrosion and Passive Layer Properties of Alloy 725 Modified with Boron and Copper Micro-alloying 78

List of Figures

Figure 1.1. subsurface safety valve assembly (left) and the fracture surface (right) [4]. 2
Figure 1.2. Schematic representation of hydrogen generation and entry into the metal from an aqueous environment. 5
Figure 1.3. Trapping sites of H in metallic materials [15]. 6
Figure 1.4. Hydrogen diffusion coefficients for BCC (Fe and Nb), FCC (Ni) and HCP (Ti) pure metals [16]. 6
Figure 1.5. Schematic diagram of fracture mechanism in presence of hydride [16]. 7
Figure 1.6. EBSD micrograph of the AG sample. The arrow shows a selected GB for bi-crystal milling. 12
Figure 1.7. A series of cantilevers milled out on a selected GB depicted in Fig. 1.1 (left). The dimensions of a bi-crystal cantilever (right). 13
Figure 1.8. A clear GB which on a milled bi-crystal cantilever (left). A notch milled on the GB in a bi-crystal cantilever (right). 13
Figure 1.9. In situ test set up in the nanoindenter chamber. 14
Figure 1.10. A schematic of the in-situ testing cell. 15
Figure 1.11. Post-deformation SEM image of a cantilever bent in H-charging condition. 15
Figure 1.12. Platinum coating of a bent cantilever to protect against further using of Ga-beam of FIB. The material presented here is a high carbon steel. 16

List of Tables

Table 1.1. Material used in this study. 11

Nomenclature

AG	Aged heat treatment
APT	Atom prob tomography
DFT	Density functional theory
DL-EPR	Double loop electrochemical potentiokinetic reactivation
DSB	Dislocation slip band
EBSD	Electron backscattered diffraction
FCC	Face centered cubic
FIB	Focus ion beam
GB	Grain boundary
HAGB	High angle grain boundary
HE	Hydrogen embrittlement
HEDE	Hydrogen-enhanced decohesion
HELP	Hydrogen-enhanced localized plasticity
KAM	Kernel average misorientation
L-D	load-displacement curves
MS	Mott-Schottky
NBS	Nickel-based superalloy
OA	Over-aged heat treatment
OCP	Open circuit potential
SA	Solution-annealed heat treatment
SEM	Scanning electron microscopy
TCP	Topologically close packed
TDS	Thermal desorption spectroscopy
TEM	Transmission electron microscopy
TKD	Transmission Kikuchi diffraction
XPS	X-ray photoelectron spectroscopy

1 Introduction and Methods

1.1 Motivation for this study

Failures due to corrosion and hydrogen embrittlement (HE) are among the biggest issues in industries which works in harsh environments. For example, some of the failures in oil and gas industries are not only costly but also they can be associated with severe consequence to human life and environment. Nickel superalloys which were firstly developed for high-temperature aerospace applications, and soon introduced into the oil and gas industry in early 1980s [1]. In these environments the material experiences high pressure and high temperature alongside highly acidic environment containing H_2S, CO_2 and chloride ions. For example, deep well environments contain more that 10% H_2S and the temperature exceeding 200 °C. Nickel superalloys are typically used as rods, production tubing, valves, landing nipples and tool joints in oil and gas industries. These alloys are expected to work for about 20 years in such environments [2]. Therefore, they should have a high resistance against corrosion and HE to be appropriate for oil and gas industries application.

However, there are reports which shows that microstructural features cause unexpected failures in nickel superalloy components. For instance, failure of an Alloy 725 seal used in subsea equipment has been observed and attributed to the formation of a brittle phase in grain boundaries [3]. A failure of a subsurface safety valve made of Alloy 716 is reported which is caused by intergranular HE as can be seen in Fig. 1.1 [4]. Other failures of tubular crossover on Alloy 725, casing and tubing hanger on Alloy 718 are also reported in the literature [5]. In most of the cases the root of the failure was detected to be some phases which is precipitated in grain boundaries (GBs).

Since the introduction of nickel superalloys in oil and gas industries, several modifications have been made to improve their mechanical and corrosion properties. In this thesis the effect of some alloying elements such as B and Cu on the HE and corrosion properties of the produced material will be investigated. Most part of this study focuses on GBs and intergranular properties of the materials. GBs are responsible for most of the failures and exploring their properties would help to understand the failure mechanism which can be useful to produce more resistant materials.

Figure 1.1. Subsurface safety valve assembly (left) and the fracture surface (right) [4].

1.2 Research objectives

This work mainly deals with the role of the GBs in HE and corrosion properties of Ni-superalloys. Therefore, micro cantilevers which contain GBs were produced and tested to be compared with ones that do not have GBs. In addition, the beneficial or detrimental effect of some GB precipitates was also investigated. The main objectives of the theses are as follows:

Chapter 2: Investigating the role of GBs in HE of Ni-superalloy. How can a GB affect the HE of the Alloy 725. Is the presence of GBs beneficial or deleterious? By using three different heat treatments, the effect of three different GBs on bi-crystal micro-cantilevers were investigated and compared with similar microcantilevers but without GB.

Chapter 3: Study of GB HE of Ni-superalloy modified with B and Cu. How does addition of minor alloying elements influence the HE properties? This part focused on the GBs to show how GB segregation changes the HE response of the material. B as a

GB modifier and Cu as a solid solution strengthening element were investigated in this chapter.

Chapter 4: Investigating the role of sulfur segregation on the HE of pure Ni. In this work, pure Ni was used. Single- and bi-crystal cantilevers were compared and the effect of GB segregated sulfur as a detrimental element was studied.

Chapter 5: Examinating how the GB precipitates influence the corrosion properties. Unlike previous parts which was related to the HE, this part pertained to the corrosion response of the superalloys which were modified with B and Cu. The total corrosion response and the passive layer properties as well as their intergranular corrosion resistance were the subjects of study in this chapter.

1.3 Nickel Superalloys

Nickel superalloys, in general, contain more than 50% alloying elements mostly from VIIIA elements in the periodic table [6]. The face centered cubic (FCC) structure of the alloy allows the material to have excellent ductility, malleability, and formability. Nickel super alloys are normally alloyed with high amount of Cr which tends to have a high corrosion resistance ability. The combination of good corrosion resistance and high mechanical properties make these materials favorable in different industries. They can be used in high and low temperature applications with harsh corrosive environment like oil and gas environment.

1.4 Influence of minor alloying addition

Different alloying elements have been used to modify the superalloys properties. Alloying elements in nickel superalloys can have several effects which can be categorized as follows [7]:

- Precipitate former alloying elements like: Al, Ti, Ta and Nb.
- Solid solution strengtheners like: Re, W and Ta.
- Grain boundary refiner: B, C and Hf.
- Enhancement of corrosion and oxidation resistance: Cr, Mo and Al.

Alloy 725 or Inconel 725, in particular, is a precipitation hardened alloy in which Cr, Mo, Fe, Nb and Ti are the main alloying elements. The microstructure of this alloy consists of the

solid-solutioned Ni matrix which is strengthened by the coherent intermetallic precipitations of γ'-Ni_3 (Ti,Al) and γ''-Ni_3(Nb).

In addition to the γ' and γ'', there are different phases that can be formed in superalloys. Among these phases are carbides that need especial attention. Carbon tends to form metallic carbides in form of $M_{23}C_6$ at the grain boundaries which M denotes Cr or Mo elements. Precipitation of such carbides might be beneficial in high temperature creep processes which need GB stabilization. However, formation of Cr or Mo rich phases at the GBs can result in impoverishment of these alloying elements in adjacent areas around the GB. Therefore, especially for the case of Cr shortage at the adjacent area of GBs it can lead to poor passive layer formation and hence raising intergranular corrosion risk.

For ambient temperature applications, on the other hand, the presence of carbide in GBs can be an initiation sites for cracking under loading conditions.

B is reported to be able to prevent the formation of large and continuous GB carbides [8]. It can also increase the GB cohesive energy [9]. Therefore, this element has been used in Ni-superalloys [10], steels [11], and other materials [12] to improve the ductility.

Cu is a corrosion resistant material in nonoxidizing solutions of mineral acids such as sulfuric, hydrochloric phosphoric, or hydrofluoric acid [13]. Cu has been used for different nickel superalloys such as Alloys 200, 825 and 925 to improve their corrosion resistance. Due to copper alloying with the content of around 2 wt%, Alloy 825 and 925 make them appropriate to for components to be used in sulfuric acid pickling of steel and copper, components in petroleum refineries and petrochemicals (tanks, agitators, valves, pumps), equipment used in production of ammonium sulfate, pollution control equipment, oil and gas recovery, acid production and phosphoric acid production (evaporators, cylinders, heat exchangers, equipment for handling fluorosilicic acid solution, and many others) [14].

1.5 Hydrogen uptake in metals

Hydrogen is the smallest atom in the periodic table. It has strong chemical activity and high lattice mobility which can be absorbed into the metal in H_2 gas environment or as a product of electrochemical reactions. H can be provided from different sources such as acid cleaning solutions, electroplating, corrosion processes and cathodic protection. It can also come from the high-pressure gaseous hydrogen containers or pipelines. In this work the H uptake from electrolytes will be investigated. In electrolytes, H can be produced via cathodic reaction of hydrogen reduction as follows:

$H_3O^+ + e^- \rightarrow H_{ads} + H_2O$ (1) Volmer reaction in acidic environments and

$H_2O + e^- \rightarrow H_{ads} + OH^-$ (2) Volmer reaction in neutral environments.

The produced H_{ads} on the metal surface can be either reacted with another adsorbed H to form a H_2 bubble and finally desorbed with following reactions:

$H_{ads} + H_{ads} \rightarrow H_2$ (3) (Tafel reaction)

$H_{ads} + H_3O^+ + e^- \rightarrow H_2 + H_2O$ (4) (Heyrovsky reaction)

or it can be absorbed into the metal:

$H_{ads} \rightarrow H_{abs}$. (5)

Fig. 1.2 shows the possible reactions incorporated in hydrogen generation and entry into the metallic substrate from an aqueous environment.

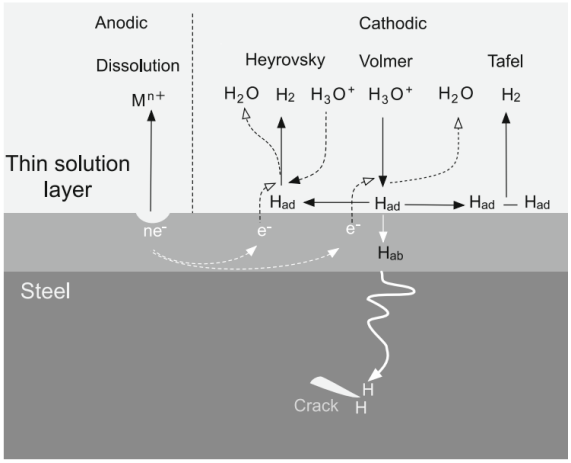

Figure 1.2. Schematic representation of hydrogen generation and entry into the metal from an aqueous environment.

The absorbed H, due to its small atomic radii will diffuse in the metal substrate and placed in octahedral and tetrahedral vacant parts of the metal. It can also enter the defects of the metal such as vacancies, dislocations, grain boundaries and interfaces. A schematic diagram in Fig. 1.3 shows some of the sites which H can be trapped in.

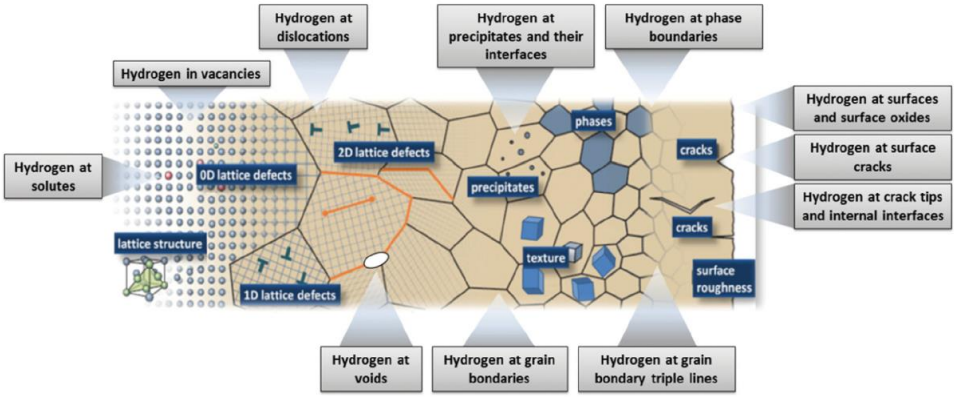

Figure 1.3. Trapping sites of H in metallic materials [15].

1.6 Hydrogen diffusion

The rate of H diffusion in pure metals depends on the crystal structure. The H diffusion coefficient, *D* is about 4 to 5 orders of magnitude higher for body centered cubic (BCC) materials in comparison with FCC and hexagonal closed packed (HCP) metals in ambient temperature. The diffusion coefficient for some metals is depicted in Fig. 1.4.

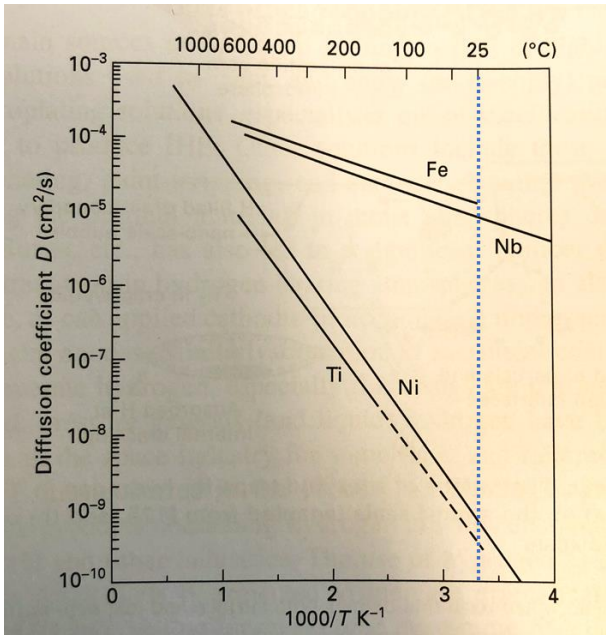

Figure 1.4. Hydrogen diffusion coefficients for BCC (Fe and Nb), FCC (Ni) and HCP (Ti) pure metals [16].

There are a number of parameters which can affect the *D*. *D* is increasing with temperature as can be seen clearly in Fig. 1.4. Closed pack structure has stronger dependency on

temperature. It also depends on the stress field, the presence of dislocations, vacancies, discontinuities, precipitates, and any microstructural features which can play role in trapping the H and changing the diffusion coefficient. For example, it is reported that the random high angle GBs accelerate the hydrogen diffusion while low misorientation or special GBs mitigate it [17].

1.7 Hydrogen Embrittlement mechanisms

The presence of absorbed H in the material cause embrittlement. Different mechanisms have been proposed to account for HE.

1.7.1 Hydride formation

In certain materials such as V, Zr, Nb, Ta and Ti there is a strong thermodynamic driving force for hydride formation. Since hydrides phases are brittle, the presence of these phases at the head of the crack enhances the possibility of brittle fracture. In hydride mechanism, first H diffuses to regions of high hydrostatic stress ahead of the crack which resulted in nucleation and growth of hydride phase. At the final stage, as depicted in Fig. 1.5, a cleavage crack will form when hydride reaches to a critical size. The crack will further arrest and experience blunting at the hydride-matrix interface.

The formation of hydride is also reported in alloys which are thermodynamically unfavorable. For example, on the conditions of high activity of H, hydride formation would be possible [18]. These NiH phases are unstable phase, but they might have irreversible impact on mechanical properties. Hydride can act as a barrier to dislocation motion. Therefore a dislocation pile up can be formed behind it and even if the hydride phase reverts to Ni, the remaining high dislocation density caucuses hardening which contribute in more brittle fracture [19].

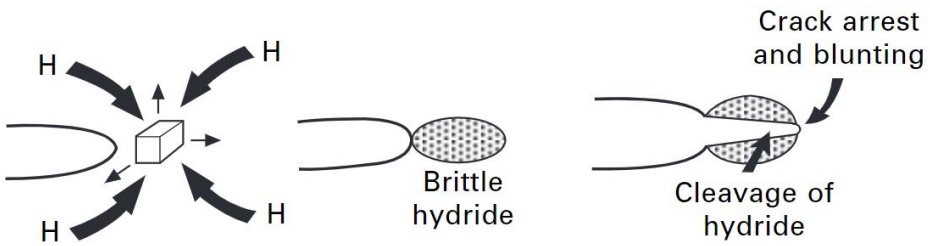

Figure 1.5. Schematic diagram of fracture mechanism in presence of hydride [16].

1.7.2 Hydrogen-enhanced decohesion

One of the famous mechanisms of HE is H-enhanced decohesion (HEDE) mechanism. According to this model the bounding strength between metal atoms will be reduced by dilatation of the atomic lattice when hydrogen accumulates in the lattice. Therefore, debonding of the atoms at the head of a crack or a position with maximum stress concentration takes place easier [20]. This mechanism is more pronounced in high strength materials and under high H concentration. This role of this mechanism is more evident in GBs and particle-matrix interfaces. Direct experimental evidence of HEDE mechanism is difficult to obtain but density functional theory (DFT) calculation, recently, well explained the contribution of this mechanism in HE. DFT calculations showed that the segregation of H in GBs and interfaces, greatly decrease the work required for interface separation [21].

1.7.3 Hydrogen-enhanced localized plasticity

H-enhanced localized plasticity (HELP) is also one of the popular mechanisms discussed in literature [22]. In this model, the accommodation of H at dislocations reduces the stress limit for which dislocations can move. Therefore, dislocations can reach the crack head easier make the crack propagate with localized shear and ductile rupture processes ahead of the crack. The mobilization of dislocations by H is directly observed by transmission electron microscopy studies [23]. The activation of dislocations by H, based on this theory leads to material softening [24]. However, the opposite conclusion has also been published in literature. It is reported that the accumulation of H induce dislocation pining effect which is lead to hardening [25, 26].

There are other mechanisms which can be found in literature. For example, Kirchheim [27] based on thermodynamics calculations proposed that H reduces the formations energy of defects. According to this theory H, as a defactant, segregates to defects, such as vacancies, dislocations and kinks in dislocation lines and void or crack surfaces and lower the defect formation energy according to the generalized Gibbs adsorption isotherm.

However, it should be noted that the HE of the materials, depending on the microstructure, loading condition and environment can be explained by different mechanism which sometimes act all together [20].

1.8 Hydrogen Embrittlement of Nickel superalloys

Embrittling effect of hydrogen on steels were first recognized in 1874 by William Johnson reported in a proceeding of the Royal Society of London [28]. Apart from corrosion effects,

he observed the mechanical degradation of the material by exposing to an acidic environment. The research on the hydrogen embrittlement (HE) were continued extensively afterwards to elucidate its mechanism of action and to evaluate possible mitigation methods. The application of superalloys in hydrogen-bearing environments, motivate researchers to invest in HE studies. However, the complicated structure of these alloys makes the research in this field challenging. Various parameters should be taken into consideration regarding HE of nickel superalloys:

- Nickel based alloys are FCC alloys and the diffusion coefficient of H in FCC alloys are several orders of magnitude lower than that in the body centered cubic (BCC) materials.
- The solubility of H in FCC metals is allegedly higher than in BCC metals.
- Presence of significant amount of solid solution in nickel superalloys is another important issue which can affect both diffusion and solubility of H. For example, the H diffusivity of Alloy 600 (74Ni15Cr9Fe) in the solution annealed form is reported to be 5 times lower than that for pure nickel [29].
- The presence of different type of precipitates in the age-hardened nickel superalloys affect the HE significantly.
- In addition, GBs make the situation more complicated. The interaction of GBs with H has long been evaluated in the literature [30]. However, depending on the specific system under study, the effect can be different.

Therefore, the mechanism-based study on the integration of H with such a complicated structure is hard to achieve. Large scale mechanical testing, in particular, suffers from the lack of separating multiple parameters that affect the mechanical response of the material simultaneously. As a result, confining the testing volume to micro-size specimens can really help to reduce the affecting parameters, in order to elucidate the role of microstructural parameters on the total mechanical performance.

1.9 Small scale HE studies

Since 1980s onward, the development of sophisticated instrumented indentation methods alongside with enhancing the electronic industry to produce highly accurate sensors lead to improvement in the micro mechanical testing area [31]. Especially, the measurement of the indentation load, P, combined with the penetration depth, h, was made possible. This advancement enables researchers to investigate the surface effects of H on the metals. Further development of microscopy methods and also the introduction of focused ion beam (FIB) for

micro milling, was the commencement of significant progress in this field. Using FIB provides the possibility of milling favorable geometrical micro scale shapes in order to do mechanical testing with the help of nanoindenter [32]. Micro-cantilever bending test is one of the most interesting methods used in this field. The first use of micro cantilever mechanical testing was reported in 2005 [33, 34]. Afterwards, it has been used in several applications to investigate the mechanism of mechanical behavior of materials in micro scale. In this regard, understanding the role GBs, dislocations, and different kind of precipitates play in mechanical responses of the materials became possible [32, 35, 36]. In addition, combining an electrochemical cell with the nanoindenter enables in situ testing over the milled micro cantilevers [25, 37]. The conventional three electrode set up helps to control the potential and current. Therefore, H charging would be possible before and during the mechanical testing.

1.10 Corrosion of Nickel superalloys

Depending on the alloying elements of the nickel superalloy, the corrosion properties could be different. Ni-Cr-Mo alloys are normally considered as the most corrosion resistant. Alloy 725, in particular, has a high durability against general corrosion and excellent resistance to pitting and crevice corrosion in chloride environments and acid media. The application of Alloy 725 has been qualified for sour service in oil and gas by NACE and ISO standards and the limiting temperature suggested is 220 °C and 2000 kPa of partial pressure of H_2S [38]. However, on the condition that Cr- or Mo-rich phases forms at the GBs there is a risk of intergranular corrosion.

1.11 Intergranular corrosion

Despite the superior corrosion resistance of nickel superalloys, some cases of intergranular corrosion have been reported [39-41]. Although there are chemical methods to compare the intergranular corrosion susceptibility of nickel based alloys [42], they are not designed to quantitatively evaluate intergranular corrosion and in some cases are hard to carry out and time consuming. Since the introduction of double loop electrochemical potentiokinetic reactivation (DL-EPR) test [43], the test has been increasingly used as a quantitative method for evaluating intergranular corrosion. However, the problem with this test is that it needs specific electrolyte for each material. The standard solution [44] is only applicable for austenitic stainless steels (SSs) and for other materials the solution should be modified [45].

1.12 Materials

Generally, seven different materials are used in this study which are listed in Table 1.1.

Table 1.1. Material used in this study.

Material ID	Specification	
Ni	Pure nickel (99.99%). Vacuum annealing at 1250 °C for 72 h.	
NiS	Pure nickel with additional 5.4 wt% ppm S.	
AG (Mod A)	Chemical composition wt.%	Cr: 19.7, Fe: 10.1, Mo: 7.3, Nb: 3.6, Ti:1.4, Mn<0.02, C<0.01, S<0.001
	Heat Treatment	solution annealing: 1038 °C for 2h, water quenching, aging at 732 °C for 8 hours, cooling in furnace down to 621 °C keeping for 8 h.
SA	Chemical composition similar to AG sample. Solution annealed at 1038 °C for 2h	
OA	Chemical composition similar to AG sample. 1038 °C for 2h, water quenching, aging at 780 °C for 8 hours, cooling in furnace down to 621 °C keeping for 8 h.	
Mod B	Chemical composition and heat treatment similar to Mod A plus adding 250 to 350 wt.ppm B.	
Mod C	Chemical composition and heat treatment similar to Mod A plus adding 2.3 wt.% Cu plus 100 wt.ppm B.	

1.13 Micro-cantilever fabrication

In the following, a step-by-step procedure of the cantilever milling and in-situ microcantilever testing used in this study will be introduced.

I. Sample surface preparation

The samples were prepared in discs with 10 mm diameter and 8 mm thickness. The samples, for the purpose of Electron Backscatter Scanning Diffraction (EBSD) analysis and micro cantilever milling, were grounded with emery paper up to grit number 2000 and then electropolished using 1 molar methanolic H_2SO_4. Thereafter, the EBSD is carried out. Fig. 1.6 shows the EBSD micrograph of a region from the AG sample.

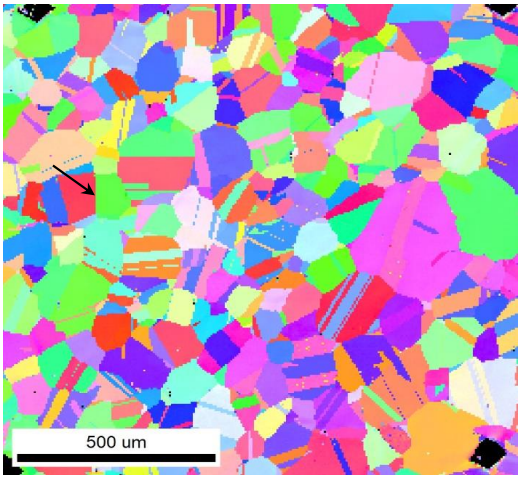

Figure 1.6. EBSD micrograph of the AG sample. The arrow shows a selected GB for bi-crystal milling.

II. Choosing the area of interest

For bi-crystal cantilevers, the selected GB was a high angle grain boundary with the misorientation angle between 45 to 55°. The reason for this selection is discussed in papers I, II and III. The arrow in Fig. 1.6 shows an example of a selected GB.

III. Milling the cantilever

The milling procedure is started by finding the selected area. It should be noted that the GB is completely visible under the SEM and also Ga-beam channel of the focused ion beam (FIB) and therefore the intended cantilever can be milled out with the dimensions depicted in Fig. 1.7. A series of cantilevers are milled on a GB in order to repeat the tests and also doing the experiment in different conditions (H-free and H-charged). Fig. 1.7 also shows an example of cantilever series milled on a selected GB.

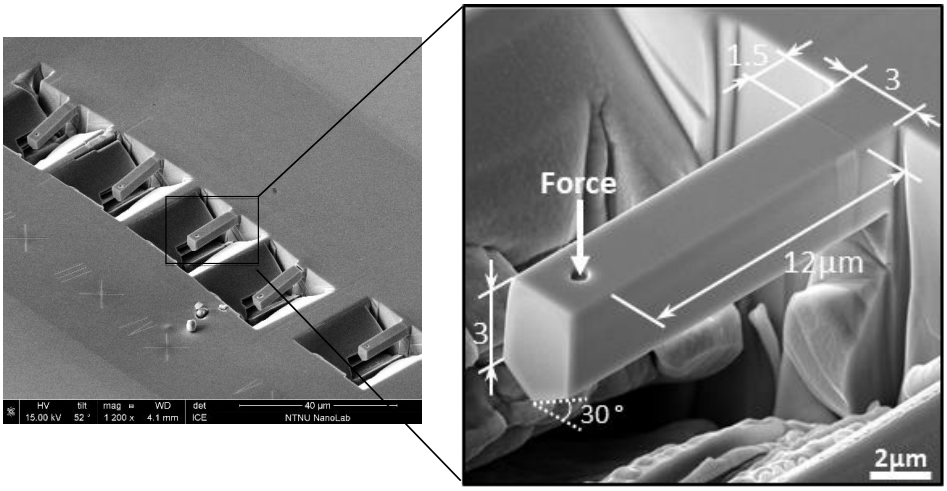

Figure 1.7. A series of cantilevers milled out on a selected GB depicted in Fig. 1.1 (left). The dimensions of a bi-crystal cantilever (right).

An identical shallow notch is milled on all cantilevers above the GB line to increase the probability of cracking. Fig. 1.8 shows a GB on a cantilever before and after notch milling.

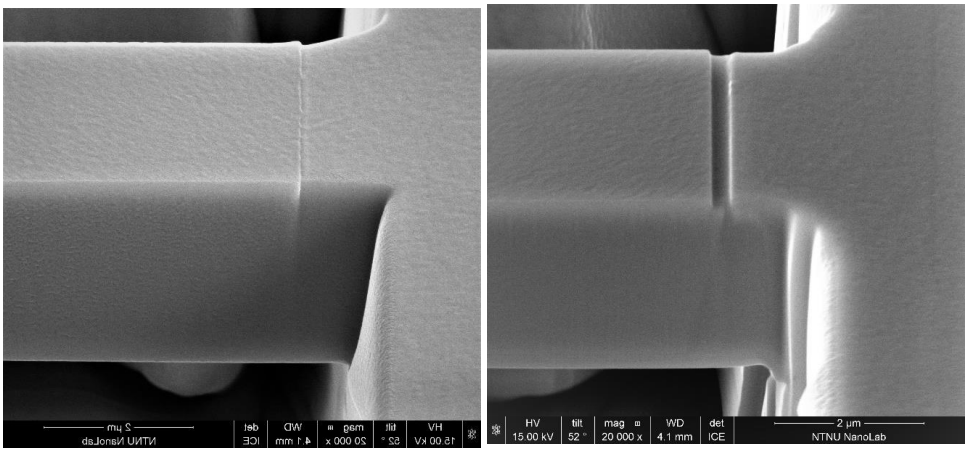

Figure 1.8. A clear GB on a milled bi-crystal cantilever (left). A notch milled on the GB in a bi-crystal cantilever (right).

IV. Setting-up the cell

A miniaturized conventional three electrode cell is used for this study. The cell is installed in the nanoindenter machine chamber which enables in-situ testing (Fig. 19). A schematic diagram of the in-situ cell is depicted in Fig. 1.10. $Hg/HgSO_4$ reference electrode (RE) is used in this study for in-situ testing. This electrode lacks the Cl^- ion which can be found in Calomel or Ag/AgCl electrodes. Cl^- is an anion which associate in corrosion reactions, and this is the reason why it is avoided in this set up. The reference electrode is connected with a tube containing similar solution to the charging electrolyte. The electrolyte was a mixture of Phosphoric acid-Glycerol (1:2 v/v). The counter electrode (CE) was a platinum sheet immersed in the cell solution which is connected with a platinum wire to the electrical connector of the potentiostat. The charging and testing were conducted in room temperature. The working electrode (WE) as depicted in Fig. 1.10, is located at the bottom of the cell. The complementary data on charging potentials and loading regime for cantilever bending can be found in the text of the papers I-IV.

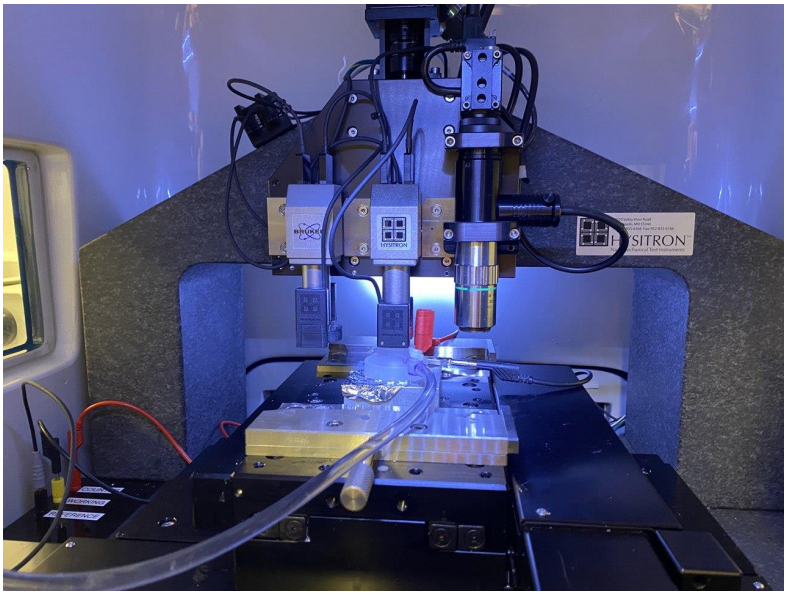

Figure 1.9. In situ test set up in the nanoindenter chamber.

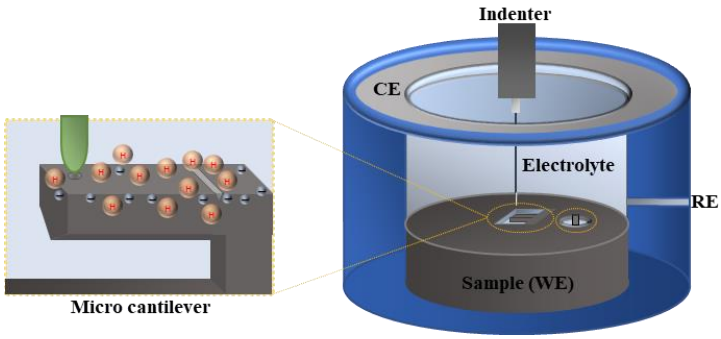

Figure 1.10. A schematic of the in-situ testing cell.

V. Post-deformation analysis

After bending, the sample is taken out, washed with deionized water and ethanol. Afterwards, post-deformation imaging is carried out by SEM. Fig. 1.11 shows an example of one cantilever which is cracked under the H-charging condition.

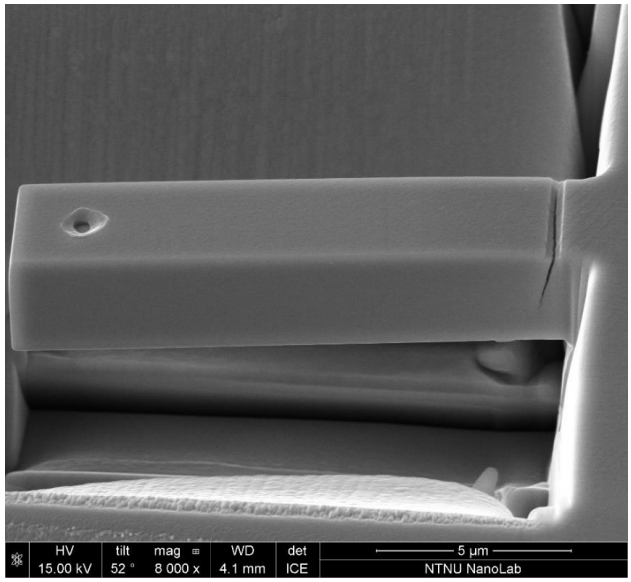

Figure 1.11. Post-deformation SEM image of a cantilever bent in H-charging condition.

FIB is also used in slice and view mode to mill the cantilever from cross sectional view to get images from internal parts of the cantilever. To do so, firstly the cantilever is covered with

the platinum coating (Fig.1.12). The coating protects the surface of the cantilever from damages of Ga-ion required for milling. Afterwards, the adjacent area of the cantilever root will be milled out to make it easy to cut the cantilever while keeping the notch area intact. The cantilever then lifts out and will be placed on a TEM copper finger holder. The cantilever then sliced with the intervals of 100 nm followed by taking an image. The slicing was done from both sides to keep the central part of the cantilever for Transmission EBSD (T-EBSD) analysis. To do T-EBSD one needs to reach a thickness of lesser than 80 nm, since T-EBSD needs electrons to transmit through the material and detected on the other side of the material.

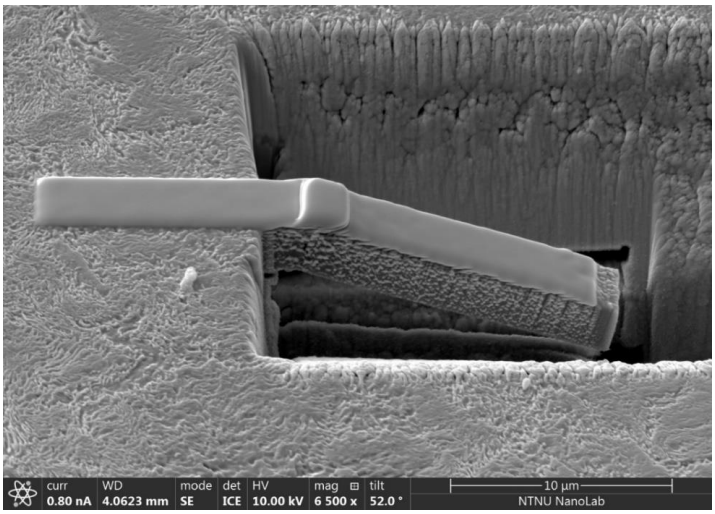

Figure 1.12. Platinum coating of a bent cantilever to protect against further using of Ga-beam of FIB. The material presented here is a high carbon steel.

1.14 X-ray photo-electron spectroscopy

X-ray photoelectron spectroscopy (XPS) is a technique which can analyse very thin oxide layers such as passive layer in stanless steels and nickel superalloys. XPS spectra are obtained by irradiating a material with X-ray beam while simultaneously measuring the kinetic energy and number of electrons escape from the the top surface of the material. The method ables to give information from he elemental composition, empirical formula, chemical state and electronic state of the elements exists in the surface. The tecknique itself is not able to measure the depth distrubution information of the layers but its combination with the ion sputtering can be used to obtain such data. Ion sputtering can remove certain amount of the surface which can be followed by XPS analysis. Therefore, a depth profile if the

elemental data will be provided. Moreover, by this method the thickness of the passive layer can be estimated.

In this study the XPS was used to obtain the passive layer composition formed on the materials and also in order to estimate the thickness of the layer. The passive layer we formed potentiostaticaly in 3.5% NaCl solution. The potentiostatic film formation was carried out at 200 and 600 mV vs. Ag/AgCl reference electrode for one hour. Afterwards, the samples were taken out from the solution, washed with deionized water and ethanol to remove the remained electrolyte on the surface. The samples were then transferred immediately to the XPS analysis chamber inside a desicator. The analysis was carried out with Kratos Axis Ultra DLD. A monochromatic Al Kα source was used as a source. First, a survey of elemental map was done with the pass energy of 160 eV with five sweeps. High resolution regional acquisitions were performed with pass energy of 20 eV with ten sweeps and 0.1 eV step size for each element. Argon sputtering with the energy of 4 V was used for depth profiling. The analysis was started with the elemental map, then the high resolution regional spectroscopy was carried out followed by 30 s argon sputtering. After sputtering another regional spectroscopy was done and this loop is repeated for three times enabling 4 regional spectroscopy at different depths of the surface. The analysis area was 300 × 700 μm^2. The obtained data were analysed using Casa XPS software.

1.15 Intergranular corrosion testing

Double loop electrochemical potentiokinetic reactivation (DL-EPR) test was used to investigate the intergranular corrosion susceptibility of the materials. The samples were mounted in an epoxy resin polymer letting a circular surface of 10 mm diameter to be exposed to the electrolyte. The electrical connection was made from the side of the samples which was embedded in epoxy with a copper wire. The DL-EPR test was carried out in a deareated aqueous solution of 2 M HCL + 1 M H_2SO_4 + 10−4 M KSCN at 30 °C which is developed by Hazarabedian et al. for Alloy 725 [46]. The anodic scan is started from the Open Circuit Potential (OCP) going forward with the scan rate of 1.667 mV/s reversing at 700 mV higher than the OCP. After the test, the samples were rinsed with deionized water and ethanol and placed in SEM chamber in order to take pictures of the corrosion attacks.

1.16 Thermal desorption spectroscopy

Thermal desorption spectroscopy (TDS) is a technique to study the hydrogen trapping characteristics of the metals. In this method the sample is charged with H and then placed in

the TDS chamber. There are two methods of doing TDS. Fistly, the sample can be heated up immediately to a high temperature to allow all of the absorbrd H to be released. In this way the total amount of the H can be measured. In another way, after putting the sample in the TDS chamber, the temperature is gradually increased. This is called a ramping test. By doing ramping test it would be possible to analyze the trapping sites of the material. By doing the ramping test, first the diffusible H and the H which is trapped in tetrahedral and octahedral sites of the material will diffuse out. By raising the temparature, hydrogen in deeper traps will activate and the H which are trapped in high angle grain boundarys (HAGBs) or deep trap interfaces will be released. The extracted H from the material carries with a carrier gas such as Argon or Nitrogen to the mass analyzer to measure the amount of H extracted within the time domain. The obtained results can be shown as the H content versus temperature.

In our study, since Ni is the FCC material with very low diffusivity, thin samples (0.5 mm) were prepared for H charging in order to increase the ration of surface to volum. Therefore, samples with dimensions of $10 \times 5 \times 0.5$ mm were used for H charging. The charging electrolyte was a mixture of phosphoric acid and glycerol (1:2 v/v). The samples were potentiostatically charged at −1050 mV vs. Ag/AgCl reference electrode at a temperature of 75 °C for 24 h. This high temperature is used in order to increase the diffusibility of hydrogen. A G4 Phoenix DH system (Bruker Co.) coupled with a mass spectrometer was used for TDS. The total H content was analyzed by instantaneously exposing the sample to 800 °C for 600 s. In addition, the ramping test was conducted by gradually increasing the temperature from 30 to 800 °C at a heating rate of 0.5 K/s.

1.17 List of publications and contributions

Paper I:

Role of Grain Boundaries in Hydrogen Embrittlement of Alloy 725: Single and Bi-Crystal Microcantilever Bending Study

Authors: Iman Taji, Tarlan Hajilou, Shabnam Karimi, Florian Schott, Ernst Plesiutschnig, Afrooz Barnoush, Roy Johnsen

International Journal of Hydrogen Energy 47.25 (2022): 12771-12781.

https://doi.org/10.1016/j.ijhydene.2022.01.251.

INTERNATIONAL JOURNAL OF HYDROGEN ENERGY 47 (2022) 12771–12781

Available online at www.sciencedirect.com

ScienceDirect

journal homepage: www.elsevier.com/locate/he

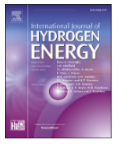

Role of grain boundaries in hydrogen embrittlement of alloy 725: single and bi-crystal microcantilever bending study

Iman Taji [a,*], *Tarlan Hajilou* [a], *Shabnam Karimi* [a], *Florian Schott* [a], *Ernst Plesiutschnig* [b], *Afrooz Barnoush* [a,c], *Roy Johnsen* [a]

[a] *Department of Mechanical and Industrial Engineering, Norwegian University of Science and Technology, No. 7491, Trondheim, Norway*
[b] *Voestalpine BÖHLER Edelstahl GmbH & Co KG, Mariazellerstraße 25, 8605, Kapfenberg, Austria*
[c] *Qatar Environment and Energy Research Institute, P.O. Box 34110, Doha, Qatar*

HIGHLIGHTS

- Single crystal (SC) and bi crystal (BC) in situ cantilever bending test is used.
- SC of over-aged sample experienced severe cracking than the aged sample.
- Load drop for SC over aged cantilevers occurs at lower distance than aged sample.
- Bi crystal cantilever of over-aged was more resistant than aged sample.
- Grain boundary in solution annealed cantilever mitigated the risk of embrittlement.

ARTICLE INFO

Article history:
Received 29 November 2021
Received in revised form
29 January 2022
Accepted 31 January 2022
Available online 21 February 2022

Keywords:
Microcantilever bending
Alloy 725
Heat treatment
Hydrogen embrittlement
Grain boundary

ABSTRACT

In situ electrochemical microcantilever bending tests were conducted in this study to investigate the role of grain boundaries (GBs) in hydrogen embrittlement (HE) of Alloy 725. Specimens were prepared under three different heat treatment conditions and denoted as solution-annealed (SA), aged (AG) and over-aged (OA) samples. For single-crystal beams in an H-containing environment, all three heat-treated samples exhibited crack formation and propagation; however, crack propagation was more severe in the OA sample. The anodic extraction of H presented similar results as those under the H-free condition, indicating the reversibility of the H effect under the tested conditions. Bi-crystal micro-cantilevers bent under H-free and H-charged conditions revealed the significant role of the GB in the HE of the beams. The results indicated that the GB in the SA sample facilitated dislocation dissipation, whereas for the OA sample, it caused the retardation of crack propagation. For the AG sample, testing in an H-containing environment led to the formation of a sharp, severe crack along the GB path.

Contribution:

Iman Taji: Planning and execution of all experimental parts, data analysis and paper writing.

Tarlan Hajilou: Discussion and advice, review and editing the paper, supervision.

Shabnam Karimi: Helping in TDS measurement.

Florian Schott: Helping in cantilever milling.

Ernst Plesiutschnig: Materials provider, TEM analysis.

Afrooz Barnoush: Research design, discussion and advice, supervision.

Roy Johnsen: review and editing the paper, supervision.

Paper II:

Hydrogen Assisted Intergranular Cracking of Alloy 725: The Effect of Boron and Copper Alloying

Authors: Iman Taji, Tarlan Hajilou, Anna Sophie Ebner, Daniel Scheiber, Shabnam Karimi, Ernst Plesiutschnig, Werner Ecker, Afrooz Barnoush, Verena Maier-Kiener, Roy Johnsen, Vsevolod I. Razumovskiy.

Corrosion Science, Available online 25 April 2022, 110331.

https://doi.org/10.1016/j.corsci.2022.110331.

Corrosion Science 203 (2022) 110331

Contents lists available at ScienceDirect

Corrosion Science

journal homepage: www.elsevier.com/locate/corsci

Hydrogen assisted intergranular cracking of alloy 725: The effect of boron and copper alloying

Iman Taji [a,*], Tarlan Hajilou [a], Anna Sophie Ebner [b], Daniel Scheiber [c], Shabnam Karimi [a], Ernst Plesiutschnig [d], Werner Ecker [c], Afrooz Barnoush [a,e], Verena Maier-Kiener [b], Roy Johnsen [a], Vsevolod I. Razumovskiy [c]

[a] Department of Mechanical and Industrial Engineering, Norwegian University of Science and Technology, No. 7491, Trondheim, Norway
[b] Department Materials Science, Montanuniversität Leoben, Jahnstraße 12, 8700 Leoben, Austria
[c] Materials Center Leoben Forschung GmbH, Roseggerstraße 12, 8700 Leoben, Austria
[d] Voestalpine Böhler Edelstahl GmbH & Co KG, [Mariazellerstraße 25, 8605 Kapfenberg, Austria
[e] Qatar Environment and Energy Research Institute (QEERI), Hamad Bin Khalifa University (HBKU), P.O. Box 34110, Doha, Qatar

ARTICLE INFO

Keywords:
Hydrogen embrittlement
Nickel-based superalloy
Density functional theory
Micro-scale testing
Atom probe tomography

ABSTRACT

To overcome the Hydrogen embrittlement (HE) susceptibility of the standard Alloy 725 (Mod A), two alloys with minor alloying modifications with B (Mod B) and B+Cu (Mod C) were produced. Then, the intergranular cracking susceptibility was investigated on bi-crystal beams by electrochemical in situ micro-cantilever bending test. The atom probe tomography and first principles calculations were employed to capture and calculate the grain boundary (GB) segregation and its effect on the GB cohesion. Cross-sectional view of the bent beams showed the superior resistance of Mod B against HE by facilitating the GB dislocation transfer/generation. While bending Mod A sample in hydrogen environment leads to form a sharp intergranular cracking, Mod B showed some nano-voids/cracks mostly in dislocation slip bands and rarely in GB path. However, a reduction of strength was observed in load-displacement (L-D) curves of Mod B. The addition of Cu, although not participated in GB segregation, compromised the lost strength of Mod B. In Mod C, after bending in H-charged condition, the nano-voids were formed in GB, but no load drop in L-D curves nor crack propagation in post-deformation observations was detected. The micro-alloying proposed in this study could be an important contribution to the future developing of H resistant alloys via GB segregation engineering.

Contribution:

Iman Taji: Planning and execution of experimental parts, data analysis and paper writing.

Tarlan Hajilou: Discussion and advice, helping in cantilever milling, review and editing the paper, supervision.

Anna Sophie Ebner: Performing the APT test and writing the related part.

Daniel Scheiber: DFT calculations and writing the related part.

Shabnam Karimi: Helping in TDS measurement.

Ernst Plesiutschnig: Materials provider.

Werner Ecker: Supervisor of Anna.

Afrooz Barnoush: Research design, discussion and advice, supervision.

Roy Johnsen: Supervision, review and editing the paper.

Vsevolod I. Razumovskiy: Supervision of DFT part, review and editing the paper, project leader.

Paper III:

Hydrogen-enhanced intergranular failure of sulfur-doped nickel grain boundary: In situ electrochemical micro-cantilever bending vs. DFT

Authors: Tarlan Hajilou, Iman Taji, Frederic Christien, Shuang He, Daniel Scheiber, Werner Ecker, Reinhard Pippan, Vsevolod I. Razumovskiy, Afrooz Barnoush.

Materials Science and Engineering: A 794 (2020): 139967.

https://doi.org/10.1016/j.msea.2020.139967.

Materials Science & Engineering A 794 (2020) 139967

Contents lists available at ScienceDirect

Materials Science & Engineering A

journal homepage: www.elsevier.com/locate/msea

Hydrogen-enhanced intergranular failure of sulfur-doped nickel grain boundary: In situ electrochemical micro-cantilever bending vs. DFT

Tarlan Hajilou [a,*], Iman Taji [a], Frederic Christien [b], Shuang He [c,d], Daniel Scheiber [c], Werner Ecker [c], Reinhard Pippan [e], Vsevolod I. Razumovskiy [c], Afrooz Barnoush [a]

[a] Department of Mechanical and Industrial Engineering, Norwegian University of Science and Technology, No. 7491 Trondheim, Norway
[b] Mines Saint-Etienne, Univ Lyon, CNRS, UMR 5307 LGF, Centre SMS, F-42023 Saint-Etienne, France
[c] Materials Center Leoben Forschung GmbH, Roseggerstraße 12, 8700 Leoben, Austria
[d] Department Materials Science, Montanuniversität Leoben, Jahnstraße 12, 8700 Leoben, Austria
[e] Erich Schmid Institute of Materials Science, Austrian Academy of Sciences, Jahnstraße 12, 8700 Leoben, Austria

ARTICLE INFO

Keywords:
Hydrogen embrittlement
Nickel
Sulfur segregation
Intergranular cracking
Density functional theory
Micro-cantilever

ABSTRACT

Intergranular failure of nickel (Ni) single grain boundaries (GBs) owing to the segregation of sulfur (S), hydrogen (H), and their co-segregation has been investigated by employing micro-cantilever bending tests and density functional theory (DFT) calculations. A pure Ni GB shows completely plastic behavior with no fracture observed in the experiments. Electrochemical H-charging of the sample with no S present in the GB leads to a crack formed at the notch tip, which propagates by means of the mixed plastic–brittle fracture mode. Cantilever testing of the H-charged GB with S results in a clear brittle fracture of the GB. The co-segregation of S and H shifts the sudden drop in the load–displacement curves to smaller values of displacement. This is explained by the combined effect of these elements on the work of separation of the selected GB leading to severely decreased GB cohesion.

Contribution:

Tarlan Hajilou: Planning and execution of experimental parts, data analysis and paper writing.

Iman Taji: Planning and execution of experimental parts, data analysis and paper writing.

Frederic Christien: Performing WDS.

Shuang He: DFT calculations and writing the related part.

Daniel Scheiber: DFT calculations and writing the related part.

Werner Ecker: Supervision of DFT part.

Reinhard Pippan: Supervision of DFT part.

Vsevolod I. Razumovskiy: Supervision of DFT part.

Afrooz Barnoush: Research design, discussion and advice, supervision.

Paper IV:

Intergranular Corrosion and Passive Layer Properties of Alloy 725 Modified with Boron and Copper Micro-alloying

Author: Iman Taji, Tarlan Hajilou, Shabnam Karimi, Afrooz Barnoush, Roy Johnsen.

To be submitted.

Intergranular Corrosion and Passive Layer Properties of Alloy 725 Modified with Boron and Copper Micro-alloying

Iman Taji[a,*], Tarlan Hajilou[a], Shabnam Karimi[a], Afrooz Barnoush[a,b], Roy Johnsen[a]

[a]*Department of Mechanical and Industrial Engineering, Norwegian University of Science and Technology, No. 7491 Trondheim, Norway*
[b]*Qatar Environment and Energy Research Institute, P.O. Box 34110, Doha, Qatar*

Abstract

In this study the effect of B and Cu alloying on corrosion properties of Alloy 725 is investigated. Mod A sample was prepared as a control sample with conventional standard heat treatment. Then two other samples were prepared by adding 250 to 350 wt.ppm B, named Mod B and Mod C with B content lower than 100 ppm plus 2.3 wt.% Cu. The samples were subjected to intergranular corrosion testing, Mott-Shottky and X-ray photoelectron (XPS) analysis. Intergranular corrosion test showed continious corrosion at the grain boundaries (GB) in Mod A while Mod C remains completely intact without any corroison attack. Mod B corroded in the areas around the Mo-rich boride phases formed due to abundant of B element in this alloy. Mod C showed the least defect density in the passive layer while the passive layer of Mod B thicker. The incorporation of Mo in Mod C was proposed to be the the responsible for less defect density of Mod C compared to Mod B. Mod A on the other hand had the most defect density and shows higher passive current density in potentiodynamic polarization test.

Keywords: Intergranular Corrosion, Mott-Schottky analysis, XPS, Alloy 725

Contributions:

Iman Taji: Planning and execution of all experimental parts, data analysis and paper writing.

Tarlan Hajilou: Discussion and advice, review and editing the paper, supervision.

Shabnam Karimi: Helping in cantilever milling.

Afrooz Barnoush: Research design, discussion and advice.

Roy Johnsen: Supervision, review and editing the paper.

1.18 Summary of the papers

Paper I

Role of Grain Boundaries in Hydrogen Embrittlement of Alloy 725: Single and Bi-Crystal Microcantilever Bending Study

In this study, Alloy 725 with three different heat treatment were used. One sample is solution annealed at 1038 °C for 2 h (SA). The aged (AG) sample was prepared by annealing the prior solution at 1038 °C for 2 h, followed by water quenching and heating up to 732 °C for 8 h, cooling in a furnace down to 621 °C, and maintenance at this temperature for 8 h. In order to have coarser precipitates, the over-aged sample (OA) was prepared by increasing the aging temperature from 732 °C to 780 °C. TEM study shoewd that the SA sample had almost no precipitation while in AG sample ellipsoid γ'' precipitates could be observed. For the AG sample, the size of the precipitates increased significantly which is led to presence of less precipitates in this condition.

The microcanliteleves, first milled in the grains to compare the strength of the grain interior of the samples. For HE studies, the samples were electrochemically charged with H in the electrolyte of phosphoric acid and glycerol (1:2 v/v) for two hours at −1500 vs. $Hg/HgSO_4$ (−1050 vs. Ag/AgCl). After this process of charging, the bending test using the nanoindeter was started while keeping the cathodic potential during the test.

The results of H-free experiments showed that the SA sample had the lowest maximum load (around 800 µN) which is related to lack of precipitates. The AG sample had the highest load (around 1400 µN) while the maximum load for OA sample was 200 µN lower. The reason of deacreasing the load in OA sample can be related to the less frequent and coarser precipitates compared to AG one. However, under the H-charged condition, the OA sample experienced more severe cracking. The load in load-displacement (L-D) curve of OA sample fell down after about 1500 nm displacement, while it dropped at about 3200 nm for AG sample.

In order to examine the role of GBs on the HE, HAGBs were selected from the samples helping EBSD analysis and the cantilevers were milled in a way to have this selected GBs on the cantilever. In this manner, with comparing the single crystal bending data, the role of the GB can be revealed. The results showed that the GBs can have different impacts on the results. The comparison of the single and bi-crystal bent cantilevers of the SA sample under the H-free condition revealed a softening effect in the bi-crystal cantilevers. In H condition because of this softeing effwet, no crack was revealed in SA bi-crystal cantilever.

Contrary to the single crystal results, in bi-crystal cantilevers the maximum load was higher for OA sample. Post-deformation SEM images showed that this behaviour is related to the serrated GB formed in the OA sample due to the presence of coarse GB precipitates. The serreated GB in OA sample prevents the H-induced crack to propagate while a sharp continuous crack was formed in the AG bi-crystal cantilever.

Paper II

Hydrogen Assisted Intergranular Cracking of Alloy 725: The Effect of Boron and Copper Alloying

In this study, the standard Alloy 725 (Mod A) is modified with 250 to 350 ppm B (Mod B) and 2.3 wt.% Cu + <100 ppm B (Mod C). Bi-crystal microcantilevers were prepared on the HAGBs of these samples to investigate the role of alloying elements on HE. The microcantilevers were bent in-situ under the H charging condition. The electrolyte was a mixture of phosphoric acid and glycerol (1:2 v/v) and the charging time before starting the test was two hours at −1500 vs. $Hg/HgSO_4$ (−1050 vs. Ag/AgCl).

The density functional theory (DFT) caclulations showed that the B tends to precipitate in GBs while Cu is more likely to be in solid-solution form. Atom prob tomography (APT) also confirmed the precipitation of B at the GBs.

In H-free condition work-hardening was taken place for Mod A. A high amount of dislocation pile up is found behind the GB. The high accumulated stress leads to distortion and deviation of the GB from its original path. In this sample during H-charging, a sharp intergranular crack was observed.

Addition of B improved the HE-resistance of Mod B, however, at the cost of reducing the strength of the alloy. B contributed to the ductility enhancement of the alloy by releasing the accumulated stress behind the GB via enhancing the GB dislocation transmission/generation. B also increased the boundary cohesive energy based on DFT results. Therefore in air condition no void/crack is formed. In H environment, nano-voids were observed in either dislocation slip banbs (DSBs) or GBs. However, the formed nano-voids did not show any effect on the strength and the integrity of the bent beams.

In Mod C, the loss of strength happened in L-D curve of Mod B is compensated by solid solution hardening by Cu. DFT and APT results showed that Cu tends to deplete at the GBs. Therefore the amount of Cu at the GBs are less than the bulk content. However its presence at

the GB reduces the strengthening energy of the GB. As a result, larger nano-voids compared to Mod B were formed at the GB after in situ bending. Albeit, even with the addition of H, no propagating crack is formed in the GB nor in the matrix.

Paper III:

Hydrogen-enhanced intergranular failure of sulfur-doped nickel grain boundary: In situ electrochemical micro-cantilever bending vs. DFT

Two type of samples in were used in this study, a pure Ni and a Ni sample which is dopedwith GB segregated S. The purpose of this study was to investigate the effedt of co-segregations of S and H on intergranular cracking. The S-doped sample contains 5.4 wt ppm of S in solid solution condition measured by a glow discharge mass spectroscopy technique. Following casting, hot rolling and cold rolling processes were carried out to decrease the thickness of the ingot to 3 mm. Afterwards, the material was annealed 72 h at 1300 ∘C and 24 h at 1000 ∘C followed by water cooling in order to GB segregation. The GB segregation was confirmed by Wavelength dispersive X-ray spectroscopy.

The micro-beams in this study were charged with a cathodic current density in the range of -60 to $-100\ \mu A\ cm^{-2}$ at -1450 to -1600 mV potential versus the $Hg/HgSO_4$ reference electrode. A glycerol-based solution with the composition of 1.3 M borax in glycerol mixed with 20% distilled water was used as the H-charging electrolyte.

Cantilever bending tests with pure Ni samples without S segregation resulted in a ductile behavior accompanied by slip traces on the surface, while testing pure Ni in H-charged condition, the crack is initiated from the notch area and fewer activated slip traces are observed. The observed difference is associated with the impeding effect of H on the dislocation motion leading to the and localized plasticity at the crack tip. Post-deformation SEM images showed that the crack formed in the H-charged pure Ni beam is neither intergranular (IG) nor purely brittle. In this case, H concentration at the GB does not reach the critical amount to cause the IG fracture atomic associated with the HEDE mechanism.

Segregation of S to GB, on the pther hand, leads to the IG cracking during the bending test. The crack reveals brittle type of fracture and propagates through the GB. Hydrogen-charging makes the IG fracture even more prominent and causes a sooner sudden drop in L–D curves compared with H-free conditions. Based on the DFT results, it is shown that the GB cohesion is much more reduced by S enrichment in comparison with H enrichment. Even though the

co-segregation of S and H substantially reduces the cohesion of the selected GB, no interaction between S and H effects is obtained by DFT calculations.

Paper IV

Intergranular Corrosion and Passive Layer Properties of Alloy 725 Modified with Boron and Copper Micro-alloying

In this study, intergranular corrosion and passive layer properties of Mod A (standard Alloy 725), B (modified with 250 to 350 ppm B) and C (modified with 2.3 wt.% Cu + <100 ppm B) alloys were investigated. DL-EPR test was carried out in the deareated aqueous solution of 2 M HCL + 1 M H_2SO_4 + 10^{-4} M KSCN at 30 °C which is developed by Hazarabedian et al. [46] for Alloy 725. The anodic scan started at the OCP goingforward with the scan rate of 1.667 mV/s reversing at 700 mV higher than the OCP.

Based on the DL-EPR results, no intergranular corrosion occured for Mod C which is conformed by SEM images taken after the test. However, in both Mod A and B a reactivation peak was appeared in the curves. The flollwing SEM images from the surface, showed that the type of corrosion on Mod A and B is different.

In Mod A, the corrosion is completely intergranular. A continious trench can be found in GBs in SEM images. The intergranular corrosion occurred in Mod A could be a results of the Cr/Mo-rich phases presence at the GBs. These phases absorb a lot of Cr/Mo and there would be in impoverishment of these alloys around the GB. Therefore, the weak passive layer formed around the GB will dissolve during the reverse scan of the DL-EPR resulting in the reactivation peald to be appeared.

In Mod B, on the other hand, the corrosion occurred around the Mo-rich phases which can be found in both GBs and grain interior. These phases are Mo and Ti-rich borides which formed in this sample due to the presense of high amount of B. The phases absorbs lots of Mo and the passive laer around these particles will not be strong enough to withstand in the reverse scan. Therfore the reactivation peak observed in this sample is related to the corroison happening around these phases.

Mott-Schottky analysis was carryied out to compare the differences between vacancy densities and the nature of the passive film. The results revealed that Mod C has the least vacancy while Mod A possessed the highest amount of vacancies in its structure. The graph of all materials consisted of two parts. The first part from -100 mV to around 400 mV vs.

Ag/AgCl shows a n-type passive layer whereas from 400 to 800 mV vs. Ag/AgCl the passive layers showed p-typer behaviour.

Finally, the passive layers were analyzed with XPS. It is revealed that the thickness of Mod B is a bit higher than Mod A and C. In addition the passive layer for,ed at 600 mV vs. Ag/AgCl is thicked that the layer formed at 200 mV vs. Ag/AgCl. In 600 mV vs. Ag/AgCl the oxygen content is highter and this could be the reason for more oxide formation and henece the thicker passive layer. In addition the availability of more oxygen in high voltages might be the reason for shiftong from n-type to p-typ passive layer.

2 Recommendations and Future works

Throughout this thesis, the interactions of H with pure nickel and nickel superalloys with different heat treatments and GB segregation have been studied. The following suggestions can be put forth for future studies.

2.1 The effect of GB type

In papers I, II and III, all the micro-cantilevers were made on the high angle grain boundaries (HAGBs). It is well-known that these GBs are the most probable sites for cracking. They are also favorable site for impurities to precipitate. However, there are reports which shows that low angle (LA)GBs or special GBs such as Σ3 GBs can be probable areas for crack nucleation. For example, Seita et al. [47] by doing tensile tests on Alloy 725 have shown that Σ3 coherent twin boundaries are susceptible to crack initiation but they are resistant against crack propagation. This dual role of the Σ3 GBs leads them to offer a new design for Nickel superalloys. Since the H-induced cracks often initiate at surfaces and propagate inward, the proposed to make a microstructurally graded material with few Σ3 GBs at the surface and a large number in the interior parts. However, this observation needs more proof. In-situ micro-cantilever testing on Σ3 GBs, can shed more light in this regard. The problem is getting more complicated knowing that the HAGBs are more prone to corrosion. Our preliminary EBSD analysis which is not reported in this thesis showed that the intergranular corrosion is happening mostly at the HAGBs. Therefore, designing a material with high amount of HAGBs at surface can be risky from corrosion point of view. As another suggestion, investigating the relation of GB type and intergranular corrosion can be interesting.

2.2 Formation of Ni-hydride

In paper III, we showed that the presence of abundant H resulted in the hardness increase on the surface which is persistent for long time. We attributed this phenomenon to the formation of Ni-H, although it is reported that the Ni-H is not a stable phase. Direct observation of this Ni-H can be advantageous. This can be happened on the Ni-superalloys as well and significantly change the mechanical properties. The presence of this alloy in highly sour environments might provide harsh conditions suitable for Ni-H formation. From experimental point of view in-situ XRD or in-situ Raman spectroscopy can help to detect the hydride formation on the alloy.

2.3 In-situ stress corrosion cracking by micro-cantilever bending

As observed in paper V, intergranular corrosion led to form grooves on the materials surface. These grooves, in the presence of external load can act as an initiation site for cracks. Therefore, by having the corrosive media and applying the load which is feasible by in-situ cantilever bending one can evaluate the stress corrosion cracking (SCC) resistance of specific GBs. In this system, the notch is not required and the groove which will be formed by the corrosion processes will act as the accelerator for cracking. The test can be carried out in anodic voltages in order to avoid the role of H in SCC.

References

[1] M. Iannuzzi, A. Barnoush, R. Johnsen, Materials and corrosion trends in offshore and subsea oil and gas production, npj Materials Degradation, 1 (2017) 1-11.

[2] M. Iannuzzi, Environmentally assisted cracking (EAC) in oil and gas production, in: Stress corrosion cracking, Elsevier, 2011, pp. 570-607.

[3] M.S. Hazarabedian, M. Iannuzzi, The role of nano-sized intergranular phases on nickel alloy 725 brittle failure, npj Materials Degradation, 5 (2021) 1-9.

[4] P. Nice, R. Strong, W.M. Bailey, G. Rørvik, J.H. Olsen, T.G. Mobberley, Hydrogen embrittlement failure of a precipitation hardened nickel alloy subsurface safety valve component installed in a North Sea seawater injection well, in: CORROSION 2014, OnePetro, 2014.

[5] H. Sarmiento Klapper, J. Klöwer, O. Gosheva, Hydrogen embrittlement: the game changing factor in the applicability of nickel alloys in oilfield technology, Philosophical Transactions of the Royal Society A: Mathematical, Physical and Engineering Sciences, 375 (2017) 20160415.

[6] L. Liu, J. Zhang, C. Ai, Nickel-Based Superalloys, in: F.G. Caballero (Ed.) Encyclopedia of Materials: Metals and Alloys, Elsevier, Oxford, 2022, pp. 294-304.

[7] B. Geddes, H. Leon, X. Huang, Superalloys: alloying and performance, Asm International, 2010.

[8] D. Raabe, M. Herbig, S. Sandlöbes, Y. Li, D. Tytko, M. Kuzmina, D. Ponge, P.-P. Choi, Grain boundary segregation engineering in metallic alloys: A pathway to the design of interfaces, Current Opinion in Solid State and Materials Science, 18 (2014) 253-261.

[9] S. Chen, A. Voter, R. Albers, A. Boring, P. Hay, Investigation of the effects of boron on Ni3Al grain boundaries by atomistic simulations, Journal of Materials Research, 5 (1990) 955-970.

[10] P. Kontis, E. Alabort, D. Barba, D.M. Collins, A.J. Wilkinson, R.C. Reed, On the role of boron on improving ductility in a new polycrystalline superalloy, Acta Materialia, 124 (2017) 489-500.

[11] G. Da Rosa, P. Maugis, A. Portavoce, J. Drillet, N. Valle, E. Lentzen, K. Hoummada, Grain-boundary segregation of boron in high-strength steel studied by nano-SIMS and atom probe tomography, Acta Materialia, 182 (2020) 226-234.

[12] S. Tamirisakandala, R.B. Bhat, J.S. Tiley, D.B. Miracle, Processing, microstructure, and properties of β titanium alloys modified with boron, Journal of Materials Engineering and Performance, 14 (2005) 741-746.
[13] H.A.U. Heubner, Aqueous Corrosion of Nickel and its Alloys, in: Shreir's Corrosion, Elsevier, 2010.
[14] Nickel and Nickel alloys, in: D.C.A.N. Sridhar (Ed.) Uhlig's Corrosion Handbook, John Wiley & Sons, Inc., 2011.
[15] M. Koyama, M. Rohwerder, C.C. Tasan, A. Bashir, E. Akiyama, K. Takai, D. Raabe, K. Tsuzaki, Recent progress in microstructural hydrogen mapping in steels: quantification, kinetic analysis, and multi-scale characterisation, Materials Science and Technology, 33 (2017) 1481-1496.
[16] S.P. Lynch, 2 - Hydrogen embrittlement (HE) phenomena and mechanisms, in: V.S. Raja, T. Shoji (Eds.) Stress Corrosion Cracking, Woodhead Publishing, 2011, pp. 90-130.
[17] A. Oudriss, J. Creus, J. Bouhattate, E. Conforto, C. Berziou, C. Savall, X. Feaugas, Grain size and grain-boundary effects on diffusion and trapping of hydrogen in pure nickel, Acta Materialia, 60 (2012) 6814-6828.
[18] E. Wollan, J. Cable, W. Koehler, The hydrogen atom positions in face centered cubic nickel hydride, Journal of Physics and Chemistry of Solids, 24 (1963) 1141-1143.
[19] A. Kimura, H. Birnbaum, The effects of cathodically charged hydrogen on the flow stress of nickel and nickel-carbon alloys, Acta Metallurgica, 35 (1987) 1077-1088.
[20] M.B. Djukic, G.M. Bakic, V.S. Zeravcic, A. Sedmak, B. Rajicic, The synergistic action and interplay of hydrogen embrittlement mechanisms in steels and iron: Localized plasticity and decohesion, Engineering Fracture Mechanics, 216 (2019) 106528.
[21] M. Yamaguchi, M. Shiga, H. Kaburaki, Energetics of segregation and embrittling potency for non-transition elements in the Ni Σ5 (012) symmetrical tilt grain boundary: a first-principles study, Journal of Physics: Condensed Matter, 16 (2004) 3933.
[22] H.K. Birnbaum, P. Sofronis, Hydrogen-enhanced localized plasticity—a mechanism for hydrogen-related fracture, Materials Science and Engineering: A, 176 (1994) 191-202.
[23] I.M. Robertson, P. Sofronis, A. Nagao, M. Martin, S. Wang, D. Gross, K. Nygren, Hydrogen embrittlement understood, Metallurgical and Materials Transactions A, 46 (2015) 2323-2341.
[24] Y. Zhao, M.-Y. Seok, I.-C. Choi, Y.-H. Lee, S.-J. Park, U. Ramamurty, J.-Y. Suh, J.-i. Jang, The role of hydrogen in hardening/softening steel: Influence of the charging process, Scripta Materialia, 107 (2015) 46-49.

[25] T. Hajilou, Y. Deng, B.R. Rogne, N. Kheradmand, A. Barnoush, In situ electrochemical microcantilever bending test: A new insight into hydrogen enhanced cracking, Scripta Materialia, 132 (2017) 17-21.
[26] D. Wan, Y. Deng, J.I.H. Meling, A. Alvaro, A. Barnoush, Hydrogen-enhanced fatigue crack growth in a single-edge notched tensile specimen under in-situ hydrogen charging inside an environmental scanning electron microscope, Acta Materialia, 170 (2019) 87-99.
[27] R. Kirchheim, Revisiting hydrogen embrittlement models and hydrogen-induced homogeneous nucleation of dislocations, Scripta materialia, 62 (2010) 67-70.
[28] W.H. Johnson, II. On some remarkable changes produced in iron and steel by the action of hydrogen and acids, Proceedings of the Royal Society of London, 23 (1875) 168-179.
[29] R.P. Gangloff, B.P. Somerday, Gaseous hydrogen embrittlement of materials in energy technologies: mechanisms, modelling and future developments, Elsevier, 2012.
[30] S. Bechtle, M. Kumar, B.P. Somerday, M.E. Launey, R.O. Ritchie, Grain-boundary engineering markedly reduces susceptibility to intergranular hydrogen embrittlement in metallic materials, Acta materialia, 57 (2009) 4148-4157.
[31] F. Yang, J.C.-M. Li, Micro and nano mechanical testing of materials and devices, Springer, 2008.
[32] J. Ast, M. Ghidelli, K. Durst, M. Göken, M. Sebastiani, A.M. Korsunsky, A review of experimental approaches to fracture toughness evaluation at the micro-scale, Materials & Design, 173 (2019) 107762.
[33] D. Di Maio, S. Roberts, Measuring fracture toughness of coatings using focused-ion-beam-machined microbeams, Journal of materials research, 20 (2005) 299-302.
[34] T. Halford, K. Takashima, Y. Higo, P. Bowen, Fracture tests of microsized TiAl specimens, Fatigue & Fracture of Engineering Materials & Structures, 28 (2005) 695-701.
[35] G. Dehm, B.N. Jaya, R. Raghavan, C. Kirchlechner, Overview on micro-and nanomechanical testing: New insights in interface plasticity and fracture at small length scales, Acta Materialia, 142 (2018) 248-282.
[36] R. Pippan, S. Wurster, D. Kiener, Fracture mechanics of micro samples: Fundamental considerations, Materials & Design, 159 (2018) 252-267.
[37] A. Barnoush, H. Vehoff, In situ electrochemical nanoindentation: A technique for local examination of hydrogen embrittlement, Corrosion Science, 50 (2008) 259-267.
[38] ISO 15156-1, in: Petroleum, petrochemical, and natural gas industries — Materials for use in H2S-containing environments in oil and gas production — Part 1: General principles for selection of cracking-resistant materials, 2015.

[39] Z. Khan, S. Fida, F. Nisar, N. Alam, Investigation of Intergranular Corrosion in 2nd stage gas turbine blades of an aircraft engine, Engineering Failure Analysis, 68 (2016) 197-209.
[40] H.T. Lee, J.L. Wu, Intergranular corrosion resistance of nickel-based alloy 690 weldments, Corrosion science, 52 (2010) 1545-1550.
[41] J. Zhang, L. Xu, Y. Han, L. Zhao, B. Xiao, New perspectives on the grain boundary misorientation angle dependent intergranular corrosion of polycrystalline nickel-based 625 alloy, Corrosion Science, 172 (2020) 108718.
[42] A. G28–02, Standard Test Methods for Detecting Susceptibility to Intergranular Corrosion in Wrought, Nickel-Rich, Chromium-Bearing Alloys, in, 2015.
[43] A.P. Majidi, M.A. Streicher, The double loop reactivation method for detecting sensitization in AISI 304 stainless steels, Corrosion, 40 (1984) 584-593.
[44] A.S.f. Testing, Materials, Standard Test Method for Electrochemical Reactivation (EPR) for Detecting Sensitization of AISI Type 304 and 304L Stainless Steels, in: ASTM-G108, ASTM International, 2015.
[45] I. Taji, M.H. Moayed, M. Mirjalili, Correlation between sensitisation and pitting corrosion of AISI 403 martensitic stainless steel, Corrosion Science, 92 (2015) 301-308.
[46] M.S. Hazarabedian, M. Lison-Pick, M.Z. Quadir, M. Iannuzzi, Detecting Intergranular Phases in UNS N07725: Part I. Adapting the Double-Loop Electrochemical Potentiokinetic Reactivation Test, Journal of The Electrochemical Society, 168 (2021) 031506.
[47] M. Seita, J.P. Hanson, S. Gradečak, M.J. Demkowicz, The dual role of coherent twin boundaries in hydrogen embrittlement, Nature communications, 6 (2015) 1-6.
[48] I. Taji, T. Hajilou, A.S. Ebner, D. Scheiber, S. Karimi, E. Plesiutschnig, W. Ecker, A. Barnoush, V. Maier-Kiener, R. Johnsen, Hydrogen Assisted Intergranular Cracking of Alloy 725: The Effect of Boron and Copper Alloying, Corrosion Science, (2022) 110331.

3 Appended papers

Paper I: Role of Grain Boundaries in Hydrogen Embrittlement of Alloy 725: Single and Bi-Crystal Microcantilever Bending Study

Iman Taji[a,*], Tarlan Hajilou[a], Shabnam Karimi[a], Florian Schott[a], Ernst Plesiutschnig[b], Afrooz Barnoush[a,c], Roy Johnsen[a]

[a]Department of Mechanical and Industrial Engineering, Norwegian University of Science and Technology, No. 7491 Trondheim, Norway

[b]voestalpine BÖHLER Edelstahl GmbH & Co KG, Mariazellerstraße 25, 8605 Kapfenberg, Austria

[c]Qatar Environment and Energy Research Institute, P.O. Box 34110, Doha, Qatar

International Journal of Hydrogen Energy 47.25 (2022): 12771-12781.

https://doi.org/10.1016/j.ijhydene.2022.01.251.

INTERNATIONAL JOURNAL OF HYDROGEN ENERGY 47 (2022) 12771–12781

Available online at www.sciencedirect.com

ScienceDirect

journal homepage: www.elsevier.com/locate/he

Role of grain boundaries in hydrogen embrittlement of alloy 725: single and bi-crystal microcantilever bending study

Iman Taji [a,*], *Tarlan Hajilou* [a], *Shabnam Karimi* [a], *Florian Schott* [a], *Ernst Plesiutschnig* [b], *Afrooz Barnoush* [a,c], *Roy Johnsen* [a]

[a] *Department of Mechanical and Industrial Engineering, Norwegian University of Science and Technology, No. 7491, Trondheim, Norway*

[b] *Voestalpine BÖHLER Edelstahl GmbH & Co KG, Mariazellerstraße 25, 8605, Kapfenberg, Austria*

[c] *Qatar Environment and Energy Research Institute, P.O. Box 34110, Doha, Qatar*

HIGHLIGHTS

- Single crystal (SC) and bi crystal (BC) in situ cantilever bending test is used.
- SC of over-aged sample experienced severe cracking than the aged sample.
- Load drop for SC over aged cantilevers occurs at lower distance than aged sample.
- Bi crystal cantilever of over-aged was more resistant than aged sample.
- Grain boundary in solution annealed cantilever mitigated the risk of embrittlement.

ARTICLE INFO

Article history:
Received 29 November 2021
Received in revised form
29 January 2022
Accepted 31 January 2022
Available online 21 February 2022

Keywords:
Microcantilever bending
Alloy 725
Heat treatment
Hydrogen embrittlement
Grain boundary

ABSTRACT

In situ electrochemical microcantilever bending tests were conducted in this study to investigate the role of grain boundaries (GBs) in hydrogen embrittlement (HE) of Alloy 725. Specimens were prepared under three different heat treatment conditions and denoted as solution-annealed (SA), aged (AG) and over-aged (OA) samples. For single-crystal beams in an H-containing environment, all three heat-treated samples exhibited crack formation and propagation; however, crack propagation was more severe in the OA sample. The anodic extraction of H presented similar results as those under the H-free condition, indicating the reversibility of the H effect under the tested conditions. Bi-crystal microcantilevers bent under H-free and H-charged conditions revealed the significant role of the GB in the HE of the beams. The results indicated that the GB in the SA sample facilitated dislocation dissipation, whereas for the OA sample, it caused the retardation of crack propagation. For the AG sample, testing in an H-containing environment led to the formation of a sharp, severe crack along the GB path.

* *Corresponding author.*
E-mail address: iman.taji@ntnu.no (I. Taji).

https://doi.org/10.1016/j.ijhydene.2022.01.251

Introduction

Currently, there is an increasing demand for nickel superalloys as structural materials for miscellaneous applications. Nickel superalloys belong to a category of precipitation-hardened materials, which gain their strength by the formation of stable γ' and/or metastable γ'' precipitations in a face-centered cubic (FCC) nickel-based matrix. The formation of such precipitates is achieved through aging-based heat treatment under appropriate conditions. In addition to superior mechanical properties, nickel superalloys with high chromium content exhibit a higher corrosion resistance than other Ni alloys. Hydrogen (H), in contrast, is one of the elements responsible for nickel superalloy degradation in corrosive media due to H production, for example, when the electrolyte contains H_2S. Therefore, H embrittlement (HE) in nickel superalloys has always been an interesting scientific and engineering research topic.

The strength of polycrystalline alloys can be improved by methods influencing grain interior strength, such as solid solution and precipitation hardening or can be enhanced by altering the grain boundary (GB) type and GB segregation. Most studies on HE of nickel superalloys are based on polycrystalline alloys [1–3]. However, if a polycrystalline alloy is used, it is difficult to understand the effects of grain interior and GBs on the resistance of the material toward HE. This problem can be overcome by conducting a microcantilever bending test. An experiment could be performed in a single grain or GB strength can be evaluated by performing bi-crystal microcantilever bending tests, allowing the differentiation between the roles of the grain or GB in mechanical property enhancement. In addition, by in situ microcantilever bending tests, the effect of H on the mechanical properties can be assessed. This method has been successfully applied to S-doped GBs for demonstrating how S embrittled GBs in pure nickel [4].

In nickel superalloys, the high content of alloying elements in a solid solution, low stacking fault energy, and the presence of precipitates favor the planarity of the dislocation slip instead of the formation of dislocation cells and block structures [1,5]. The limiting dislocation cross-slip forces dislocations to remain in narrow, parallel slip bands called dislocation slip bands (DSBs) [6,7]. The formation of DSBs was further enhanced by the elevated content of H [6]. Because of the high dislocation density in DSBs, the intersections of DSBs with themselves and with GBs serve as favorable sites for crack formation. Zhang et al. [1] showed an example of fully transgranular fracture via DSBs in alloy 718. Voids were found to form primarily at the intersections of DSBs with different crystallographic orientations and propagated within the DSB route, crossing the GBs. In contrast, Ogawa et al. [8] presented an example of intergranular crack propagation in alloy 718. This discrepancy could be explained by the uneven distribution of H in the material, because H is distributed slowly in FCC solids, and it is likely that most of the grain interior is not strongly affected by H, as confirmed by Ref. [1]. In addition, different orientations of the GBs with respect to the applied stress direction could influence the analysis of the results in terms of crack initiation and propagation. GBs that are parallel to the direction of the applied stress are less susceptible to cracking, regardless of their type.

Another factor influencing fracture is the GB type and orientation angle. It is well known that special GBs are more resistant to fracture. Bechtle et al. [9] showed that GB engineering, by increasing the special GB fraction, markedly increased resistance toward HE. The resistance of special GBs toward stress corrosion cracking was also confirmed through 3D diffraction contrast tomography [10]. Lu and Wang showed that high-angle GBs, unlike low-angle GBs, contribute to dislocation pileup and the suppression of dislocation transmission, which can later lead to crack formation. A study on Alloy 725 showed that twin boundaries serve as crack initiation sites, but they also suppress crack propagation [11]. Therefore, it can be inferred that random high-angle GBs are more critical in inducing HE in nickel superalloys. In addition, random high-angle GBs are reported to be more prone to impurity segregation, which makes them more vulnerable to HE [4,12,13]. As a result, in this study, random high-angle GBs were selected to investigate intergranular HE by bi-crystal microcantilever bending tests. This method is also useful for understanding the interactions between DSBs and GBs although the results may not necessarily reflect the behavior of the bulk material.

In this study, single-crystal cantilevers were bent in situ to study the grain interior HE resistance of three samples of Alloy 725, which were subjected to three different heat treatment conditions according to API specifications. Then, three high-angle GBs were selected, and bi-crystal microcantilever bending was carried out to determine the influence of the GBs on the mechanical response and their interaction with H. Single and bi-crystal microcantilever bending results were analyzed and compared for samples subjected to the three different heat treatment conditions. The results help in understanding the interactions among DSB, GB, and H, and could be used to develop more H-resistant materials.

Materials and methods

Materials and sample preparation

Conventional Alloy 725 samples subjected to three different heat treatment conditions were used in this study. The solution-annealed (SA) sample was prepared by solution annealing at 1038 °C for 2 h. The aged (AG) sample was prepared by annealing the prior solution at 1038 °C for 2 h, followed by water quenching and heating up to 732 °C for 8 h, cooling in a furnace down to 621 °C, and maintenance at this temperature for 8 h [14]. For the over-aged (OA) sample, in order to coarsen the precipitates, the above heat treatment was repeated in which the aging temperature was increased from 732 °C to 780 °C. The heat-treated bars were cut into cylindrical parts with a diameter of 10 mm and a thickness of 8 mm. The samples to be used for electron backscatter scanning diffraction (EBSD) analysis and microcantilever milling were ground with emery paper up to grit number 2000 and then electropolished using 1 M methanolic H_2SO_4.

Thermal desorption spectroscopy

The H content of the samples was measured through thermal desorption spectroscopy (TDS). Thin samples with dimensions of 10 × 5 × 0.5 mm were used for H charging. The electrolyte was a mixture of phosphoric acid and glycerol (1:2 v/v). The samples were potentiostatically charged at −1050 mV vs. Ag/AgCl reference electrode at a temperature of 75 °C for 24 h. A G4 Phoenix DH system (Bruker Co.) coupled with a mass spectrometer was used for TDS. The total H content was analyzed by instantaneously exposing the sample to 800 °C for 600 s. In addition, the ramping test was conducted by gradually increasing the temperature from 30 to 800 °C at a heating rate of 0.5 K/s.

Microcantilever milling and bending

To investigate the inter- and intra-grain strength of the alloy samples, two series of cantilevers, single-crystal and bi-crystal ones, were milled. The criteria for bi-crystal selection are described elsewhere [4]. High-angle GBs with misorientation angles between 45 and 55°were selected to mill the bi-crystal beams. The selected GBs are shown in Fig. 1 and the corresponding GB information is summarized in Table 1. The micro-cantilevers were milled using an FEI Helios DualBeam™ focused ion beam (FIB) system. The cantilevers were bent using a Hysitron TI 950 Tribo-Indenter. The bending test was carried out under air (H-free), H-charged, and anodic conditions. The H charging of the samples was performed using a customized three-electrode cell prepared for the in situ electrochemical microcantilever bending test. The $Hg/HgSO_4$ electrode served as the reference electrode, and a platinum wire was used as the counter electrode. The samples were pre-charged for at least 2 h before the bending test started and were continued to be charged during bending. For H charging, the electrodes were cathodically polarized at −1500 vs. $Hg/HgSO_4$ (−1050 vs. Ag/AgCl). After bending the cantilevers under the H-charged condition, the sample was polarized anodically at 500 vs. $Hg/HgSO_4$ to extract all the charged H absorbed at the cathodic potential. After 2 h, while maintaining the anodic potential, a cantilever bending test was performed. The anodic potential was applied in the range of the passivity region of the alloy sample, and no corrosion was observed upon post-experiment microscopic investigation. To study the crack propagation path and plastic deformation, the cross-sections of the bent cantilevers were milled using the slice and view method. The slicing thickness was set to 100 nm. After each slicing, a high-resolution scanning electron microscopy (SEM) image was obtained.

Results

Transmission electron microscopy

No precipitation was observed for the SA sample. The transmission electron microscopy (TEM) images of the AG and OA samples are shown in Fig. 2. Fig. 2a shows the distribution of the ellipsoid γ'' in the sample. By prolonging the aging time or increasing the aging temperature, the sizes of the precipitates increase, which is known as coarsening. Studies have shown that the influence of increasing the temperature, which is implemented in this study to produce OA samples, is more significant than the effect of time [15–18]. In the OA sample, as shown in Fig. 2b, fewer precipitates were present compared to those in the same area of the AG samples, Fig. 2b, indicating coarsening and enhancement of spacing between the precipitates.

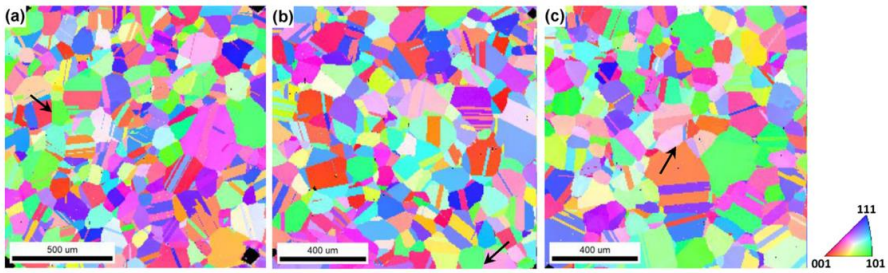

Fig. 1 – EBSD images of the (a) SA, (b) AG and (c) OA samples. The arrows show the selected GB for cantilever milling.

Table 1 – Measured GB misorientation angle and corresponding information in SA, API and OA samples.

GB ID	Misorientation angle (°)	Axis			Sigma	Plane 1 (fixed grain)			Plane 2 (free-standing grain)		
		h	*k*	*l*		*u*	*v*	*w*	*u*	*v*	*w*
SA	52.7	0	19	−15	–	−10	25	−9	−3	7	−1
AG	44.7	1	−6	−10	–	5	−14	20	21	14	−15
OA	49.7	23	18	−5	–	3	−6	−2	1	−13	27

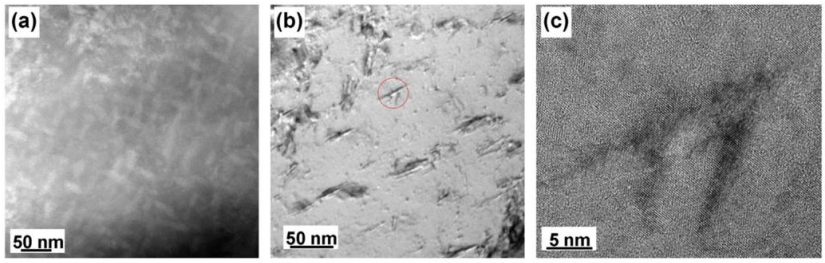

Fig. 2 – TEM images of the (a) AG and (b) OA samples alongside (c) a high-resolution image of a precipitate are shown, with a red circle on the over-aged sample image. (For interpretation of the references to color in this figure legend, the reader is referred to the Web version of this article.)

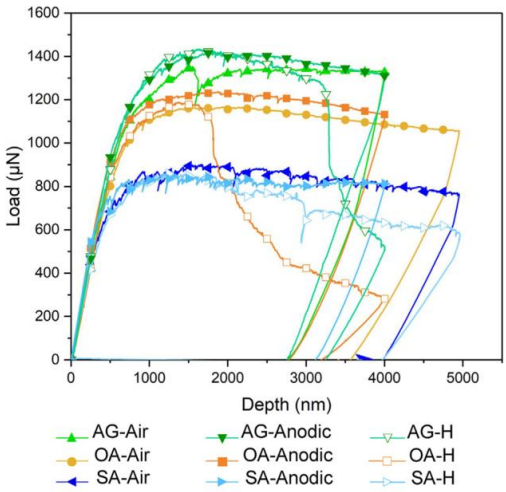

Fig. 3 – L-D curves of the single-crystal micro-cantilevers bent under the air, H-charged, and anodic conditions.

Single-crystal microcantilever bending

Load-displacement curves

The microcantilever bending test for single-crystal beams was carried out under air, H-charged, and anodic conditions. An anodic test was performed to determine whether H is the only influencing factor or whether there is another parameter in the electrolyte that affects the mechanical properties of the alloy samples. In addition, testing under the anodic condition helps to examine the reversibility of the effect of H on the mechanical response. The comparison of the load-displacement (L-D) curves under the anodic and air conditions (Fig. 3) reveals that almost no noticeable difference can be distinguished. Therefore, it is rational to conclude that the electrolyte has no effect on the mechanical response of the bending test. Under the cathodic condition, in contrast, the charged H affects the mechanical properties. Therefore, because the air and anodic conditions afford similar results, testing under the anodic condition will not be conducted for bi-crystal microcantilever bending.

The load in the L-D curves of the SA sample reached nearly 800 μN under the air condition and continued almost consistently until the end of the test, that is, 5 μm displacement. For the SA sample under the H-charged condition, however, the load exhibited a continuous decreasing trend during plastic deformation. Load reduction of approximately 200 μN was observed from 1 to 5 μm displacement under the H-charged condition. The maximum load in the L-D curves of the AG sample reached up to 1400 μN, which is 600 μN higher than that observed for the SA samples. The increase in strength is a result of the precipitation-hardening effect of the γ'' particles after the aging heat treatment. Under the H-charged condition, after 3.3 μm displacement, a sharp load drop can be observed in the L-D curve. The formation of a crack during the bending test causes the reduction in the volume of the material, which is responsible for the tolerated load. Therefore, to compenickel superalloyte the constant displacement constrain defined for the test, the maximum tolerated load would be decreased, causing a drop in the L-D curve. The sudden load drop in the L-D curve of the OA sample under the H-charged condition occurs at lower displacements (approximately 1.6 μm) compared to that observed for the AG sample, which indicates a higher susceptibility to HE. The maximum load in the L-D curve of the OA sample under the air condition is approximately 1200 μN, which is 200 μN lower than that of the AG sample.

Post-bending SEM images

The post-bending SEM images of the single-crystal micro-cantilevers are shown in Fig. 4. As illustrated by the L-D curves, the bending results under the anodic condition indicate a behavior similar to that under the air condition. The appearance of plasticity ahead of the notch in the three heat-treated alloy samples at anodic potential is similar to that under the air condition. It is rational to conclude that by applying an anodic potential, all H atoms present in the material because of H charging would diffuse. This phenomenon shows the reversibility of the effect of H on the experimental parameters focused in this study. Under the H-free condition, DSBs are the main features that appear on the surface. They are more frequently observed in SA cantilevers with lower DSB spacing than in the other heat-treated cantilevers. In contrast, the least frequent DSBs were revealed on the OA sample surface after the bending test. For all three samples under the H-free condition, the notch head was blunted after

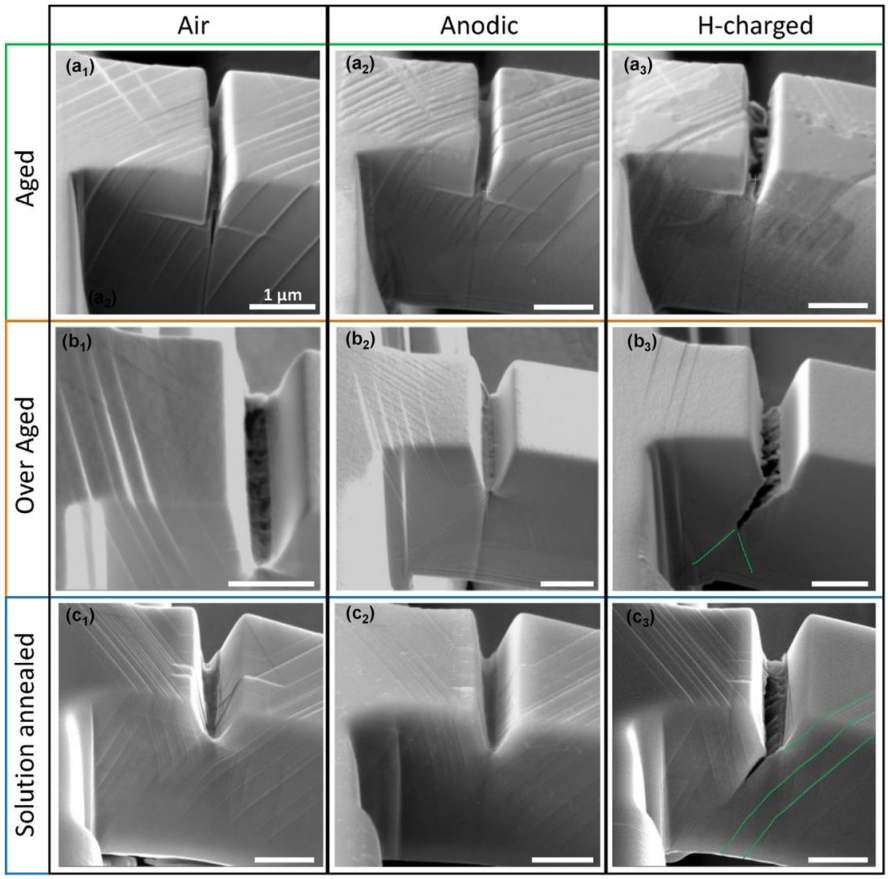

Fig. 4 – Post-deformation SEM images of the single-crystal micro-cantilevers under the air, H-charged, and anodic conditions.

the test and did not propagate into the material. Under the H-charged condition, however, a crack was formed at the notch root in all three heat-treated samples.

Bi-crystal microcantilever bending

Fig. 5 shows the L-D curves and corresponding post-bending SEM images of the bi-crystal micro-cantilevers. The axis scales for the L-D curves were sketched in a similar manner, to compare the maximum load difference between the corresponding curves of the three heat-treated samples. The L-D curve of the OA sample represents the highest load of approximately 1600 μN, the maximum loads of the AG and SA samples are 1400 μN and 600 μN, respectively. Under the H-charged condition, a decrease in the maximum load can be seen for all the three heat-treated sampled, similar to the results of single-crystal microcantilever bending test. This maximum load reduction was most evident for the OA sample.

No signs of cracks or voids could be observed on the surface of the SA-heat-treated cantilever bent under the H-free and H-charged conditions (Fig. 5a_2 and a_3). On the other hand, under the H-charged condition, a clear intergranular crack was formed on the beams of the AG and OA samples. Intergranular cracking in both the AG and OA samples was accompanied by plastic deformation revealed by DSBs on the cantilever surface. Under the air condition, especially for the AG sample, the formed DSBs at both grains adjacent to the GB interact and stop at the GB.

Hydrogen content

The TDS results after 24 h of cathodic H charging are shown in Fig. 6. Due to the lack of precipitates serving as trapping sites,

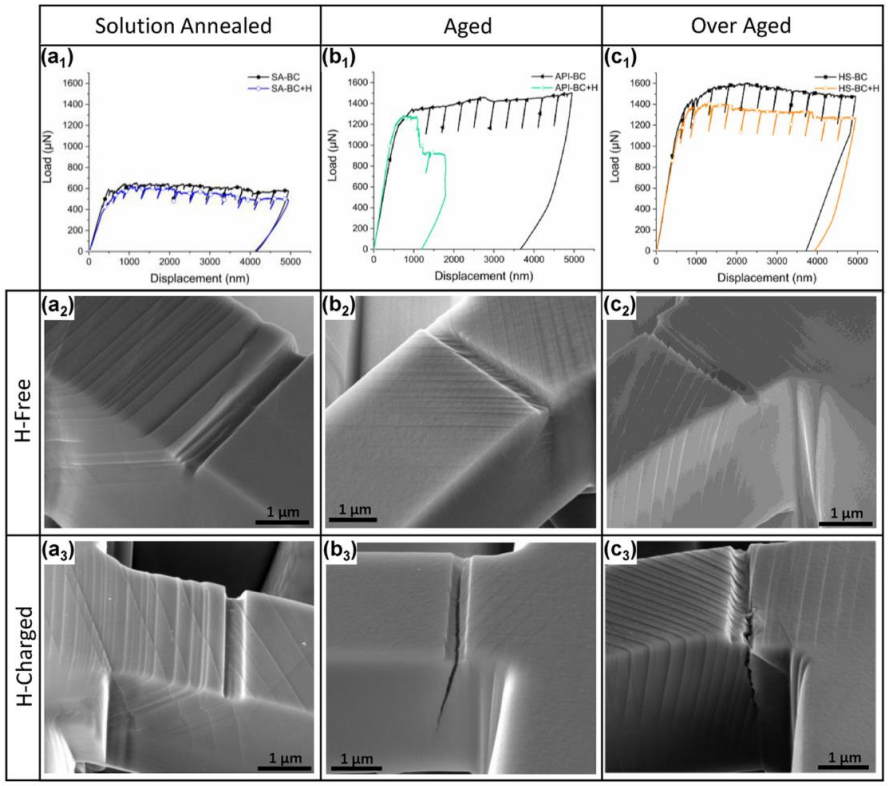

Fig. 5 – L-D curves and corresponding post-deformation SEM images of the cantilevers bent under the H-free and H-charged conditions.

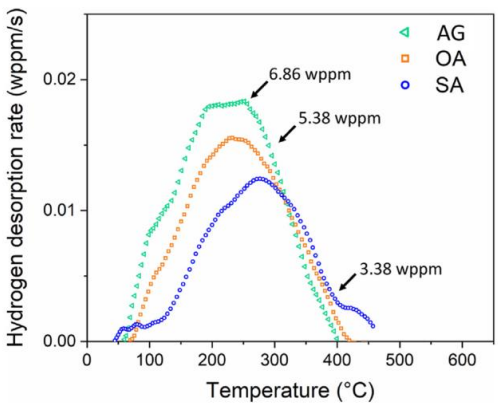

Fig. 6 – Hydrogen desorption spectra of the three heat-treated samples obtained from TDS.

the SA sample absorbed the lowest amount of H compared to the other samples. The AG sample absorbed more H than the OA sample. The AG sample had a larger surface area of the precipitate–matrix interface than the OA sample. The precipitates in the AG sample are finer and more widely distributed in the matrix, whereas in the OA sample, the precipitates are coarser and less scattered.

Discussion

Reversibility of hydrogen traps

The comparison of the L-D curves of the H-charged and air-bent cantilevers with those under the H-extracted (anodic) condition in Fig. 6 confirmed the reversibility of H interaction with the nickel superalloy crystals. The anodic extraction of H has been conducted in several studies to verify the reversibility/irreversibility of H diffusion [19–21]. A similar conclusion was reached by in situ nanoindentation on Alloy 718 [21], in which, after 2 h of H charging, the hardness value recovered to the air condition value upon the application of anodic potential. This effect shows that the trapped H at the γ''/matrix interface is mostly reversible. However, it should be noted that there are some particles in nickel superalloys, such as carbides, which could act as irreversible trap sites for H atoms [22]. Turnbull et al. [23] verified the reversibility of H trapped at both γ' and γ'' particles in nickel superalloys. They measured

the binding energy of H with the particles to range from −31 to −37 and from −23 to −27 kJ mol^{-1}for γ' and γ'', respectively. These values are considerably higher than that (−58 kJ mol^{-1}) considered as the energy criterion for reversible/irreversible trap transitions [24]. It should be noted that the dominant particles in the alloys used in this study are mostly γ'', as depicted by TEM (Fig. 2), which are more reversible than γ', according to the mentioned binding energy values.

Strength of single-crystal cantilevers

Fig. 3 shows that in situ charging with H contributed to a decrease in the yield strength and maximum load of the L-D curves, known as the H-softening effect. The corresponding yield point and maximum load are listed in Table 2. This phenomenon is attributed to the decrease in the internal shear stress of DSB walls [25] in pure Ni. However, the H-softening effect in nickel superalloys is negligible in relation to that in pure Ni. Owing to the presence of γ' and γ'' particles and high contents of alloying elements, Nickel superalloys are susceptible to planar slip and DSB formation [5,7].

The precipitation of γ'' phases was responsible for the increase in the strength of the AG and OA samples in relation to that of the SA sample. However, coarsening of the precipitates in the OA sample reduced the maximum load in the L-D curves in Fig. 3. This is consistent with the results of previous in situ nanoindentation studies [21], wherein Alloy 718, which was subjected to over-aging, had lower hardness because of larger but fewer γ' particles dispersed in the matrix. The number of obstacles in the path of the dislocations controls the stress required for the glide. Therefore, by decreasing the obstacles in the OA sample, a lower maximum load was expected. In addition, the precipitate–matrix interface is known to act as a reversible trap in nickel superalloys [22, 26]. The reduction in the surface area of the precipitates in the OA sample due to coarsening resulted in the absorption of lower amount of H than that in the AG sample, as can be observed in Fig. 6. The coarsening of the γ'' precipitates also led to a reduction in the maximum tolerated strength represented by the L-D curves. The reduction in the yield strength due to the coarsening of the precipitates is a common phenomenon that stems from the large spacing between precipitates [27, 28]. According to the Friedel model [29], the flow stress, σ_f, obeys the following relationship:

$$\sigma_f \propto \frac{1}{L} \tag{1}$$

where L is the distance between the obstacles.

Table 2 – Yield points and maximum loads extracted from the single-crystal L-D curves.

ID	Air		H-charged	
	Yield point	Maximum load	Yield point	Maximum load
SA	865	899	751	855
AG	1322	1432	1207	1347
OA	1126	1237	1086	1186

Due to the lower content of H and lower maximum strength of the OA sample than those of the AG sample, a lower HE severity was expected in the former. However, contrary to this expectation, the AG sample showed more durability against HE according to the L-D curves. A cross-sectional view of the bent specimens under the H-charged condition after slicing with the FIB, Fig. 7(c_2), also depicted the long-distance propagation of the crack in the OA sample, unlike that observed in the AG sample (Fig. 7(b_2)). It has been reported that coarse precipitates in the matrix can serve as more favorable sites for void formation compared to small precipitates [30]. In addition, it is well documented that the coarser the precipitates, the greater the mismatch between the matrix and precipitate [31]. These mismatched sites create an elastic strained area that could be a trap site for H [32]. Therefore, the H content of the material increased, which further increased the crack initiation probability in the interface areas and contributed to the severe cracking of the OA sample.

Contribution of GBs

The comparison of the single and bi-crystal cantilever L-D curves for the SA sample confirms that the latter has an approximately 200 μN lower strength. Based on the well-known Hall-Petch relation, the strength can be increased by incorporating a GB in the system. The dislocations pile behind the GB; therefore, high stress is required to overcome the resistance of the GB toward the dislocation transmission, which results in the increase in the overall strength of the material. In contrast, in this case, the strength was decreased by adding a GB to the cantilever. The reason for such a decrease in the strength of the bi-crystal cantilever can be attributed to the limited volume of the cantilever, especially in the SA sample, wherein there is a lack of favorable dislocation nucleation sites. Instead of being a pileup area, the GB can be regarded as an additional defect in which dislocation nucleation can occur [33]. In addition, dislocations can also be annihilated at a single GB provided in the microcantilever [34]. Therefore, by comparing the single and bi-crystal micro-cantilevers, it can be deduced that the GB, in this case, did not increase the strength, but resulted in softening. The SEM images obtained from the cross-sectional slicing of the cantilevers support this explanation. In a single-crystal cantilever, the accumulation of dislocations and strain concentration can be distinguished by the color contrast under the notch area, as shown in Fig. 7(a_1). In contrast, in bi-crystal cantilevers (Fig. 7(a_3)), no sign of pileup or strain concentration could be observed. Therefore, it seems that the GB serves as a source for the annihilation of the dislocations, which relaxes strain accumulation. This explanation can also elucidate the mechanism underlying crack formation induced by H charging in a single-crystal cantilever, while the bi-crystal cantilever remains almost intact. It should be noted that there was a sign of the formation of nano-voids at the intersection of the GB path and notch route, which is depicted by the white arrow in Fig. 7(a_4). However, because no dislocation pileup and no strain concentration occurred in the bi-crystal cantilever, the formed voids did not tend to propagate. This void formation could be responsible for the strength decay

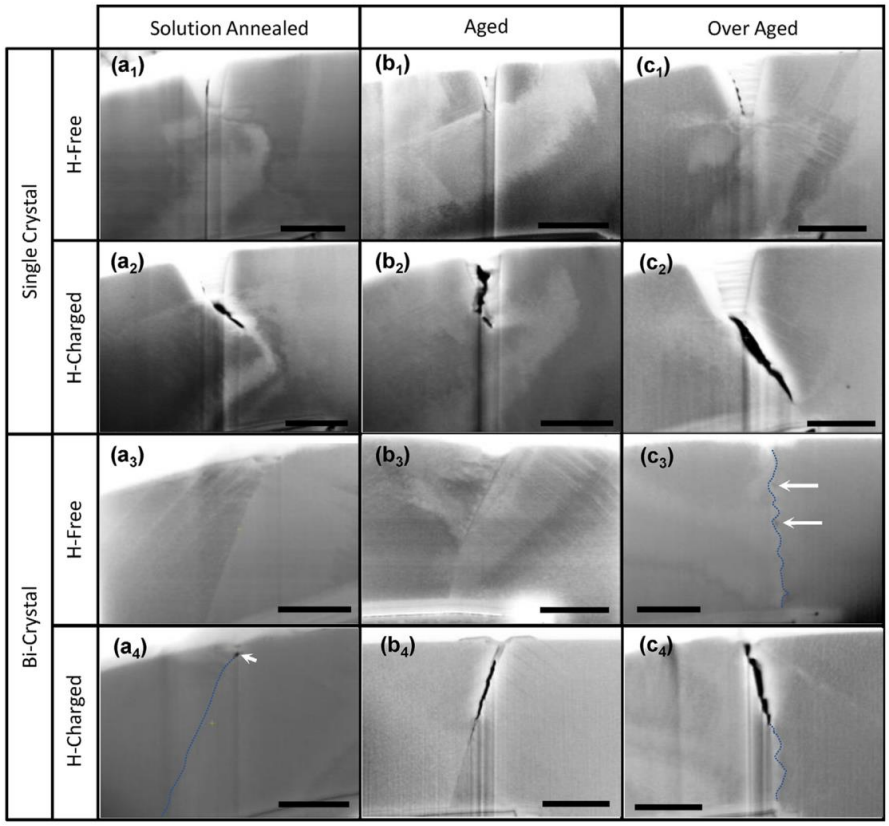

Fig. 7 – Cross-sectional SEM images of the single- and bi-crystal cantilevers after slicing with the FIB.

observed in the L-D curves of the corresponding beams in Fig. 5(a_1).

Based on Fig. 5(b_1), the bi-crystal microcantilever made on the AG sample bent in air exhibited mild continuous hardening in the L-D curve. This continuous hardening in the presence of a GB occurs as a result of strain hardening and dislocation pileup at the GB. A cross-sectional SEM image of this cantilever is shown in Fig. 7(b_3) wherein the pileup area can be observed. The hydrogenation of the sample upon cathodic charging resulted in the formation of a sharp crack and semi-cleavage failure, as depicted in Fig. 5(b_3). The crack was formed exactly at the GB route. H is well known to decrease the cohesive energy of the GB, leading to easier debonding of the atoms, which is categorized as the Hydrogen enhanced decohesion (HEDE) mechanism [35]. However, it should be noted that crack advancement was under the control of the local plastic area formed at the GB-DSB intersections, which are depicted by the edge formation in the crack route in Fig. 7(b_4) as is already discussed in the introduction section.

The L-D curve of the OA bi-crystal cantilever bent in air (Fig. 5(c_1)) represents a load increase in relation to that of the AG sample (Fig. 5(b_1)). This increase could be explained by the cross-sectional images of the bent cantilevers. Fig. 7(c_3) shows the air-bent cantilever of the OA sample. As can be seen, the GB has a serrated form. It has been proven that the formation of a serrated GB significantly improves the mechanical properties of materials [36,37]. The presence of the serrated GB contributes to the higher lattice strain around the GB [38]; hence, an increase in the tolerated maximum stress was revealed in the L-D curve. The formation of the serrated GB is related to the coarser γ'' precipitates that were formed at the GBs in the OA sample. These coarse precipitates pin the GB at the points where they are formed, while the rest can move and grow during solidification [39]. The arrows in Fig. 7(c_3) show two precipitates which have formed around the GB inducing the serration. In agreement with the results of this study, Alabbad et al. [40] showed that the larger γ' formed at the GB resulted in higher amplitudes and wavelengths of the serration along the boundary. The presence of the serrated GB can readily improve the mechanical resistance by retarding crack growth, impeding void accumulation, and lengthening the crack propagation path [38,41]. It also shows more resistance toward GB sliding [42]. In the cross-sectional image shown in Fig. 7(c_4), it can be seen that the serrated form of the GB makes it difficult for the crack to propagate. Therefore, the corresponding L-D curve shows no sudden drop in load. It should be noted that Fig. 7(c_4) depicts the cantilever from one side and

almost from the middle of the cantilever to the other side. No crack was formed at the GB.

Summary of the mechanisms involved in microcantilever bending tests

The total strength of the material (σ_{total}) can be assumed to be a summation of the solid solution (σ_{ss}), precipitation (σ_{prec}), and GB (σ_{gb}) strengthening:

$$\sigma_{total} = \sigma_{ss} + \sigma_{prec} + \sigma_{gb} \quad (2)$$

In a polycrystalline material, it has been shown that the contribution of precipitation strengthening is significantly larger than that of the two others [28]. This result is in good agreement with the microcantilever test results. If the results of our previous study on pure nickel [4] were compared with those of an SA single-crystal sample, the contribution of σ_{ss} would be accounted to be approximately 400 μN enhancement in maximum load strength. Precipitation hardening in the AG single-crystal sample, however, increases the strength by about 600 μN compared with that in the SA sample. Upon coarsening of the precipitates, the strengthening effect of the precipitates in the OA single-crystal sample was found to weaken.

Furthermore, the role of the GB structure in strengthening is different. The SA sample served as a dislocation dissipation site or a defect, facilitating the annihilation of the dislocations; therefore, in Eq. (2) the term σ_{gb} has a negative sign, resulting in the softening of the cantilever. For the AG bi-crystal cantilever bent in air and owing to the large contribution of precipitation hardening, σ_{gb} does not have a significant effect, even though its influence could be distinguished by work hardening and the continuous increase in the load in the L-D curve. The SEM images revealed that the dislocation accumulation behind the GBs led to this behavior. In the OA sample, however, the GB contribution resulted in approximately 400 μN hardening under the air condition. This increase in strength, according to the SEM cross-sectional observation of the cantilevers, was related to the serrated GB formed due to the coarse GB precipitates in the OA sample.

Conclusion

In this study, single and bi-crystal micro-cantilevers were milled out of three heat-treated samples. The solution-annealed (SA), aged (AG), and over-aged (OA) samples were used to investigate the micro-mechanical properties. The cantilevers were bent under H-free and in situ H-charged conditions. The main results were as follows:

- The application of anodic potential after cathodic charging resulted in the de-charging of H from the beams. Therefore, similar L-D curves were obtained for cantilevers bent under anodic and air conditions. This result suggested the reversibility of H charging under the tested conditions.
- Due to the presence of fine, dispersed precipitates in the AG sample, the maximum load in the L-D curves of single-crystal cantilevers was higher in the AG sample than in the OA sample. However, under the H-charged condition, the OA sample experienced more severe cracking. The load in L-D curve of OA sample fell down after about 1500 nm displacement, while it dropped at about 3200 nm for AG sample.
- Under the H-charged condition, for the SA single-crystal sample, a crack was formed during bending, which propagated smoothly in the DSB route. Under the same condition for the bi-crystal sample, no cracks were formed in the H environment. The comparison of the single and bi-crystal bent cantilevers of the SA sample under the H-free condition revealed a softening effect in the bi-crystal cantilevers.
- A sharp continuous crack was formed in the AG bi-crystal cantilever after H charging, whereas in the OA bi-crystal sample, the formed crack was not able to propagate. It was found that the serrated GB formed in the AG sample due to coarse GB precipitates was responsible for this phenomenon.

Declaration of competing interest

The authors declare that they have no known competing financial interests or personal relationships that could have appeared to influence the work reported in this paper.

Acknowledgments

The authors gratefully acknowledge the financial support under the scope of the COMET program within the K2 Center "Integrated Computational Material, Process and Product Engineering (IC-MPPE)" (Project No 859480). This program is supported by the Austrian Federal Ministries for Climate Action, Environment, Energy, Mobility, Innovation, and Technology (BMK) and for Digital and Economic Affairs (BMDW), represented by the Austrian Research Funding Association (FFG), and the federal states of Styria, Upper Austria, and Tyrol. The financial support of the voestalpine BÖHLER Edelstahl GmbH & Co KG and Equinor ASA is gratefully acknowledged. The Research Council of Norway is acknowledged for its support of the Norwegian Micro- and Nano-Fabrication Facility, NorFab (Project No. 245963/F50).

Appendix A. Supplementary data

Supplementary data to this article can be found online at https://doi.org/10.1016/j.ijhydene.2022.01.251.

REFERENCES

[1] Zhang Z, Obasi G, Morana R, Preuss M. Hydrogen assisted crack initiation and propagation in a nickel-based superalloy. Acta Mater 2016;113:272–83.
[2] Harris ZD, Bhattacharyya JJ, Ronevich JA, Agnew SR, Burns JT. The combined effects of hydrogen and aging condition on the deformation and fracture behavior of a precipitation-

hardened nickel-base superalloy. Acta Mater 2020;186:616–30.
[3] Lu X, Ma Y, Wang D. On the hydrogen embrittlement behavior of nickel-based alloys: alloys 718 and 725. Mater Sci Eng 2020;792:139785.
[4] Hajilou T, Taji I, Christien F, He S, Scheiber D, Ecker W, Pippan R, Razumovskiy VI, Barnoush A. Hydrogen-enhanced intergranular failure of sulfur-doped nickel grain boundary: in situ electrochemical micro-cantilever bending vs. dft. Mater Sci Eng 2020;794:139967.
[5] Xiao L, Chen D, Chaturvedi M. Shearing of γ'' precipitates and formation of planar slip bands in inconel 718 during cyclic deformation. Scripta Mater 2005;52(7):603–7.
[6] Wen M, Fukuyama S, Yokogawa K. Hydrogen-affected cross-slip process in fcc nickel. Phys Rev B 2004;69(17):174108.
[7] Hong SI, Laird C. Mechanisms of slip mode modification in fcc solid solutions. Acta Metall Mater 1990;38(8):1581–94.
[8] Ogawa Y, Takakuwa O, Okazaki S, Okita K, Funakoshi Y, Matsunaga H, Matsuoka S. Pronounced transition of crack initiation and propagation modes in the hydrogen-related failure of a ni-based superalloy 718 under internal and external hydrogen conditions. Corrosion Sci 2019;161:108186.
[9] Bechtle S, Kumar M, Somerday BP, Launey ME, Ritchie RO. Grain-boundary engineering markedly reduces susceptibility to intergranular hydrogen embrittlement in metallic materials. Acta Mater 2009;57(14):4148–57.
[10] King A, Johnson G, Engelberg D, Ludwig W, Marrow J. Observations of intergranular stress corrosion cracking in a grain-mapped polycrystal. Science 2008;321(5887):382–5.
[11] Seita M, Hanson JP, Gradečak S, Demkowicz MJ. The dual role of coherent twin boundaries in hydrogen embrittlement. Nat Commun 2015;6(1):1–6.
[12] Hazarabedian MS, Iannuzzi M. The role of nano-sized intergranular phases on nickel alloy 725 brittle failure. NPJ Mater Degrad 2021;5(1):1–9.
[13] Raabe D, Herbig M, Sandlöbes S, Li Y, Tytko D, Kuzmina M, Ponge D, Choi P-P. Grain boundary segregation engineering in metallic alloys: a pathway to the design of interfaces. Curr Opin Solid State Mater Sci 2014;18(4):253–61.
[14] Physical metallurgy of alloys 718, 925, 725, and 725HS for service in aggressive corrosion environments. arXiv; 2003. Vol. All days of NACE CORROSION, nACE-03126, https://onepetro.org/NACECORR/proceedings-pdf/CORR03/All-CORR03/NACE-03126/1876627/nace-03126.pdf.
[15] Whelchel RL, Kelekanjeri VSKG, Gerhardt RA, Ilavsky J. Effect of aging treatment on the microstructure and resistivity of a nickel-base superalloy. Metall Mater Trans 2011;42(5):1362–72.
[16] Zhao S, Xie X, Smith GD, Patel SJ. Microstructural stability and mechanical properties of a new nickel-based superalloy. Mater Sci Eng 2003;355(1–2):96–105.
[17] Zhang F, Cao W, Zhang C, Chen S, Zhu J, Lv D. Simulation of co-precipitation kinetics of γ' and γ'' in superalloy 718. In: Proceedings of the 9th international symposium on superalloy 718 & derivatives: energy, aerospace, and industrial applications. Springer; 2018. p. 147–61.
[18] Han Y-f, Deb P, Chaturvedi M. Coarsening behaviour of γ''- and γ'-particles in inconel alloy 718. Met Sci 1982;16(12):555–62.
[19] Wang D, Lu X, Deng Y, Guo X, Barnoush A. Effect of hydrogen on nanomechanical properties in fe-22mn-0.6 c twip steel revealed by in-situ electrochemical nanoindentation. Acta Mater 2019;166:618–29.
[20] Wang D, Lu X, Wan D, Li Z, Barnoush A. In-situ observation of martensitic transformation in an interstitial metastable high-entropy alloy during cathodic hydrogen charging. Scripta Mater 2019;173:56–60.
[21] Stenerud G, Hajilou T, Olsen JS, Taji I, Barnoush A, Johnsen R. The effect of hydrogen on the nanoindentation behavior of heat treated 718 alloy. Metals 2020;10(11):1451.
[22] Turnbull A, Ballinger R, Hwang I, Morra M, Psaila-Dombrowski M, Gates R. Hydrogen transport in nickel-base alloys. Metall Trans A 1992;23(12):3231–44.
[23] Rezende M, Araujo L, Gabriel S, Dos Santos D, De Almeida L. Hydrogen embrittlement in nickel-based superalloy 718: relationship between $\gamma' + \gamma''$ precipitation and the fracture mode. Int J Hydrogen Energy 2015;40(47):17075–83.
[24] Pound B. Hydrogen trapping in precipitation-hardened alloys. Acta Metall Mater 1990;38(12):2373–81.
[25] Magnin T, Bosch C, Wolski K, Delafosse D. Cyclic plastic deformation behaviour of ni single crystals oriented for single slip as a function of hydrogen content. Mater Sci Eng 2001;314(1–2):7–11.
[26] Galliano F, Andrieu E, Blanc C, Cloue J-M, Connetable D, Odemer G. Effect of trapping and temperature on the hydrogen embrittlement susceptibility of alloy 718. Mater Sci Eng 2014;611:370–82.
[27] Pandey P, Kashyap S, Palanisamy D, Sharma A, Chattopadhyay K. On the high temperature coarsening kinetics of γ' precipitates in a high strength co37. 6ni35. 4al9. 9mo4. 9cr5. 9ta2. 8ti3. 5 fcc-based high entropy alloy. Acta Mater 2019;177:82–95.
[28] Harte A, Atkinson M, Smith A, Drouven C, Zaefferer S, da Fonseca JQ, Preuss M. The effect of solid solution and gamma prime on the deformation modes in ni-based superalloys. Acta Mater 2020;194:257–75.
[29] Swinburne T, Dudarev S. Kink-limited orowan strengthening explains the brittle to ductile transition of irradiated and unirradiated bcc metals. Phys Rev Mater 2018;2(7):073608.
[30] Balikci E, Mirshams R, Raman A. Fracture behavior of superalloy in738lc with various precipitate microstructures. Mater Sci Eng 1999;265(1–2):50–62.
[31] Barjesteh MM, Abbasi SM, Madar KZ, Shirvani K. The effect of heat treatment on characteristics of the gamma prime phase and hardness of the nickel-based superalloy rene® 80. Mater Chem Phys 2019;227:46–55.
[32] Zhang Z, Moore KL, McMahon G, Morana R, Preuss M. On the role of precipitates in hydrogen trapping and hydrogen embrittlement of a nickel-based superalloy. Corrosion Sci 2019;146:58–69.
[33] Soer W, Aifantis K, De Hosson JTM. Incipient plasticity during nanoindentation at grain boundaries in body-centered cubic metals. Acta Mater 2005;53(17):4665–76.
[34] Kim Y, Lee S, Jeon JB, Kim Y-J, Lee B-J, Oh SH, Han SM. Effect of a high angle grain boundary on deformation behavior of al nanopillars. Scripta Mater 2015;107:5–9.
[35] Djukic MB, Bakic GM, Zeravcic VS, Sedmak A, Rajicic B. The synergistic action and interplay of hydrogen embrittlement mechanisms in steels and iron: localized plasticity and decohesion. Eng Fract Mech 2019;216:106528.
[36] Hong HU, Jeong HW, Kim IS, Choi BG, Yoo YS, Jo CY. Significant decrease in interfacial energy of grain boundary through serrated grain boundary transition. Phil Mag 2012;92(22):2809–25.
[37] Wisniewski A, Beddoes J. Influence of grain-boundary morphology on creep of a wrought ni-base superalloy. Mater Sci Eng 2009;510:266–72.
[38] Kontis P, Alabort E, Barba D, Collins DM, Wilkinson AJ, Reed RC. On the role of boron on improving ductility in a new polycrystalline superalloy. Acta Mater 2017;124:489–500.

[39] Qiu C, Andrews P. On the formation of irregular-shaped gamma prime and serrated grain boundaries in a nickel-based superalloy during continuous cooling. Mater Char 2013;76:28–34.
[40] Alabbad B, Li L, Tin S. Controlling the grain boundary morphology and secondary γ′ precipitate size distribution in ni-base superalloys. J Alloys Compd 2019;775:931–41.
[41] Yoon J, Jeong H, Yoo Y, Hong H. Influence of initial microstructure on creep deformation behaviors and fracture characteristics of haynes 230 superalloy at 900 c. Mater Char 2015;101:49–57.
[42] Carter JL, Kuper MW, Uchic MD, Mills MJ. Characterization of localized deformation near grain boundaries of superalloy rené-104 at elevated temperature. Mater Sci Eng 2014;605:127–36.

Paper II: Hydrogen Assisted Intergranular Cracking of Alloy 725: The Effect of Boron and Copper Alloying

Iman Taji[a,*], Tarlan Hajilou[a], Anna Sophie Ebner[b], Daniel Scheiber[c], Shabnam Karimi[a], Ernst Plesiutschnig[d], Werner Ecker[c], Afrooz Barnoush[a,e], Verena Maier-Kiener[b], Roy Johnsen[a], Vsevolod I. Razumovskiy[c]

[a]Department of Mechanical and Industrial Engineering, Norwegian University of Science and Technology, No. 7491 Trondheim, Norway

[b]Department Materials Science, Montanuniversität Leoben, Jahnstraße 12, 8700 Leoben, Austria

[c]Materials Center Leoben Forschung GmbH, Roseggerstraße 12, 8700 Leoben, Austria

[d]Voestalpine Böhler Edelstahl GmbH & Co KG, Mariazellerstraße 25, 8605 Kapfenberg, Austria

[e]Qatar Environment and Energy Research Institute (QEERI), Hamad Bin Khalifa University (HBKU) P.O. Box 34110, Doha, Qatar

Corrosion Science, 203 (2022), 110331.

https://doi.org/10.1016/j.corsci.2022.110331.

Corrosion Science 203 (2022) 110331

Contents lists available at ScienceDirect

Corrosion Science

journal homepage: www.elsevier.com/locate/corsci

Hydrogen assisted intergranular cracking of alloy 725: The effect of boron and copper alloying

Iman Taji [a,*], Tarlan Hajilou [a], Anna Sophie Ebner [b], Daniel Scheiber [c], Shabnam Karimi [a], Ernst Plesiutschnig [d], Werner Ecker [c], Afrooz Barnoush [a,e], Verena Maier-Kiener [b], Roy Johnsen [a], Vsevolod I. Razumovskiy [c]

[a] Department of Mechanical and Industrial Engineering, Norwegian University of Science and Technology, No. 7491, Trondheim, Norway
[b] Department Materials Science, Montanuniversität Leoben, Jahnstraße 12, 8700 Leoben, Austria
[c] Materials Center Leoben Forschung GmbH, Roseggerstraße 12, 8700 Leoben, Austria
[d] Voestalpine Böhler Edelstahl GmbH & Co KG, Mariazellerstraße 25, 8605 Kapfenberg, Austria
[e] Qatar Environment and Energy Research Institute (QEERI), Hamad Bin Khalifa University (HBKU), P.O. Box 34110, Doha, Qatar

ARTICLE INFO

Keywords:
Hydrogen embrittlement
Nickel-based superalloy
Density functional theory
Micro-scale testing
Atom probe tomography

ABSTRACT

To overcome the Hydrogen embrittlement (HE) susceptibility of the standard Alloy 725 (Mod A), two alloys with minor alloying modifications with B (Mod B) and B+Cu (Mod C) were produced. Then, the intergranular cracking susceptibility was investigated on bi-crystal beams by electrochemical in situ micro-cantilever bending test. The atom probe tomography and first principles calculations were employed to capture and calculate the grain boundary (GB) segregation and its effect on the GB cohesion. Cross-sectional view of the bent beams showed the superior resistance of Mod B against HE by facilitating the GB dislocation transfer/generation. While bending Mod A sample in hydrogen environment leads to form a sharp intergranular cracking, Mod B showed some nano-voids/cracks mostly in dislocation slip bands and rarely in GB path. However, a reduction of strength was observed in load-displacement (L-D) curves of Mod B. The addition of Cu, although not participated in GB segregation, compromised the lost strength of Mod B. In Mod C, after bending in H-charged condition, the nano-voids were formed in GB, but no load drop in L-D curves nor crack propagation in post-deformation observations was detected. The micro-alloying proposed in this study could be an important contribution to the future developing of H resistant alloys via GB segregation engineering.

1. Introduction

A wide range of nickel-based superalloy (NBS) applications ranging from high to low temperatures and from aerospace to submarine environments [1,2] leads to rather strict material quality requirements. One of them is resistance to hydrogen embrittlement (HE) [3]. Being exposed to hydrogen-containing environments, some NBS have a tendency toward intergranular failure [4]. Grain boundaries (GB) have been found to play a key role in this fracture mode and considered by many as the main element of the alloy microstructure responsible for material's damage due to HE [5–7]. For instance, a study of Alabort et al. [8] has shown that GB resistance to fracture can determine to a large extend both strength and ductility of NBS.

Presence of H at GB in NBS leads to material failure along GB in most cases [9,10] which is often associated with the hydrogen enhanced decohesion (HEDE) mechanism by reducing the material's cohesive strength induced by H atoms [11–13]. A number of other studies have shown that H can lead to an increase of the dislocation nucleation rate [14,15]. It is also known that H promotes the slip planarity by reducing the equilibrium distance between dislocations [16] which results in extensive dislocation slip activation. Therefore, impingement of the GB with the extensive dislocations could raise up the stress accumulation at the GB and lead to intergranular fracture [13]. Furthermore, presence of H is reported to confine the high stress-bearing plastic area around the crack tip enhancing the quasi-cleavage fracture [17,18]. A number of recent publications have demonstrated that GB structure itself may be an important factor determining material's susceptibility to HE and therefore deserves special attention.[19–21].

Recent progress in the field of hydrogen-GB interaction laid the basis for such material design concepts as GB engineering [22] and GB

* Corresponding author.
E-mail address: Iman.taji@ntnu.no (I. Taji).

https://doi.org/10.1016/j.corsci.2022.110331
Received 6 September 2021; Received in revised form 29 March 2022; Accepted 21 April 2022
Available online 25 April 2022

segregation engineering [23]. These approaches attempt to improve material properties by increasing the ratio of the GBs with a desirable structure and sometimes enriched with elements improving material integrity. One of the known examples of GB engineering is microalloying with GB-active elements like B. The effect of B on mechanical properties of steels [24,25], Cu [26], Al [27], Ti [28], intermetallics [29,30] and NBSs [31,32] has been investigated and related to its GB segregation. The segregation of the B on GBs is reported as the main factor improving the ductility of the material. First-principal studies showed that the B contributes to the cohesion enhancement of the GB [24]. It also has retardation effect on the carbide formation [33,34]. Therefor, its presence shows a great effect on ductility enhancement. However, the B alloying may result in reducing the material's strength. Addition of the elements with the ability of solid solution strengthening could compromise this effect. The addition of Cu, for mechanical purposes, is barely reported for NBSs, but due to its high solubility in Ni, it is likely that it does not serve as strong precipitate former and efficiently contribute to the solid solution strengthening [35].

Most of the studies on the influence of B alloying, were conducted on poly-crystalline alloys and therefore could not provide a detailed knowledge of the actual impact of alloying at the GB-resolved level [36]. B is reported to alter the grain size [36] and also the ratio of especial GBs in the material. Therefore, the obtained mechanical properties of the bulk alloy could not truly represent the exact mechanism of B influence in micro scale. The effect of grain size and GB structure in bulk material can be ruled out by confining the test condition to a small scale bi-crystal sample [37]. By testing in similar environmental condition and GB structure, it would be possible to investigate the mechanical response of a bi-crystal with desired segregated element. For instance, in our previous study the effect of S and H co-segregation in Ni GB was studied by this method [38]. Another advantage of this kind of test is to readily visualize the GB interaction with the dislocations. Although its resolution is not comparable with transmission electron microscopy (TEM), it can be more representative of the material because of its sufficient larger size rather than the confined, small sampling of the TEM investigations [39].

In this work, a possible way to combine theoretical and experimental methods for prediction, characterization and mechanical testing for design of HE-resistance of NBS with GB-controlled properties is proposed. For this purpose, a standard 725 NBS is selected as a first step of the investigation. DFT-based predictive modeling approach, that already been demonstrated to be an effective computational approach to design of NBS[40–43,18], is used to analyze possible changes in GB chemistry and properties in this alloy upon composition variation. Therefore, small scale bi-crystal samples were prepared, each containing an individual GB for micro-cantilever bending tests to investigate the efficiency of the suggested GB engineering approach with respect to alloy resistance to H assisted intergranular cracking. The results of this investigations allowed us to take a deeper look into material behavior at and near GB at multiple scales and to contribute to design of new NBSs. The produced alloys demonstrated improved HE-resistance compared to the standard 725 alloy that could be predicted and controlled by means of the presented GB engineering approach. A micro-scale investigation of the crack initiation at GB allowed us to analyze and identify mechanisms of intergranular cracking in all considered alloys under H loading conditions.

2. Method

2.1. Materials and characterization

2.1.1. Material

The API heat treated Alloy 725 was used in this study as a base material, naming modification A (Mod A). The main alloying elements of the material were 19.7 wt% Cr, 10.1 wt% Fe, 7.3 wt% Mo, 3.6 wt% Nb, 1.4 wt% Ti and lower than 0.01 wt% C. The heat treatment consisted of prior solution annealing at 1038^{circ}C for two hours followed by water quenching and then heating up to 732^{circ}C for 8 h, cooling in furnace down to 621^{circ}C and keeping it in this temperature for 8 h [44]. Two samples with minor alloying modifications were produced by adding B (Mod B) and B+Cu (Mod C). The B addition for Mod B was in the range of 250–350 ppm. For Mod C the level of B content was lower than 100 ppm while about 2.3 wt% Cu was added to the alloy. The grain size of the produced alloys together with the information about the coverage of the specific GBs are listed in Table 1.

All samples were cut in cylindrical form with the diameter of 8 mm in order to be used for electron backscatter diffraction (EBSD) studies and subsequent focused ion beam (FIB) milling. the samples were ground up to #2000 grit paper and finally electropolished by a solution of 1 Molar methanolic H_2SO_4.

2.1.2. Atom probe tomography

For the investigation of local chemical composition at the GBs, atom probe tomography (APT) with site-specific sample preparation was conducted. The preparation was realized with FIB milling on a FEI Versa 3D Dualbeam workstation, equipped with a EDAX Hikari XP EBSD camera system for transmission Kikuchi diffraction (TKD) analysis. In all three alloys, GBs with misorientations between 38 and 48° and grain orientations similar to (1 1 1) and (1 0 1) were chosen from EBSD pattern for positioning of the lamella in lift-out process. For coarse milling of the pyramidal shape of the APT tip, acceleration voltage of 30 kV and ion currents between 100 pA and 3 nA were applied. To reduce ion damage the annular fine milling steps were performed with 8 kV and 12 pA. For positioning of the GB in the vicinity of the first 100 nm of the finished tip, TKD was completed in analytical mode with 20 kV voltage and a current of 8 nA. Further details of the lift-out procedure can be found in [45]. The interfacial excess value (IFE), which will be used in Fig. 5, is calculated according to the following references [46,47].

2.2. H content and diffusion

The H content of the samples was measured by thermal desorption spectroscopy (TDS) technique. Samples with the dimensions of 10 × 5 × 0.5 mm were used for H cathodic charging. A mixture of Phosphoric acid-Glycerol (1:2 v/v) served as an electrolyte. The samples were potentiostatically charged at − 1050 mV vs. Ag/AgCl reference electrode at the temperature of 75^{circ}C. G4 Phoenix DH, Bruker Co. coupled with mass spectrometer were utilized for the TDS measurements. The total H content was analyzed by instantaneously exposing the sample at 800^{circ}C for 600 s. In addition, the ramping test was conducted by gradually increasing the temperature from 30 to 800^{circ}C with the heating rate of 0.5k/s. To have an estimation of the H penetration profile into the material the COMSOL multi-physics software version 5.5 was used. The second Fick's law was solved for the 1D line at room temperature with charging from one side, considering the insulating condition for the opposite side.

2.3. Bi-crystal micro-cantilever preparation and testing

Bi-crystal micro-cantilevers were milled by FEI Helios DualBeam™ FIB system. The micro-cantilevers contained a selective random GBs with the misorientation angle in the range of $30–45^{circ}$ as listed in Table 2. Although there are results showing that the low orientation GBs could act as crack nucleation sites, the intergranular crack usually

Table 1
Grain size and GB types of the three Mods used in this study.

ID	Grain size (μm)	%Σ3	%Σ5	%Σ9
Mod A	138.9 ± 9.0	42.7	0.6	1.3
Mod B	132.8 ± 6.6	45	0.8	0.8
Mod C	163.6 ± 4.6	60	0.3	0.7

Table 2
Measured GB misorientation angle and corresponding adjacent grains information in Mod A, Mod B and Mod C bi-crystal beams.

ID	Misorientation angle (^{circ})	Axis			Sigma	Plane 1 (fixed grain)			Plane 2 (free-standing grain)		
		h	*k*	*l*		*u*	*v*	*w*	*u*	*v*	*w*
Mod A	44.7	1	− 6	− 10	–	7	− 9	21	25	10	− 12
Mod B	31.3	− 5	6	6	–	6	− 28	− 7	− 6	11	1
Mod C	43.7	− 2	0	3	47b	1	15	− 4	− 1	1	− 1

propagates within the high angle GBs (HAGBs) [20,48]. The HAGBs are considered as one of the weak parts of the engineering materials especially when there is a risk of GB segregation [49]. The arrows in Fig. 1 show the subjected GBs in EBSD pattern of the three modes. A representative picture of a milled cantilever and its geometry is shown in Fig. 2. The selected GB angle versus beam surface is also represented in Fig. 2(a_1) – (a_3).

The GBs were selected in a way to have an angle close to 90^{circ} vs. the cantilevers surface. Therefore, if the load on the beam top surface considered as a pure tensile load, the GB would be perpendicular to the load direction and hence upholds the maximum stress. A shallow U-shaped notch with the diameter of ~ 300 nm is milled on the GB path to intensify the stress concentration on the GB.

Micro-cantilevers were bent in two conditions of H-free (air-bent) and in situ electrochemical H-charging. The bending test was carried out with the Hysitron TI 950 Tribo-Indenter® system in an integrated, home-made conventional three electrode cell as described elsewhere [18,50]. The electrolyte for H-charging was similar to the one used for TDS sample charging. The potential was set at − 1500 vs. $Hg/HgSO_4$ (−1050 vs. Ag/AgCl) and the specimen was charged at room temperature. The cantilevers were charged under cathodic potential minimum for two hours before starting the test and the potential kept constant during the bending process. At least two cantilevers for each condition were tested to ensure about the reproducibility of the results. The bending tests were carried out under the displacement control mode with the displacement rate of 2 nm/s. The long shaft of conical tip with the radius of 0.5μm were used for cantilever bending.

Post-deformation analysis of the cantilevers were carried out using high resolution scanning electron microscope (SEM) and TKD. The cantilevers were gently transferred with the lift-out finger facility of the FIB and then placed on a three-post copper grid. The cross-section of the cantilevers were milled from both sides to reach approximately 100 nm of thickness. This thickness is low enough to enable electrons to pass through the material. By detecting the passed electrons, the TKD would be possible. This form of EBSD improves the spatial resolution of the patterns by narrowing the energy width of the scattered electrons [51]. As a result, indexing of the nano-meter lattice distortions of the plastic area would be possible [52]. In this study the step size of the electron scanning for TKD was fixed at 10 nm.

2.4. Computational details

First principles calculations were performed at 0 K with the projector-augmented wave (PAW) [53,54] method as employed in the Vienna ab initio simulation package (VASP) [55,56]. For the exchange-correlation potential, the Perdew-Burke-Ernzerhof (PBE) [57] implementation of generalized gradient approximation (GGA) was used. The plane-wave basis set cutoff energy was set to 400 eV. The

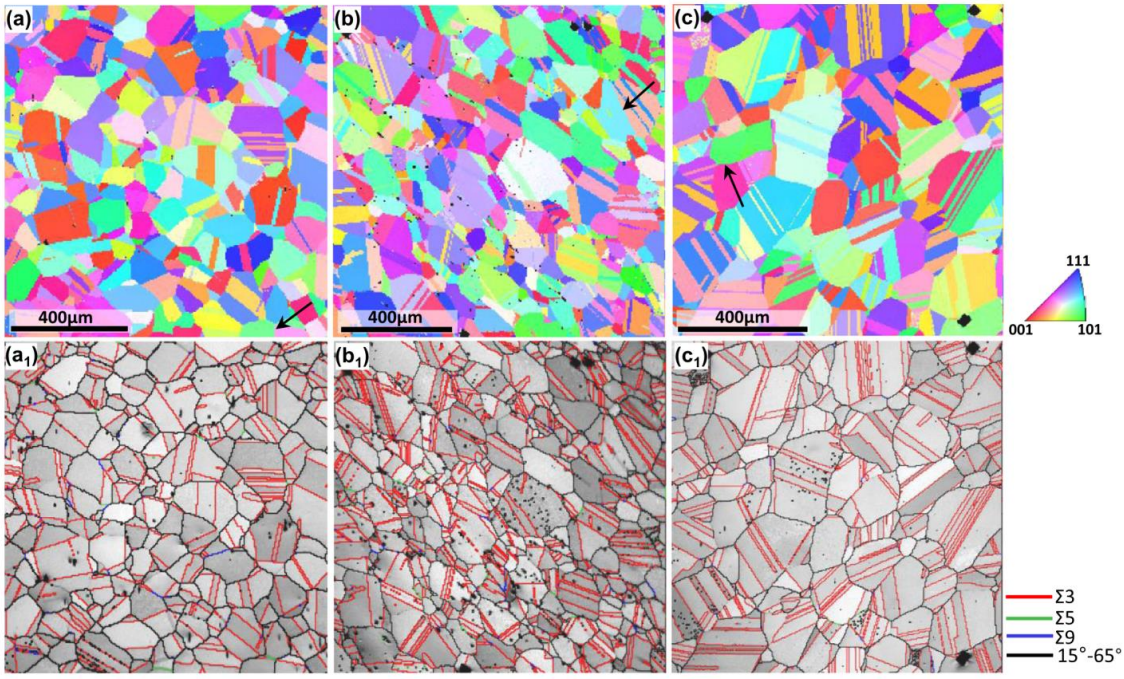

Fig. 1. Inverse pole figure map of the studied Ni super alloys Mod A (a), Mod B (b) and Mod C (c). The image quality maps of the same area show the distribution of the especial GBs in three materials (a_1 to c_1).

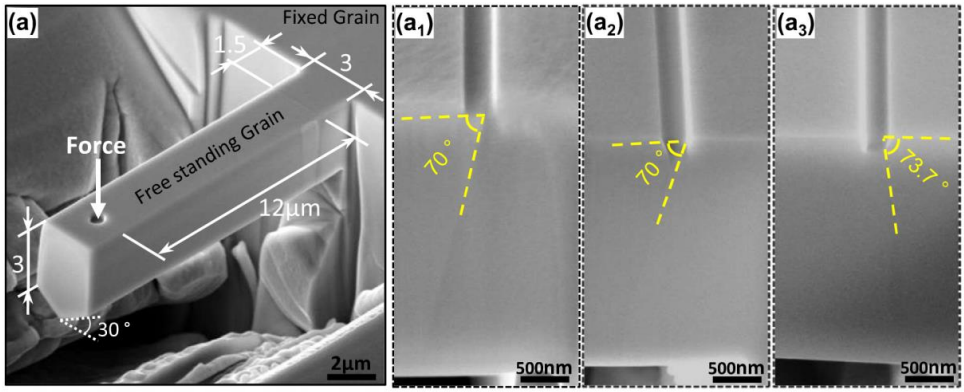

Fig. 2. A representative scanning electron microscopy image and the geometrical dimensions of the milled cantilevers (a). The angle between the selected grain boundary and beam surface in Mod A (a_1), Mod B (a_2) and Mod C (a_3).

convergence criteria of self-consistent calculations was set to 10^{-5} eV/cell for the total energy and to 9×10^{-3} eV/Å for the atomic forces. The integration over the Brillouin zone was done using the $4 \times 4 \times 1$ Monkhorst-Pack *k*-mesh [58] for the GB cell and using the $4 \times 4 \times 4k$-mesh in the $3 \times 3 \times 3$ (conventional face-centered cubic (FCC) cell consisting of 108 atoms) bulk supercell calculations. The lattice parameter was fixed to 3.515 Å [59] and only the ions were allowed to relax in the calculations. The Ni Σ5(012) coincidence site lattice (CSL) symmetric tilt GBs was modeled using a 76-atom GB slab with 19 layers and 4 atoms/layer [59]. The Ni Σ5(012) GB structure used in this work is illustrated in Fig. 3. The calculated GB energy is 1.29 J/m^2 and the corresponding work of separation is 3.51 J/m^2.

Segregation energies are computed as

$$E^{i,j}_{seg} = (E^{i,j}_{slab} - E_{slab}) - (E^{j}_{bulk} - E_{bulk}) + \delta E_{bulk}/\mathrm{N}, \quad (1)$$

where $E^{i,j}_{slab}$ and E_{slab} denote the total energy of the GB slab with and without a solute *j* at site *i*, respectively, and similar, E^{j}_{bulk} and E_{bulk} refer to the bulk cell with and without solute *j*. The number of atoms in the pure bulk cell is denoted by *N* and δ changes depending on the site type. For the case where a solute segregates from the one type of site (interstitial or substitutional) in the bulk to same type of site at the GB, $\delta = 0$, for the case that the solute is interstitial in the bulk and substitutional at the GB, $\delta = 1$, and in case the solute is substitutional in the bulk and

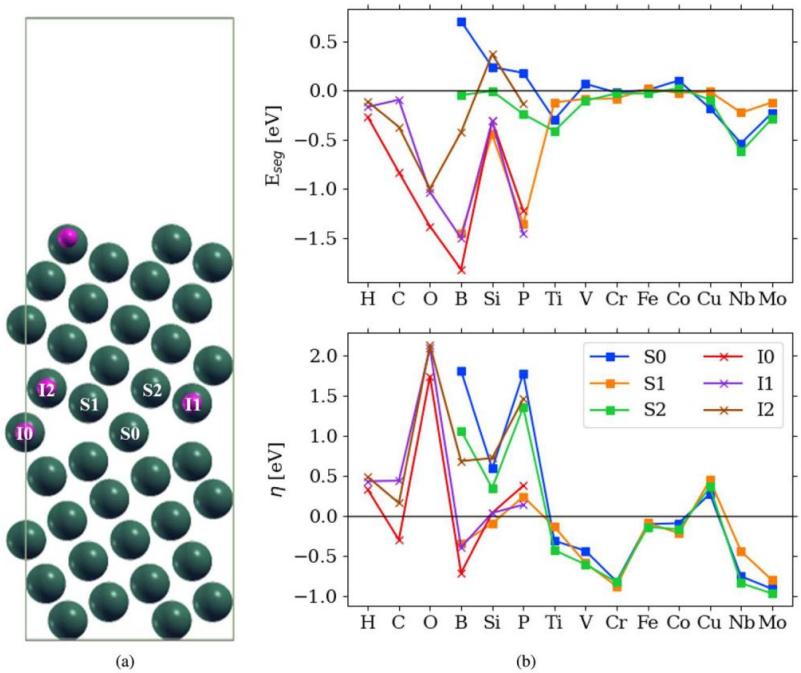

Fig. 3. a) Σ5[100](012) GB where the studied interstitial (I0-I2) and substitutional sites (S0-S2) are labelled and b) segregation energies to the Σ5[100](012) GB at interstitial (I0-I2) and substitutional sites (S0-S2) as well as the corresponding strengthening energies (η).

interstitial at the GB, $\delta = -1$. In this definition, solute enrichment is preferential for negative values of the segregation energy and solute depletion for positive values. The strengthening energies are obtained from the difference in GB and surface segregation according to the Rice-Wang theory [60]:

$$\eta^{i,j} = E^{i,j}_{seg,GB} - E_{seg,FS}, \tag{2}$$

with $E^{i,j}_{seg,GB}$ the segregation energy of solute j to site i at the GB and $E_{seg,FS}$ the segregation energy to the surface.

The concentration of solutes at the GB can be obtained from the multi-site McLean isotherm derived by White et al. [61,62]. It connects the bulk content C^j_{Bulk} and the segregation energies $E^{i,j}_{seg}$ to sites i of the solutes j with the GB concentration as a function of temperature:

$$C^{i,j}_{GB} = \frac{C^j_{Bulk}\exp\left(-\beta E^{i,j}_{seg}\right)}{1 - \sum_k C^k_{Bulk}\left(1 - \exp\left(-\beta E^{i,k}_{seg}\right)\right)} \tag{3}$$

The temperature comes into play together with the Boltzmann constant via the thermodynamic Beta, $\beta = (k_B T)^{-1}$. The total content of a solute at the GB is given by averaging over all GB sites n:

$$C^j_{GB} = \sum_i C^{i,j}_{GB}/\mathrm{n}. \tag{4}$$

The IFE value in atoms/nm^2 that is extracted from APT measurements is also related to the GB concentration as [63]:

$$C^j_{GB} = \mathrm{IFE}^j \times A + C^j_{Bulk}, \tag{5}$$

where A denotes the GB area. The concentration of the solutes at the GB can be combined with the strengthening energies to obtain the effect of solute concentrations on GB cohesion [63,64]:

$$\Delta E^j_{coh} = \sum_i C^{i,j}_{GB}\eta^{i,j}/\mathrm{A}. \tag{6}$$

3. Results

3.1. APT results

The distribution of the alloyed elements B and Cu and the matrix species Ni of the selected GBs is visualized in Fig. 4 for Mods A, B and C. All GBs have misorientation angles as close as possible to the GBs used in the calculations and in the micro-cantilever bending experiments. The quantitative information of the GB composition was obtained by comparing chemical compositions in the parts of the APT tip dedicated to the GB and bulk region. Therefore, we assigned a cuboidal region of interest (ROI) of 5 nm thickness (as displayed in Fig. 4 d), which was positioned in the GB plane. For the tip concentration all elements outside this ROI were summed up, and vice versa the inside region was used for the GB concentration. The obtained results are summarized in Fig. 5.

The first observation one can make, after a visual comparison of the tips in Fig. 4, is a strong depletion of the Ni, the main matrix element, in Mod B and C and virtually no pronounced Ni content changes across the GB plane in Mod A. This observation can be used as an indication of more pronounced segregation of elements substituting Ni at the GB in Mods B and C compared to Mod A. Indeed, if we take a closer look at another element B, we see a significant segregation of it to the GB in Mod B and C and only a not so well pronounced cloud of B atoms around the GB in Mod A.

The distribution of B is highly localized at all observed GBs (see Fig. 4 and Fig. 5). Our results show that ~ 0.11 at% is presented in the bulk of the tip of Mod B and ~ 2.91 at% B is located at the GB. In Mod C, the concentration of the B is similar to Mod B. Although the tip content of B for Mod B and C are almost the same, the amount of measured B for Mod C is about ~ 0.5 at% higher than Mod B. Cu in Mod C it virtually equally distributed in the bulk region and a weak depletion at the GB is visually observable.

The IFE values in Fig. 5, which provide a statement of segregation (positive) or depletion (negative) behavior, confirm the information gained by the comparison of tip and GB concentration. B with a positive IFE for all modifications shows a higher GB concentration than tip concentration, and vice versa for Cu.

3.2. TDS results

Due to the different chemical composition and microstructure of Mods A, B and C, it is necessary to know, relatively, how much H each Mod could absorb. The H content is a major factor affecting the brittleness of the material. Therefore, the TDS was carried out and the result are depicted in Fig. 6. The results show that the highest amount of H of 7.49 wppm has been absorbed in Mod C followed by 6.86 wppm in Mod A and 4.87 wppm in Mod B.

Mod C possesses the highest amount of H among others which can be rationalized by knowing that the special GBs are the preferential areas for the H segregation [65,66]. This Mod has 61% special GBs (Table. 1) which is about 20% higher than the other two Mods. Another factor which can affect the H solubility of the Mod C is the lattice distortion caused by substitutional copper alloying. Due to the higher atomic radius, replacement of the matrix atoms with Cu will result in lattice distortion. The elastic distortion is reported to be a possible trap for H atoms [67].

Since the percentage of the special GBs in Mods A and B are almost similar to each other there should be another factor affecting the sig-

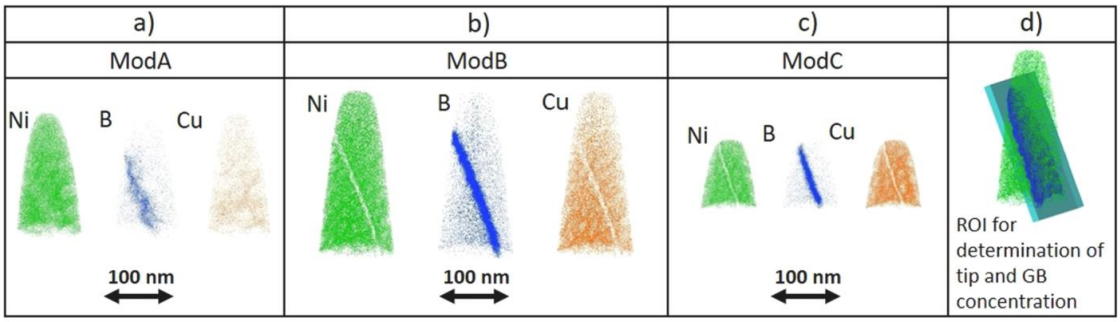

Fig. 4. APT reconstruction for one exemplary tip of each modification for a) Mod A, b) Mod B and c) Mod C. The main important elements Ni, B and Cu are illustrated. In d) an exemplary tip of Mod B with Ni(green) and B (dark blue area) atoms is depicted with the light-blue cuboidal region of interest (ROI), which was used for the calculation of chemical content of the alloyed elements in Fig. 5.

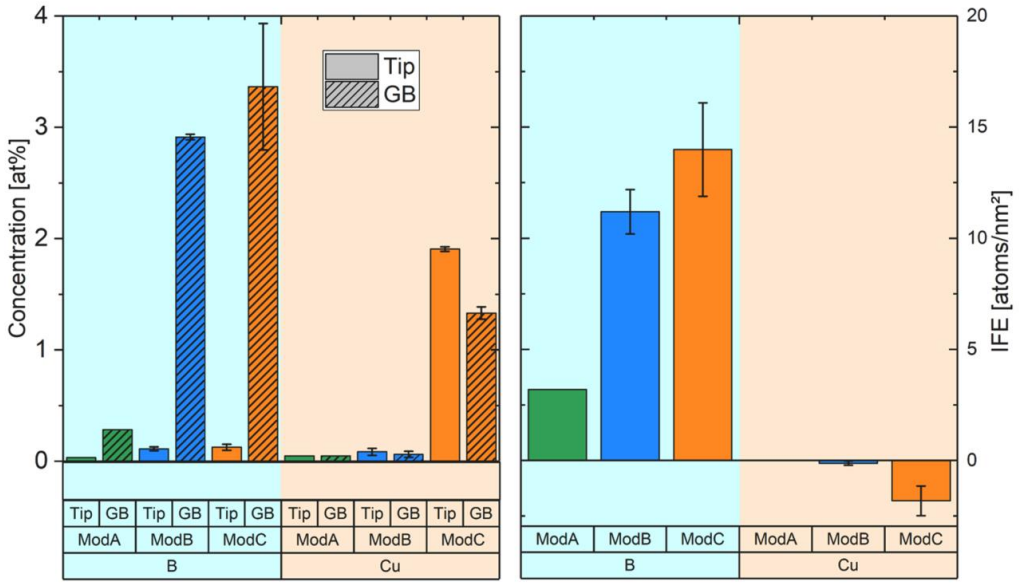

Fig. 5. Chemical content of the alloyed elements in the tips and at the GB (measured via APT) and according IFE values for all three modifications.

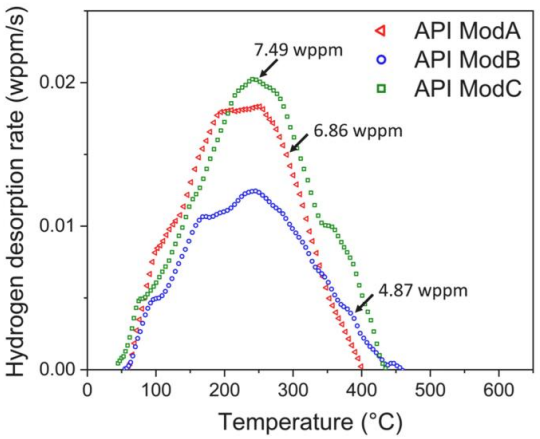

Fig. 6. Hydrogen desorption spectra of three Mods obtained from TDS measurement.

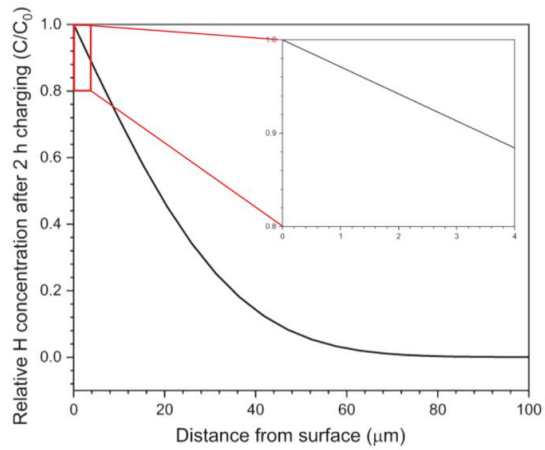

Fig. 7. The diffusion profile of the Hydrogen in Nickel superalloy based on the Fick's second law.

nificant low amount of H in Mod B compared to Mod A. As mentioned before, the addition of B and Cu has no effect on the γ' and γ'' structure in the matrix [35,68]. Therefore, assuming the same H absorbent ability of the matrix, the HAGBs can be considered as an influential factor. It is reported that the presence of the B accumulated at the HAGBs could repel the H atoms to accommodate at the GB [69,70].

The penetration depth of H during the electrochemical charging has been evaluated using the Fick's second law implementing the H diffusion coefficient primarily measured in Alloy 718 [71]. The result for 2 h charging at room temperature is shown in Fig. 7. As one can see, the highest H concentration is reached near the sample surface and drops exponentially as the distance from the surface increases. However, H concentration reaches 90% of its surface value within the depth of the first 3μm from the surface, meaning that the tested cantilevers have been almost completely saturated with H after 2 h of charging.

3.3. DFT results

The $\Sigma5[100](012)$ GB is a symmetric tilt GB with a misorientation angle of 53.13° around the [100] axis and has been selected as a representative case for a high-angle GB in Ni [59,72]. The DFT results on the segregation energy profiles and on the corresponding changes of the work of separation (strengthening energy η) are plotted in the top and bottom panels of Fig. 3.b, respectively. The strongest segregation tendency that corresponds to the lowest values of E_{seg} is observed for B, P and O solutes occupying interstitial positions at the GB. Weaker segregation tendencies are observed for other interstitial elements like C and H and for most of the substitutional solutes, with Nb, Ti and Mo atoms

having the most pronounced propensity for segregation. Here, we would like to note that E_{seg} values only indicate a segregation tendency of a solute at thermal equilibrium conditions and do not always correlate to the actual elemental GB content, that may strongly depend on a site competition between elements in a multi-component alloy, chemical composition of the matrix phase, grain size and multiple kinetic effects related to the heat treatment history of a material under investigation.

In the bottom of Fig. 3 (b) we show a possible effect of all considered solutes on the change in the work of the GB separation or the GB strengthening energy η. Positive values of η indicate an increase of the GB work of separation and of the GB cohesion respectively; negative values indicate the opposite effect of GB decohesion. The results indicate that Mo, Cr, Nb, and B are among the strongest GB cohesion enhancing elements, whereas H, O, and P exhibit a very distinct negative effect on the GB cohesion. Other elements like Si and C can have a mixed strengthening or destrengthening effect on the GB depending on the GB site occupation. Ti, V, Fe and Co have less pronounced effect than Mo, Nb and B on GB strengthening and Cu shows some tendency towards GB decohesion, provided that the elements be present at the interface.

The calculated results are in agreement with available literature data, although previous works often neglected the multi-site nature of a GB and only focused on the central GB site (i.e. S0 and I0 in Fig.3), see [40,73]. Although in most cases the strongest segregation energy is found for the central GB site, there are exceptions to this rule, e.g. P at site I1 or Cr at site S1.

3.4. Computational analysis of GB composition and cohesive strength

The effect of solutes on the GB cohesion in an alloy is a combination of the strengthening potency of its components, i.e. the strengthening energies shown in Fig. 3.b, and the amount of solutes present at the GB (Fig. 4 and Fig. 6), see e.g. Refs. [63,74]. As mentioned above, the E_{seg} values shown in Fig. 3.b only indicate a segregation tendency of a solute at thermal equilibrium conditions and do not always correlate to the actual elemental GB content. The latter can be rather accurately described within modified McLean segregation isotherm that takes into account site competition between segregating elements, grain size and kinetic effects related to the heat treatment history as described in Sec. 2.4 and in Ref. [43] in detail. Here, we use experimental data on GB segregation from APT (Fig. 4) and TDS (Fig. 7), as well as modeled data based on DFT segregation energies. This is combined with the data on the GB strengthening (η) (Fig. 3) to evaluate the effect of each segregating element on the GB cohesive strength using Eq-s. 5 and 6.

The resulting changes in the GB cohesion for Mod A, B, and C alloy modifications are shown in Fig. 8 (a) and (b), which use modeled GB contents and experimentally measured GB contents, respectively. The results show that B has a pronounced effect on the GB cohesive strength increase in Mod B and C compared to Mod A. The trend in the increase is the same for using modeled data (Fig 8 (a)) or experimental data (Fig 8 (b)) on GB content, but the magnitude changes significantly. The reason for this difference is that the GB content predicted based on segregation energies is significantly higher than the experimentally measured values. This could be a result of neglected interaction of solutes at the GB, which come into play at high solute concentrations. The effect of Cu is negligible in both cases. Based on the segregation energies, only a marginal GB enrichment is predicted for Mod C, which results in a minor decrease in GB cohesion, whereas experimentally, for no modification an enrichment of Cu is observed.

To evaluate the effect of H on GB cohesion, we consider the measured H content from TDS of 4.87–7.45 wppm in the bulk. This leads to significant H enrichment in the GB and subsequently to a substantial decrease in GB cohesion in all alloys as shown in Fig. 8, where the results were calculated according to H charging at 75°C. In Fig. 8(c), the enrichment and effect on cohesion of H is plotted as function of the bulk content and the segregation energies according to Eqs. 4-6. The top panel shows the enrichment and the bottom panel displays the resulting effect on GB cohesion. Of course, with increasing bulk content, the GB content increases, and with increasing GB content, the GB cohesion decreases. The measured H contents in the modifications are highlighted as well. How these H contents affect the cohesion together with B and Cu is shown in Fig. 8 (a) and (b). As the content of H is rather similar, i.e. in the same order of magnitude, in all three modifications, the effect on cohesion is also not very different. As such, The original effect of chemical composition is still the same as without H except for a constant shift. This constant shift with H leads to a GB cohesion below that of the pristine GB in case of the experimentally observed GB content.

3.5. Bi-Crystal cantilever bending

Representative load-displacement (L-D) curves from bi-crystal cantilever bending tests for Mods A, B and C in H-free and H-charged conditions are shown in Fig. 9. The position of the notch has been chosen

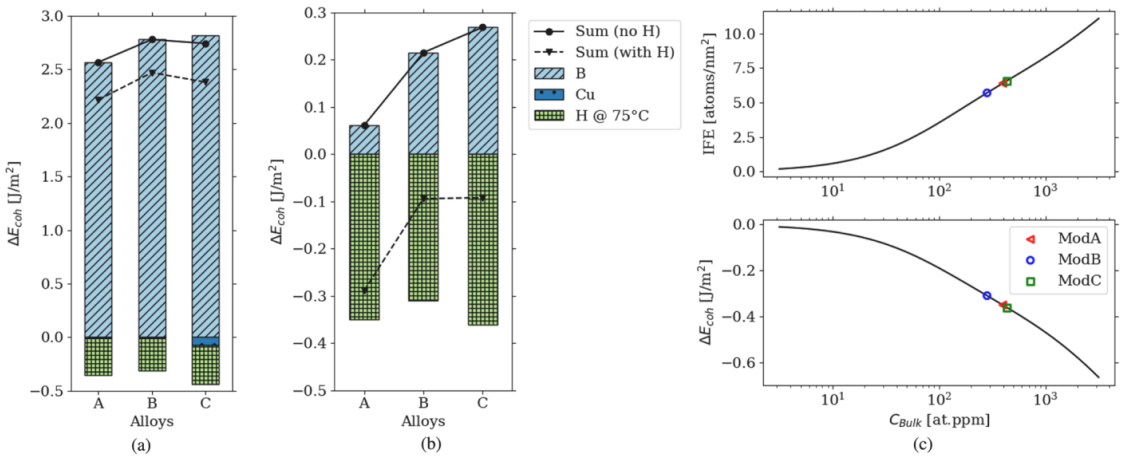

Fig. 8. Changes in GB cohesion energy for the studied modifications due to solute enrichment a) calculated from APT bulk values and b) obtained from APT IFE values which are linked to ab initio strengthening energies. The H enrichment at 75° is computed individually from the segregation energies for both a) and b). c) GB enrichment of H at GB as a function of H bulk content with corresponding GB embrittlement and marked bulk concentrations (see text and Fig. 6).

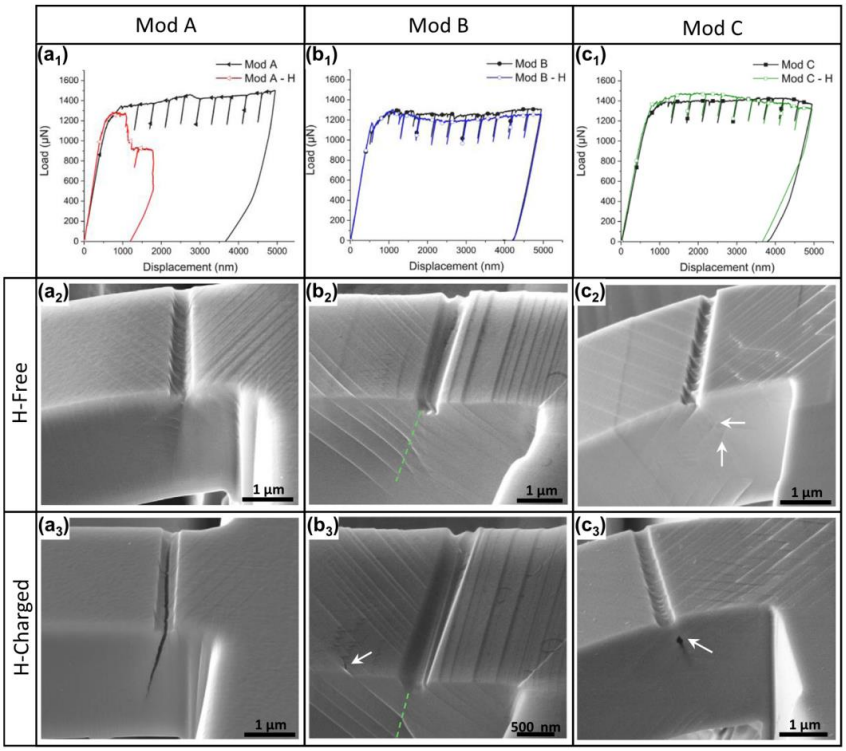

Fig. 9. The load-displacement curves of the air and H-bent cantilevers of Mod A, B and C with its corresponding post-deformation secondary electron images from the side view of the bi-crystal beams.

to be on top of the edge of the GB plane going throughout the cross-section of the microcantilever beam. The GB misorientation angles have been selected to be as close as possible to the GBs studied in DFT and APT in the previous sections. The curves show the load evolution with displacement of the indenter tip placed on the cantilever.

The L-D curve of Mod A bent in air shows a continuous increasing load, up to 1500μ N. During H-charging, an abrupt drop is observed already after 1μm displacement at the very initial stage of the plastic deformation zone of the L-D curve (Fig. 9(a_1)). This behavior can be attributed to the crack formation and propagation as can be seen in Fig. 9(a_3). Crack formation reduces the cross-sectional area of the beam which is compensated by a load drop in L-D curve necessary to maintain the constant displacement of the indenter. The formed crack in H charged condition propagated via the GB path.

As shown in Fig. 9(a_2), bending Mod A beam in H-free condition resulted in activation of dislocation slip bands (DSBs) which stop at the GB. The dislocations reached to the surface revealed by a step mark on the surface which are parallel to each other and oriented along the preferential dislocation slip planes in each grain. Two activated slip planes can be seen in Fig. 9(a_2) on the surfaces of both grains of the bi-crystal. The observed activated slip systems in each side of the bi-crystal (denoted as fixed (rightmost in Fig. 9(a_2)) and free (leftmost in Fig. 9 (a_2))) are listed in Table 3.

The sharp DSBs and the distinct surface steps are results of the slip planarity. There are two main reasons for the slip planarity in NBSs: (I) firstly, containing the high amount of solid solution elements reducing the stacking fault energy (SFE) of these alloys which enhances the slip planarity by impeding dislocations's cross slip [75]. (II) secondly, the presence of the γ'' and γ' precipitates in Alloy 725 which are finely dispersed in the γ matrix, considered as a coherent or semi-coherent particles. Shearing of these precipitates during deformation and limiting the cross-slip movement are assumed as a reason for the slip planarity [76]. Adding H into the system, on the other hand, can reduce the work of separation especially in GBs which is well-explained by the HEDE mechanism [11]. Once the H is added to the system it can accumulate in GBs as trapping sites resulting in reducing the work of separation. Therefore, the intersections of DSBs with the GBs can be a favorable site for nano-voids formation which later can link to each other leading to crack initiation and propagation.

Table 3
The activated slip systems and the Schmid factors in Mod A, B and C bi-crystal beams.

Grain ID	Slip system		Schmid Factor
	(*hkl*)	[*uvw*]	
Mod A (fixed)	(11–1)	[101]	0.46
Mod A (free)	(1–1–1)	[110]	0.44
	(111)	[10–1]	0.40
Mod B(fixed)	(111)	[1–10]	0.46
Mod B(free)	(1–11)	[011]	0.50
Mod C (fixed)	(1–11)	[110]	0.49
	(11–1)	[1–10]	0.47
Mod C (free)	(1–1–1)	[1]	0.34
	(1–1–1)	[101]	0.34

Regarding Mod B cantilevers (Fig. 9(b_1)), the maximum load in the uncharged condition levels off in a load range of about 1200μn which is 200μm, about 14%, lower than the corresponding load in Mod A. In contrast to Mod A, cantilevers of Mod B bent in both H-free and H-charged conditions show similar L-D curves except a slight lower load of

the H-bent compared to the air-bent counterpart (Fig. 9(b_2) and (b_3)). This lower load level in presence of H can be attributed to the nano-crack formation at the DSBs in the free-standing grain of the cantilever as depicted by arrow in Fig. 9(b_3). Furthermore, in post deformation micrographs of the air bent cantilever for Mod B (Fig. 9(b_2)), contrary to the Mod A and C (Fig. 9(a_2), (c_2)), the GB path can be barely distinguished showing that no stress concentration is formed at the GB path. The GB is denoted with the green dashed line in Fig. 9(b_2), (b_3). Shortly it can be said that the dislocations in Mod B could be transferred via the GB to the adjacent grain or annihilated in the GB. Therefore, no localized stress could be concentrated at the GB from the SEM graphs. This issue will be discussed later in this paper.

As can be seen in Fig. 9(b_3), nano-cracks during H-charging were formed not at the GB but at DSBs away from it. The figure shows a crack that has already formed at one set of DSB and deviates from its original plane, goes into the neighboring DSB as depicted by arrow in Fig. 9(b_3). There are several studies that have proved that the DSBs can serve as nucleation sites for nano-voids or -cracks [66,77,78]. H can further amplify the slip planarity by either decreasing the SFE or increasing the dragging force on dislocations movement [79]. Therefore, the density of dislocations that reach to the surface by one DSB will intensify and could be an appropriate place for crack initiation.

The maximum load of Mod C in both charged and uncharged conditions are similar to that of Mod A, i.e. 1400μn (Fig. 9(c_1)). In the air-bent condition, the maximum load remains constant during bending, while the load shows a primary hardening followed by a continuous softening with a modest decrease in the load values during H-charging. The SEM pictures of bent cantilevers of Mod C show nano-void formation near the GB intersection without H-charging as depicted by arrows in Fig. 9(c_2) and formation of larger voids directly at the GB route during H-charging (Fig. 9(c_3)).

4. Discussion

The acquired results will be discussed in two main sections. The first one deals with the micro-alloying effect on the mechanical properties of the alloy in three Mods without H and the second part will discuss the HE of the alloys.

4.1. Strength response to micro alloying

4.1.1. Modification A: GB hardening

Micro-cantilever experiment on bi-crystals provides a unique opportunity to investigate mechanical properties of a material on the microstructure-resolved level with a specific focus on isolated GBs. Bi-crystal micro-cantilever testing, on the other side, can provide deep insight into the dislocation-GB interaction by confining the test geometry to a selected GB and the adjacent grains. Different mechanisms have been put forward to describe the dislocation-GB interaction [80,81]. The GB here in Mod A bent in air, acts as an obstacle to dislocation motion. The dislocations in both fixed and free-standing grains are stopped at the GB path. The high stress accumulated in the GB region leads to bulging of the GB as depicted in Fig. 10(a_1). This figure shows a side-view of the central part of the cantilever after slicing by FIB. The high amount of dislocation pile-ups at the GB creates backstresses which in turn lead to activation of other dislocation sources around the GB contributing to formation of an extended plastic area [82]. It shouold be noted that the white arrows in Fig. 10 represent the precipitates which were found frequently in Mod B and scarcely in Mod A, while no precipitates were formed in Mod C. These precipitates were shown to be rich of Nb, Ti and Mo, as depicted in EDS analysis in supplementary data. The results showed no sign of crack initiation or propagation around these precipitates.

Quantitative representation of the lattice distortion around the GB due to the plasticity can be obtained by the Kernel average misorientation (KAM) map derived from the TKD results. This map shows the lattice distortion of each single point relative to the selected neighboring points in the scanned area. Fig. 11(a) shows the KAM map of the same area as Fig. 10(a_1) considering the lattice misorientation of the points relative to the fifth neighboring points.The extremely high amount of distortion at the GB and also in some DSBs prevent the software to index the kikuchi pattern in that black-colored areas, denoting a high amount of accumulated strain formed due to the dislocation pile-up.

Dislocation pile-up formed on both sides of the GB, leads to continuous hardening and an increase of the load in the L-D curve shown in Fig. 9(a_1). Another sign of the dislocation pile-up formation is the reduction of the serrations in the L-D curve [81], which we observed in the case of Mod A as shown in Fig. 12. This figure is a zoomed view of the Fig.9 with the displacement resolution in the range of 3400–3700 nm.

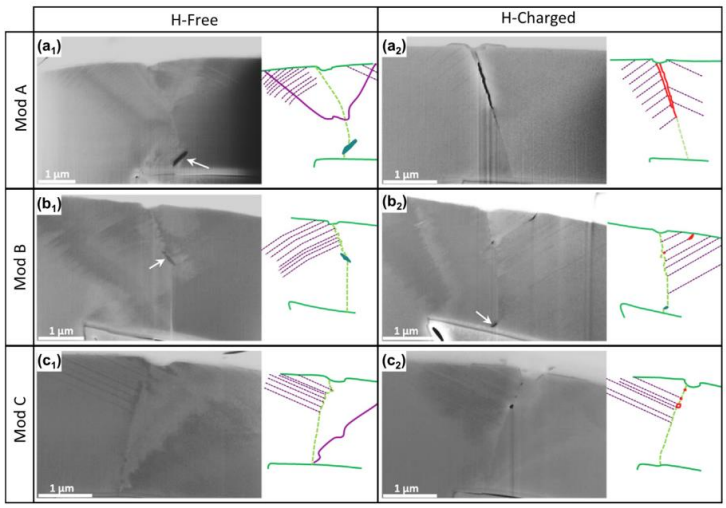

Fig. 10. Cross-sectional images of the middle part of the bent cantilevers after slicing by FIB in H-free and H-charged conditions of Mod A, B and C. Schematic illustration of the grain boundary- dislocations interaction and formed slip bands are shown beside each micor-graph.

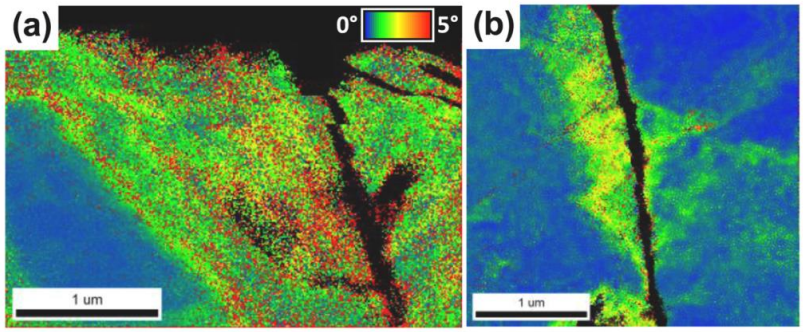

Fig. 11. Kernel average misorientation map of the same area as Figs. 10(a_1)(a) and 10(a_2)(b), obtained from transmission kikuchi pattern considering the lattice misorientation relative to the fifth neighboring points.

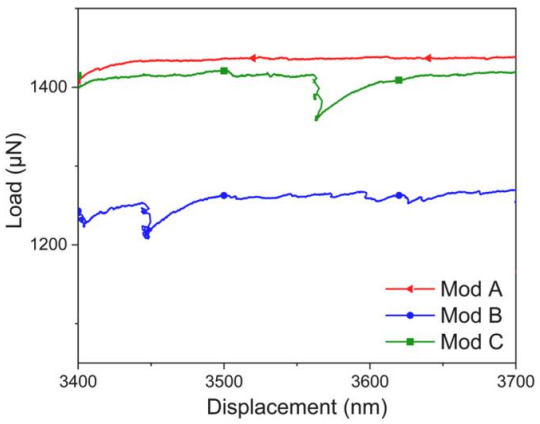

Fig. 12. Magnified view of the load-displacement curves of the Fig. 9 for Mod A, B and C bi-crystal beams bent in air.

As can be seen, the curve for Mods B and C show some load drops which is known as serrated flow or strain burst, while in Mod A the curve is a continuous line without any significant serration.

Different physical phenomena have been reported to cause serrated flow in mechanical testing [83], but mostly, and in particular for the case of a bi-crystal testing the interaction of GB-dislocation is more dominant. Ng and Ngan [84] reported such behavior in a micro-pillar compression test with a GB. By comparing single- and bi-crystal pillars they observed a significant reduction of large strain bursts in stress-strain curves of bi-crystal pillars. This serration reduction has been accompanied by a continuous increase in the magnitude of stress. They attributed this behavior to the high density of dislocations resulting from the presence of the GB in the sample. This result is consistent with the results of our micro-cantilever experiments done in air on the Mod A bi-crystals. However, the authors of Ref. [84] could not observe any dislocation pile-up in a conducted TEM investigation of the compressed nano-pillars. The results of TKD mapping of Mod A suggest the opposite. This discrepancy can be related to the possible dissolution of the piled-up dislocations during the TEM sample preparation [81]. However, in our study the piled-up dislocations and the corresponding large plastic area is captured by slicing of the cantilever and subsequent TKD mapping.

4.1.2. *Modification B: B softening effect*

The cross sectional view of Mod B before H-charging is shown in Fig. 10(b_1). The first difference one can notice, is that the GB shape has changed from a straight line to a serrated one with respect to a similar image of Mod A (Fig. 10(a_1)). We relate this observation to the impingement of dislocations toward the GB plane that let dislocations to glide through it, i.e. the GB plane is not acting as a dislocation barrier anymore as it is in the case of Mod A. In addition, Fig. 9(b_2) clearly shows that the activated DSBs in the free standing grain cut through the GB plane and passed to the fixed grain. However, the passing from the GB makes them deviate from their original direction. The corresponding L-D curves of Mod B (Fig. 9(b_1)) show no hardening compared to Mod A. However, the curve has pronounced serrations as shown in Fig. 12, which are most likely related to the events of dislocations cutting through the GB plane.

Reduction of the strength in NBSs due to alloying with B, as observed in Fig. 9(b_1) has been discussed in a number of papers [85–88]. All these evidences lead us to the conclusion that the B segregation in the GB would result in softening of the alloy. Zhou et al. [88] demonstrated that the B addition to the NBS decreases the tensile strength by softening the GBs. Using TEM observations they claimed that B facilitates the dislocation transmission at the head of the dislocations pile ups which lead to the GB strain dissipation. Lee et al. [29], testing the Ni_3Al Bi-crystal, attributed the B inducing GB softening to its ability to reduce the GB cavities which lead to improving the transfer efficiency of the shear stress concentration. However, the results in literature on the effect of B on GB dislocation transition/generation are controversial. Birnbaum and co-workers [85,86], argued that the influence of B on the GB dislocation transition should not be considered as a separate factor. Indeed, it is the B enhancing cohesive energy, which affects the dislocation mobility via the GB. This idea was doubted by Mills et al. [87], expressing that the small enhancement of the cohesive energy could not have such a large softening effect on their bi-crystal tensile specimens. Albeit, it should be noted that the former group did not reject the possibility of the B contribution in improving the GB efficiency as a dislocation source [86]. Our observations on post-deformation SEM images together with decreased in maximum load and the increased serrated flow in L-D curves by adding B indicates that the B doped GB in the tested beam would pass the dislocations which accumulated behind it or would lead to generation of new dislocations in the neighboring grain. This phenomena would relax the accumulated strain behind the GB. The formation of zig-zag pattern or GB edges represented clearly in cartoon image of Fig. 10(b_1). This kind of edges are normally formed by transferring of a shear stress across the GB, during which the GB is displaced proportionally to the number of transfer events [89].

In addition to the B plasticity enhancement discussed above, most of the researchers attributed the beneficial effect of B to the GB cohesive energy increase which is proved in different systems like Ni-superalloy [32], intermetallics [85,90] and even Ti alloys [91]. Computational

results of this study also clearly shows that B enhances the cohesive energy of the GB (Fig. 3(b). This can be considered as the second beneficial effect of the B presence in the GB. The increase in cohesive energy of the GB, indeed, strengthens the elemental atomic bondings at the GB and has retardation effect on the decohesion (atomic de-bonding) of the GB. To summarize, improved decohesioning strength alongside with the plasticity transfer enhancement, leads to the intergranular cracking retardation in the B-doped GBs. However, the exact relation between the GB cohesive energy and the GB dislocation transmission/generation ability is not yet clearly understood.

4.1.3. Modification C: Solid solution hardening

An increase of the maximum load value in Mod C compared to Mod B that can be seen in Fig. 9 (c_1) is related to alloying with Cu. The APT data shows no evidence of strong Cu segregation at the GB. Considering no sign of any Cu containing precipitation in SEM observations, one can conclude that the micro-alloyed Cu participated in solid solution which is mainly substitutional for this alloy. Therefore, it is reasonable to suggest that the observed strengthening of the material is most likely related to the solid solution strengthening effect of Cu. The primary effect of Cu as a solid solution is to increase the resistance against the dislocation movement due to changes in lattice distortion [35]. Further, decrease in SFE by Cu alloying can be another parameter which results in more difficult cross slipping. It's impact on the SFE decrease lead to have lower number of DSBs revealed on the cantilever surfaces as can be seen in Fig. 9.

Another apparent effect of Cu is the reduction of B solubility in the alloy matrix. Based on APT results (Fig. 5) even though Mod C has lower B content rather than Mod B, more atomic B is segregated at the GBs. However it should be considered that the ratio of HAGBs in Mod C is lower than Mod B. HAGS are the favorable sites for the elemental segregations [92]. In addition, the grains are larger in Mod C, leading to have less GB area and more fraction of B segregation. We could see that bending cantilevers of Mod C in air condition was accompanied by formation of nano voids at some intersections between the GB-DSBs (Fig. 9(c_2)). The increase in the strength of the grain interior in Mod C, compared to Mod A resulted in formation of voids at the GBs rather than inside the grains as it was observed in Mod B.

4.2. Alloys response to hydrogen charging

4.2.1. Modification A

There is a clear difference between the three alloys crack formation and propagation in presence of H. The intergranular fracture happened in Mod A is in line with the previous studies suggesting that the H enhances the intergranular cracking potency [93]. The reduction in GB cohesive energy by H charging, shown in Fig. 8, is the key factor responsible for such an intergranular fracture. This H at the GBs could be provided either by its higher diffusion coefficient compared to the matrix [94] or the amount of H carried by dislocations which are accumulated at the GBs [9]. It should be noted that the formed crack showed a zigzag path. The small deviations of the crack path from the GB and edges produced by the GB-DSBs intersections (Fig. 10(a_2)) indicate that the formed crack is not propagated in fully brittle manner and the propagation is under the control of the plastic deformation ahead of the crack; a similar finding was reached by several authors in H environment [10,95].

4.2.2. Modification B

The addition of B into the GB in Mod B, prevents the intergranular cracking and instead, nano-cracks are formed in DSBs path (Fig. 9(b_2)), in addition to the rarely formed nano-voids at the GB-DSBs, as can be seen in Fig. 10(b_2). As discussed in section 4.1.2, the presence of B enhances the ductility of the alloy by facilitating the GB dislocation transmission/generation. Therefore, the accumulated stress could be released avoiding the GB rupture. However the presence of H diminishes the GB transferability as shown in previous studies on Alloy 718 and 725 [21,96]. H presents in the GBs, calculated by computational methods, increases the energy barrier for slip transmission [97]. Higher resistance of the GB against the dislocation transfer can be observed in Fig. 10(b_2) where the GB is less serrated comparing to H-free condition (Fig. 10(b_1)) which can be an indication that lower amount of dislocations transferred through the GB.

Repulsive effect of B on H is also reported in the literature. The calculations of Wang et al. [30], proved a strong repulsive interactions between B and H when they approach each other. Hence, the segregation of B inhibits the diffusion of H atoms along the GBs. This phenomena is reported by other researchers as well [98,99]. The repulsive behavior of B against H can be an influencing parameter leading to the lower amount of absorbed H obtained by TDS results for Mod B (Fig. 6). The cohesive energy enhancement of the B doped GB also plays a crucial role in preventing the GB decohesion. Therefore the void formation tendency and the crack propagation potency at the GB decrease. All of the above factors contribute to the intergranular cracking resistance of Mod B.

4.2.3. Modification C

The Mod C alloy, was resistant against H while keeping its strength compared to conventional Mod A alloy. The difference between Mod B and C is highlighted as no nano-voids/cracks formation in DSBs in the latter. However, the nano-voids are formed in the GB path with greater size and continuity in comparison with Mod B. Comparison of the cross-sectional view of the cantilevers (Fig. 10(b_2) and (c_2)), shows no clear evidence of GB crossing by dislocations in Mod C tested in H. The GBs in Mod C are favorable sites for void formation since the grain interior possesses more strength compared to Mod B. Therefore, the high stress produced at the GB by dislocation impingement results in nano voids formation at the GB path. The presence of Cu, on the other hand, can increase the GB void formation susceptibility. Based on the DFT results (Fig. 3b), the presence of Cu at the GB diminishes the GB strengthening energy. According to this figure, even though its detrimental effect is not comparable to the elements like P or O, its effect on the GB strengthening energy is almost in the same range as H.

4.3. Summary of the deformation mechanisms in Mods A-C

A summary of the discussion and proposed mechanisms responsible for the observed void/crack formation in three Mods are shown in Fig. 13. Three qualitative energy values at the bottom of the figure are used to represent the mechanical response of the bent beams. In Mod A, by adding H, the GB dislocation transmission/emission energy increases, while the decohesion energy and the lattice dislocation emission energy decrease. Decreasing of the lattice dislocation emission energy is related to the effect of H on reduction of required stress for the onset of plasticity [14,15]. The outcome is the semi-cleavage fracture from the GB path. The crack propagation is controlled by the dislocation-GB intersections in this case lead in to the zigzag pattern of the formed crack. In Mod B, the addition of B significantly increases the GB cohesion. The GB dislocation transmission/emission energy is reduced resulting in formation of serrated GB after bending. In the H-charged condition, nano-voids form at DSBs and rarely within the GB plane without further coalescence due to the high GB decohesion energy. In Mod C due to the solid solution effect of Cu, the lattice dislocation emission energy increases leading to higher grain interior strength in comparison with Mod B. However, the presence of Cu at the GB slightly reduces the cohesive energy of the GB compared to the Mod B. Therefore, larger nanovoids are formed at the GB which tend to accumulate and grow. However, their size and amount are insufficient to cause a full crack formation.

5. Conclusions

We have investigated resistance to hydrogen embitterment of three

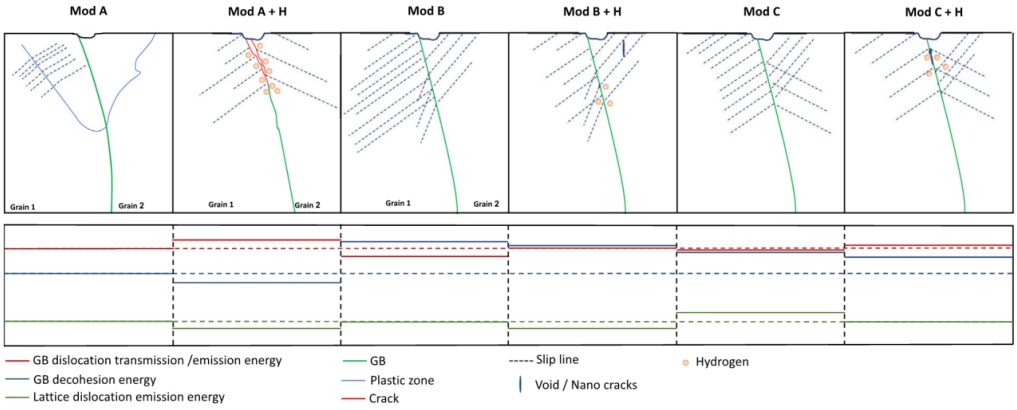

Fig. 13. Schematic representation of the crack propagation and Hydrogen embrittlement mechanism in Mods A, B and C. For simplicity of comparison, the original state lines of the energies in Mod A are continued as dashed lines in other conditions.

modifications of the 725 Ni-based super alloy: a standard modification (Mod A), a standard modification alloyed with 250–350 ppm B (Mod B), and standard modification alloyed with $<$ 100 ppm B and 2.3 wt% Cu (Mod C). All modifications with B have shown a substantial increase in resistance to intergranular GB fracture during in situ H-charging. A detailed GB analysis can be summarized as follows:

- The APT results showed that the added B to the alloy is mainly segregated in the GB and the Cu participated in solid solution at the matrix. In Mod B, part of the alloyed B remains in solid solution, while in Mod C, nearly all added B accumulated in the GB.
- In Mod A, bending in air (H-free condition) resulted in GB work hardening. A high amount of dislocation pile up is found behind the GB. The high accumulated stress leads to distortion and deviation of the GB from its original path. During H-charging, formation of intergranular crack is observed.
- Addition of B improved the HE-resistance of Mod B, however, at the cost of reducing the strength of the alloy. B contributed to the ductility of the alloy by releasing the accumulated stress behind the GB via enhancing the GB dislocation transmission/generation. B also increased the boundary cohesive energy based on DFT results. Therefore in air condition no void/crack is formed. In H environment, nano-voids were observed in either DSBs or GBs. However, the formed nano-voids did not show any effect on the strength and the integrity of the bent beams.
- In Mod C, the loss of strength happened in Mod B is compensated by solid solution hardening by Cu. DFT and APT results showed that Cu tends to deplete at the GBs. Therefore the amount of Cu at the GBs are less than the bulk content. However its presence at the GB reduces the strengthening energy of the GB. As a result, larger nano-voids compared to Mod B were formed at the GB after in situ bending. Albeit, even with the addition of H, no propagating crack is formed in the GB nor in the matrix.

CRediT authorship contribution statement

Iman Taji: Conceptualization, Methodology, Investigation, Visualization, Writing – original draft. **Tarlan Hajilou:** Conceptualization, Methodology, Investigation, Writing – review & editing. **Anna Sophie Ebner:** Investigation, Writing – original draft. **Daniel Scheiber:** Methodology, Simulation, Writing – original draft. **Shabnam Karimi:** Investigation. **Ernst Plesiutschnig:** Resources. **Werner Ecker:** Conceptualization, Writing – review & editing. **Afrooz Barnoush:** Conceptualization, Methodology, Supervision. **Verena Maier-Kiener:** Conceptualization, Supervision. **Roy Johnsen:** Supervision, Writing – review & editing: **Vsevolod I. Razumovskiy:** Methodology, Supervision, Writing – review & editing.

Declaration of Competing Interest

The authors declare that they have no known competing financial interests or personal relationships that could have appeared to influence the work reported in this paper.

Data Availability

The raw/processed data required to reproduce these findings cannot be shared at this time as the data also forms part of an ongoing study.

Acknowledgment

The authors gratefully acknowledge the financial support under the scope of the COMET program within the K2 Center "Integrated Computational Material, Process and Product Engineering (IC-MPPE), Astria" (Project No. 859480). This program is supported by Equinor, Norway and Voestalpine BÖHLER Edelstahl GmbH & Co KG, the Austrian Federal Ministries for Climate Action, Environment, Energy, Mobility, Innovation and Technology (BMK) and for Digital and Economic Affairs (BMDW), represented by the Austrian Research Funding Association (FFG), and the federal states of Styria, Upper Austria, and Tyrol. The computational results presented have been obtained using the Vienna Scientific Cluster (VSC). The Research Council of Norway is acknowledged for the support to the Norwegian Micro- and Nano-Fabrication Facility, NorFab, Norway (Project No. 245963/F50).

Appendix A. Supporting information

Supplementary data associated with this article can be found in the online version at doi:10.1016/j.corsci.2022.110331.

References

[1] R.C. Reed, The Superalloys: Fundamentals and Applications, Cambridge University Press, 2008.
[2] S. Patel, J. deBarbadillo, S. Coryell, Superalloy 718: evolution of the alloy from high to low temperature application, in: Proceedings of the 9th International Symposium on Superalloy 718 & Derivatives: Energy, Aerospace, and Industrial Applications, Springer, 2018, pp. 23–49.
[3] J. Lee, Hydrogen embrittlement of nickel, cobalt and iron-based superalloys, Gaseous Hydrog. Embrittlement Mater. Energy Technol. (2012) 624–667.
[4] Z. Zhang, Z. Yang, S. Lu, A. Harte, R. Morana, M. Preuss, Strain localisation and failure at twin-boundary complexions in nickel-based superalloys, Nat. Commun. 11 (1) (2020) 1–11.

[5] A. Kolagar, N. Tabrizi, M. Cheraghzadeh, M. Shahriari, Failure analysis of gas turbine first stage blade made of nickel-based superalloy, Case Stud. Eng. Fail. Anal. 8 (2017) 61–68.

[6] M. Sujata, M. Madan, K. Raghavendra, M. Venkataswamy, S. Bhaumik, Identification of failure mechanisms in nickel base superalloy turbine blades through microstructural study, Eng. Fail. Anal. 17 (6) (2010) 1436–1446.

[7] T. Gabb, J. Telesman, P. Kantzos, A. Garg, Effects of temperature on failure modes for a nickel-base disk superalloy, J. Fail. Anal. Prev. 7 (1) (2007) 56–65.

[8] E. Alabort, D. Barba, S. Sulzer, M. Lißner, N. Petrinic, R. Reed, Grain boundary properties of a nickel-based superalloy: characterisation and modelling, Acta Mater. 151 (2018) 377–394.

[9] M. Martin, B. Somerday, R. Ritchie, P. Sofronis, I. Robertson, Hydrogen-induced intergranular failure in nickel revisited, Acta Mater. 60 (6–7) (2012) 2739–2745.

[10] Z. Zhang, G. Obasi, R. Morana, M. Preuss, Hydrogen assisted crack initiation and propagation in a nickel-based superalloy, Acta Mater. 113 (2016) 272–283.

[11] M.B. Djukic, G.M. Bakic, V.S. Zeravcic, A. Sedmak, B. Rajicic, The synergistic action and interplay of hydrogen embrittlement mechanisms in steels and iron: Localized plasticity and decohesion, Eng. Fract. Mech. 216 (2019), 106528.

[12] W.W. Gerberich, R.A. Oriani, M.-J. Lji, X. Chen, T. Foecke, The necessity of both plasticity and brittleness in the fracture thresholds of iron, Philos. Mag. A 63 (2) (1991) 363–376, https://doi.org/10.1080/01418619108204854.

[13] I.M. Robertson, P. Sofronis, A. Nagao, M. Martin, S. Wang, D. Gross, K. Nygren, Hydrogen embrittlement understood, Metall. Mater. Trans. B 46 (3) (2015) 1085–1103.

[14] R. Kirchheim, Solid solution softening and hardening by mobile solute atoms with special focus on hydrogen, Scr. Mater. 67 (9) (2012) 767–770.

[15] A. Barnoush, H. Vehoff, Recent developments in the study of hydrogen embrittlement: Hydrogen effect on dislocation nucleation, Acta Mater. 58 (16) (2010) 5274–5285.

[16] K. Nibur, D. Bahr, B. Somerday, Hydrogen effects on dislocation activity in austenitic stainless steel, Acta Mater. 54 (10) (2006) 2677–2684.

[17] D. Wan, Y. Deng, J.I.H. Meling, A. Alvaro, A. Barnoush, Hydrogen-enhanced fatigue crack growth in a single-edge notched tensile specimen under in-situ hydrogen charging inside an environmental scanning electron microscope, Acta Mater. 170 (2019) 87–99.

[18] T. Hajilou, Y. Deng, N. Kheradmand, A. Barnoush, Hydrogen enhanced cracking studies on Fe-3wt% Si single and bi-crystal microcantilevers, philosophical transactions of the royal society a: mathematical, Phys. Eng. Sci. 375 (2098) (2017), 20160410.

[19] M. Iannuzzi, A. Barnoush, R. Johnsen, Materials and corrosion trends in offshore and subsea oil and gas production, npj Mater. Degrad. 1 (1) (2017) 1.

[20] M. Seita, J.P. Hanson, S. Gradečak, M.J. Demkowicz, The dual role of coherent twin boundaries in hydrogen embrittlement, Nat. Commun. 6 (1) (2015) 1–6.

[21] X. Lu, D. Wang, Effect of hydrogen on deformation behavior of alloy 725 revealed by in-situ bi-crystalline micropillar compression test, J. Mater. Sci. Technol. 67 (2021) 243–253.

[22] S. Bechtle, M. Kumar, B.P. Somerday, M.E. Launey, R.O. Ritchie, Grain-boundary engineering markedly reduces susceptibility to intergranular hydrogen embrittlement in metallic materials, Acta Mater. 57 (14) (2009) 4148–4157.

[23] D. Raabe, M. Herbig, S. Sandlöbes, Y. Li, D. Tytko, M. Kuzmina, D. Ponge, P.-P. Choi, Grain boundary segregation engineering in metallic alloys: A pathway to the design of interfaces, Curr. Opin. Solid State Mater. Sci. 18 (4) (2014) 253–261.

[24] R. Wu, A.J. Freeman, G.B. Olson, First principles determination of the effects of phosphorus and boron on iron grain boundary cohesion, Science 265 (5170) (1994) 376–380.

[25] G. DaRosa, P. Maugis, A. Portavoce, J. Drillet, N. Valle, E. Lentzen, K. Hoummada, Grain-boundary segregation of boron in high-strength steel studied by Nano-SIMS and atom probe tomography, Acta Mater. 182 (2020) 226–234.

[26] A. Lozovoi, A. Paxton, Boron in copper: A perfect misfit in the bulk and cohesion enhancer at a grain boundary, Phys. Rev. B 77 (16) (2008), 165413, https://doi.org/10.1103/PhysRevB.74.155416.

[27] S. Zhang, O.Y. Kontsevoi, A.J. Freeman, G.B. Olson, First-principles determination of the effect of boron on aluminum grain boundary cohesion, Phys. Rev. B 84 (13) (2011), 134104.

[28] S. Tamirisakandala, R.B. Bhat, J.S. Tiley, D.B. Miracle, Processing, microstructure, and properties of β titanium alloys modified with boron, J. Mater. Eng. Perform. 14 (6) (2005) 741–746.

[29] C. Lee, G. Han, R. Smallman, D. Feng, J. Lai, The influence of boron-doping on the effectiveness of grain boundary hardening in ni3al, Acta Mater. 47 (6) (1999) 1823–1830.

[30] F.-H. Wang, J.-X. Shang, J.-M. Li, C.-Y. Wang, The effects of boron and hydrogen on the embrittlement of polycrystalline ni3al, Intermetallics 8 (5–6) (2000) 589–593.

[31] P. Kontis, E. Alabort, D. Barba, D.M. Collins, A.J. Wilkinson, R.C. Reed, On the role of boron on improving ductility in a new polycrystalline superalloy, Acta Mater. 124 (2017) 489–500.

[32] Y. Zhao, J. Zhang, Y. Luo, B. Zhang, G. Sha, L. Li, D. Tang, Q. Feng, Improvement of grain boundary tolerance by minor additions of hf and b in a second generation single crystal superalloy, Acta Mater. 176 (2019) 109–122.

[33] X. Li, M. Ou, M. Wang, L. Zhang, Y. Ma, K. Liu, Effect of boron addition on the microstructure and mechanical properties of k4750 nickel-based superalloy, J. Mater. Sci. Technol. 60 (2021) 177–185.

[34] D. Tytko, P.-P. Choi, J. Klöwer, A. Kostka, G. Inden, D. Raabe, Microstructural evolution of a ni-based superalloy (617b) at 700c studied by electron microscopy and atom probe tomography, Acta Mater. 60 (4) (2012) 1731–1740.

[35] A. Jena, M. Chaturvedi, The role of alloying elements in the design of nickel-base superalloys, J. Mater. Sci. 19 (10) (1984) 3121–3139.

[36] H. Guo, M. Chaturvedi, N. Richards, Effect of boron concentration and grain size on weld heat affected zone microfissuring in inconel 718 base superalloys, Sci. Technol. Weld. Join. 4 (4) (1999) 257–264.

[37] I. Taji, T. Hajilou, S. Karimi, F. Schott, E. Plesiutschnig, A. Barnoush, R. Johnsen, Role of grain boundaries in hydrogen embrittlement of alloy 725: single and bi-crystal microcantilever bending study, Int. J. Hydrog. Energy (2022).

[38] T. Hajilou, I. Taji, F. Christien, S. He, D. Scheiber, W. Ecker, R. Pippan, V. I. Razumovskiy, A. Barnoush, Hydrogen-enhanced intergranular failure of sulfur-doped nickel grain boundary: in situ electrochemical micro-cantilever bending vs. dft, Mater. Sci. Eng. A 794 (2020), 139967, https://doi.org/10.1016/j.msea.2020.139967.

[39] A. Harte, M. Atkinson, A. Smith, C. Drouven, S. Zaefferer, J.Q. daFonseca, M. Preuss, The effect of solid solution and gamma prime on the deformation modes in Ni-based superalloys, Acta Mater. 194 (2020) 257–275.

[40] V. Razumovskiy, A. Lozovoi, I. Razumovskii, First-principles-aided design of a new Ni-base superalloy: Influence of transition metal alloying elements on grain boundary and bulk cohesion, Acta Mater. 82 (Supplement C) (2015) 369–377, https://doi.org/10.1016/j.actamat.2014.08.047. ⟨http://www.sciencedirect.com/science/article/pii/S1359645414006612⟩.

[41] V. Razumovskiy, A. Lozovoi, I. Razumovskii, Corrigendum to "first-principles-aided design of a new ni-base superalloy: Influence of transition metal alloying elements on grain boundary and bulk cohesion" [acta mater. 82 (2015) 369-377], Acta Mater. 106 (2016) 401–402, https://doi.org/10.1016/j.actamat.2015.12.030. ⟨http://www.sciencedirect.com/science/article/pii/S1359645415007843⟩.

[42] I. Razumovskii, A. Ruban, V. Razumovskiy, A. Logunov, V. Larionov, O. Ospennikova, V. Poklad, B. Johansson, New generation of ni-based superalloys designed on the basis of first-principles calculations, Mater. Sci. Eng.: A 497 (1) (2008) 18–24, https://doi.org/10.1016/j.msea.2008.08.013. ⟨https://www.sciencedirect.com/science/article/pii/S092150930800974X⟩.

[43] D. Scheiber, L. Romaner, F. Fischer, J. Svoboda, Kinetics of grain boundary segregation in multicomponent systems-the example of a Mo-C-B-O system, Scr. Mater. 150 (2018) 110–114, https://doi.org/10.1016/j.scriptamat.2018.03.011.

[44] Physical Metallurgy of Alloys 718, 925, 725, and 725HS for Service in Aggressive Corrosion Environments, Vol. All Days of NACE CORROSION, nACE-03126. arXiv: https://onepetro.org/NACECORR/proceedings-pdf/CORR03/All-CORR03/NACE-03126/1876627/nace-03126.pdf.

[45] K. Babinsky, R. de Kloe, H. Clemens, S. Primig, A novel approach for site-specific atom probe specimen preparation by focused ion beam and transmission electron backscatter diffraction, Ultramicroscopy 144 (2014) 9–18, https://doi.org/10.1016/j.ultramic.2014.04.003.

[46] M. Thuvander, H.-O. Andrén, A pfim studies of grain and phase boundaries, Mater. Charact. 44 (2000) 87–100, https://doi.org/10.1016/S1044-5803(99)00052-2.

[47] O.C. Hellman, D.N. Seidman, Measurement of the gibbsian interfacial excess of solute at an interface of arbitrary geometry using three-dimensional atomprobe microscopy, Mater. Sci. Eng. A 327 (2002) 24–28, https://doi.org/10.1016/S0921-5093(01)01885-8.

[48] M.S. Hazarabedian, M. Iannuzzi, The role of nano-sized intergranular phases on nickel alloy 725 brittle failure, npj Mater. Degrad. 5 (1) (2021) 1–9.

[49] S. Bechtle, M. Kumar, B.P. Somerday, M.E. Launey, R.O. Ritchie, Grain-boundary engineering markedly reduces susceptibility to intergranular hydrogen embrittlement in metallic materials, Acta Mater. 57 (14) (2009) 4148–4157.

[50] T. Hajilou, Y. Deng, B.R. Rogne, N. Kheradmand, A. Barnoush, In situ electrochemical microcantilever bending test: A new insight into hydrogen enhanced cracking, Scr. Mater. 132 (2017) 17–21.

[51] R.R. Keller, R.H. Geiss, Transmission EBSD from 10 nm domains in a scanning electron microscope, J. Microsc. 245 (3) (2012) 245–251.

[52] Y. Deng, A. Barnoush, Hydrogen embrittlement revealed via novel in situ fracture experiments using notched micro-cantilever specimens, Acta Mater. 142 (Supplement C) (2018) 236–247.

[53] P.E. Blöchl, Projector augmented-wave method, Phys. Rev. B 50 (24) (1994) 17953, https://doi.org/10.1103/PhysRevB.50.17953. ⟨https://link.aps.org/doi/10.1103/PhysRevB.50.17953⟩.

[54] G. Kresse, D. Joubert, From ultrasoft pseudopotentials to the projector augmented-wave method, Phys. Rev. B 59 (3) (1999) 1758, https://doi.org/10.1103/PhysRevB.59.1758. ⟨https://link.aps.org/doi/10.1103/PhysRevB.59.1758⟩.

[55] G. Kresse, J. Hafner, Ab initio molecular dynamics for open-shell transition metals, Phys. Rev. B 48 (1993) 13115–13118, https://doi.org/10.1103/PhysRevB.48.13115. ⟨http://link.aps.org/doi/10.1103/PhysRevB.48.13115⟩.

[56] G. Kresse, J. Furthmuller, Efficiency of ab-initio total energy calculations for metals and semiconductors using a plane-wave basis set, Comput. Mater. Sci. 6 (1) (1996) 15–50, https://doi.org/10.1016/0927-0256(96)00008-0. ⟨http://www.sciencedirect.com/science/article/pii/0927025696000080⟩.

[57] J.P. Perdew, K. Burke, M. Ernzerhof, Generalized gradient approximation made simple, Phys. Rev. Lett. 77 (1996) 3865–3868, https://doi.org/10.1103/PhysRevLett.77.3865. ⟨https://link.aps.org/doi/10.1103/PhysRevLett.77.3865⟩.

[58] H.J. Monkhorst, J.D. Pack, Special points for brillouin-zone integrations, Phys. Rev. B 13 (1976) 5188–5192, https://doi.org/10.1103/PhysRevB.13.5188. ⟨https://link.aps.org/doi/10.1103/PhysRevB.13.5188⟩.

[59] S. He, W. Ecker, R. Pippan, V.I. Razumovskiy, Hydrogen-enhanced decohesion mechanism of the special σ 5 (0 1 2)[1 0 0] grain boundary in Ni with Mo and C solutes, Comput. Mater. Sci. 167 (2019) 100–110, https://doi.org/10.1016/j.commatsci.2019.05.029.

[60] J.R. Rice, J.-S. Wang, Embrittlement of interfaces by solute segregation, Mater. Sci. Eng. A 107 (1989) 23–40, https://doi.org/10.1016/0921-5093(89)90372-9.

[61] C.L. White, W.A. Coghlan, The spectrum of binding energies approach to grain boundary segregation, Metall. Trans. A 8 (9) (1977) 1403–1412, https://doi.org/10.1007/BF02642853.
[62] C.L. White, D.F. Stein, Sulfur segregation to grain boundaries in Ni3Al and Ni3(AI, Ti) alloys, Metall. Trans. A 9 (1) (1978) 13–22, https://doi.org/10.1007/BF02647165.
[63] K. Leitner, D. Scheiber, S. Jakob, S. Primig, H. Clemens, E. Povoden-Karadeniz, L. Romaner, How grain boundary chemistry controls the fracture mode of molybdenum, Mater. Des. 142 (2018) 36–43, https://doi.org/10.1016/j.matdes.2018.01.012. ⟨http://linkinghub.elsevier.com/retrieve/pii/S0264127518300121⟩.
[64] D. Scheiber, V.I. Razumovskiy, P. Puschnig, R. Pippan, L. Romaner, Ab initio description of segregation and cohesion of grain boundaries in W-25 at% Re alloys, Acta Mater. 88 (2015) 180–189, https://doi.org/10.1016/j.actamat.2014.12.053.
[65] A. Oudriss, J. Creus, J. Bouhattate, E. Conforto, C. Berziou, C. Savall, X. Feaugas, Grain size and grain-boundary effects on diffusion and trapping of hydrogen in pure nickel, Acta Mater. 60 (19) (2012) 6814–6828.
[66] Y. Aboura, D. Martelo, R. Morana, R. Akid, K. Moore, Characterising hydrogen induced cracking of alloy 625. using correlative SEM-EDX and NanoSIMS, Corros. Sci. 181 (2021), 109228.
[67] D. Li, R.P. Gangloff, J.R. Scully, Hydrogen trap states in ultrahigh-strength AERMET 100 steel, Metall. Mater. Trans. A 35 (3) (2004) 849–864.
[68] C. Wang, Y. Guo, J. Guo, L. Zhou, Microstructural stability and mechanical properties of a boron modified Ni-Fe based superalloy for steam boiler applications, Mater. Sci. Eng.: A 639 (2015) 380–388.
[69] Y. Ogino, T. Yamasaki, A remedial effect of boron on intergranular hydrogen-embrittlement of nickel, Scr. Metall. 15 (8) (1981) 821–824.
[70] T. Chaki, Grain boundary engineering in ordered Ni3Al for improving ductility, MRS Online Proc. Libr. Arch. 458 (1996).
[71] J. Xu, X. Sun, Q. Liu, W. Chen, Hydrogen permeation behavior in IN718 and GH761 superalloys, Metallurgical and Materials Transactions A 25 (3) (1994) 539–544.
[72] M. Yamaguchi, Y. Nishiyama, H. Kaburaki, Decohesion of iron grain boundaries by sulfur or phosphorous segregation: First-principles calculations, Phys. Rev. B - Condens. Matter Mater. Phys. 76 (3) (2007), https://doi.org/10.1103/PhysRevB.76.035418.
[73] M. Yamaguchi, M. Shiga, H. Kaburaki, Energetics of segregation and embrittling potency for non-transition elements in the Ni 5 (012) symmetrical tilt grain boundary: a first-principles study, J. Phys.: Condens. Matter 16 (23) (2004) 3933–3956, https://doi.org/10.1088/0953-8984/16/23/013.
[74] A.S. Ebner, S. Jakob, H. Clemens, R. Pippan, V. Maier-Kiener, S. He, W. Ecker, D. Scheiber, V. Razumovskiy, Grain boundary segregation in Ni-base alloys: a combined atom probe tomography and first principles study, submitted, Acta Mater. (2021).
[75] S.I. Hong, C. Laird, Mechanisms of slip mode modification in fcc solid solutions, Acta Metall. Et. Mater. 38 (8) (1990) 1581–1594.
[76] L. Xiao, D. Chen, M. Chaturvedi, Shearing of γ ¨precipitates and formation of planar slip bands in inconel 718 during cyclic deformation, Scr. Mater. 52 (7) (2005) 603–607.
[77] L. Xiao, D. Chen, M. Chaturvedi, Effect of boron on fatigue crack growth behavior in superalloy in 718 at rt and 650c, Mater. Sci. Eng.: A 428 (1–2) (2006) 1–11.
[78] Y. Ogawa, O. Takakuwa, S. Okazaki, Y. Funakoshi, S. Matsuoka, H. Matsunaga, Hydrogen-assisted fatigue crack-propagation in a ni-based superalloy 718, revealed via crack-path crystallography and deformation microstructures, Corros. Sci. 174 (2020), 108814.
[79] I. Robertson, H. Birnbaum, P. Sofronis, Hydrogen effects on plasticity, Dislocations Solids 15 (2009) 249–293.
[80] Z. Shen, R. Wagoner, W. Clark, Dislocation and grain boundary interactions in metals, Acta Metall. 36 (12) (1988) 3231–3242.
[81] G. Dehm, B.N. Jaya, R. Raghavan, C. Kirchlechner, Overview on micro-and nanomechanical testing: New insights in interface plasticity and fracture at small length scales, Acta Mater. 142 (2018) 248–282.
[82] P.J. Imrich, C. Kirchlechner, C. Motz, G. Dehm, Differences in deformation behavior of bicrystalline cu micropillars containing a twin boundary or a large-angle grain boundary, Acta Mater. 73 (2014) 240–250.
[83] P. Rodriguez, Serrated plastic flow, Bull. Mater. Sci. 6 (4) (1984) 653–663.
[84] K. Ng, A. Ngan, Deformation of micron-sized aluminium bi-crystal pillars, Philos. Mag. 89 (33) (2009) 3013–3026.
[85] T. Lee, I. Robertson, H. Birnbaum, Interaction of dislocations with grain boundaries in Ni3Al, Acta Metall. Et. Mater. 40 (10) (1992) 2569–2579.
[86] G. Bond, I. Robertson, H. Birnbaum, Effect of boron on the mechanism of strain transfer across grain boundaries in Ni3Al, J. Mater. Res. 2 (4) (1987) 436–440.
[87] M. Mills, S. Goods, S. Foiles, J. Whetstone, The influence of boron segregation on the structure and mechanical properties of boundaries in bicrystals of Ni3Al, Scr. Metall. Et. Mater. 25 (6) (1991) 1283–1288.
[88] P. Zhou, J. Yu, X. Sun, H. Guan, Z. Hu, The role of boron on a conventional nickel-based superalloy, Mater. Sci. Eng.: A 491 (1–2) (2008) 159–163.
[89] Y. Guo, D.M. Collins, E. Tarleton, F. Hofmann, A.J. Wilkinson, T.B. Britton, Dislocation density distribution at slip band-grain boundary intersections, Acta Mater. 182 (2020) 172–183.
[90] E. George, C. Liu, Brittle fracture and grain boundary chemistry of microalloyed nial, J. Mater. Res. 5 (4) (1990) 754–762.
[91] J. Luan, Z. Jiao, L. Heatherly, E. George, G. Chen, C. Liu, Effects of boron on the fracture behavior and ductility of cast Ti-6Al-4V alloys, Scr. Mater. 100 (2015) 90–93.
[92] P. Lejcek, Grain Boundary Segregation in Metals, Springer, Berlin Heidelberg, Berlin, 2010.
[93] S. Wang, M.L. Martin, P. Sofronis, S. Ohnuki, N. Hashimoto, I.M. Robertson, Hydrogen-induced intergranular failure of iron, Acta Mater. 69 (2014) 275–282.
[94] D.E. Page, K.F. Varela, O.K. Johnson, D.T. Fullwood, E.R. Homer, Measuring simulated hydrogen diffusion in symmetric tilt nickel grain boundaries and examining the relevance of the borisov relationship for individual boundary diffusion, Acta Mater. (2021), 116882.
[95] Z. Tarzimoghadam, D. Ponge, J. Klöwer, D. Raabe, Hydrogen-assisted failure in Ni-based superalloy 718 studied under in situ hydrogen charging: the role of localized deformation in crack propagation, Acta Mater. 128 (2017) 365–374.
[96] X. Lu, D. Wang, D. Wan, Z. Zhang, N. Kheradmand, A. Barnoush, Effect of electrochemical charging on the hydrogen embrittlement susceptibility of alloy 718, Acta Mater. 179 (2019) 36–48.
[97] I. Adlakha, K. Solanki, Critical assessment of hydrogen effects on the slip transmission across grain boundaries in α -Fe, Proc. R. Soc. A: Math., Phys. Eng. Sci. 472 (2185) (2016), 20150617.
[98] J. Cohron, E. George, L. Heatherly, C. Liu, R. Zee, Hydrogen-boron interaction and its effect on the ductility and fracture of Ni3Al, Acta Mater. 45 (7) (1997) 2801–2811.
[99] Y. Wu, X. Li, Y. Wang, First-principles study of the influence of lattice misfit on the segregation behaviors of hydrogen and boron in the Ni-Ni3Al system, Acta Mater. 55 (14) (2007) 4845–4852.

Paper III: Hydrogen-enhanced intergranular failure of sulfur-doped nickel grain boundary: In situ electrochemical micro-cantilever bending vs. DFT

Tarlan Hajilou[a,*], Iman Taji[a], Frederic Christien[b], Shuang He[c,d], Daniel Scheiber[c], Werner Ecker[c], Reinhard Pippan[e], Vsevolod I. Razumovskiy[c], Afrooz Barnoush[a]

[a]Department of Engineering Design and Materials, Norwegian University of Science and Technology, No. 7491 Trondheim, Norway

[b]Mines Saint-Etienne, Univ Lyon, CNRS, UMR 5307 LGF, Centre SMS, F-42023 Saint-Etienne, France

[c]Materials Center Leoben Forschung GmbH, Roseggerstraße 12, 8700 Leoben, Austria [d]Department Materials Science, Montanuniversität Leoben, Jahnstraße 12, 8700 Leoben, Austria

[e]Erich Schmid Institute of Materials Science, Austrian Academy of Sciences, Jahnstraße 12, 8700 Leoben, Austria

Materials Science and Engineering: A 794 (2020): 139967.

https://doi.org/10.1016/j.msea.2020.139967.

Materials Science & Engineering A 794 (2020) 139967

Contents lists available at ScienceDirect

Materials Science & Engineering A

journal homepage: www.elsevier.com/locate/msea

Hydrogen-enhanced intergranular failure of sulfur-doped nickel grain boundary: In situ electrochemical micro-cantilever bending vs. DFT

Tarlan Hajilou [a,*], Iman Taji [a], Frederic Christien [b], Shuang He [c,d], Daniel Scheiber [c], Werner Ecker [c], Reinhard Pippan [e], Vsevolod I. Razumovskiy [c], Afrooz Barnoush [a]

[a] Department of Mechanical and Industrial Engineering, Norwegian University of Science and Technology, No. 7491 Trondheim, Norway
[b] Mines Saint-Etienne, Univ Lyon, CNRS, UMR 5307 LGF, Centre SMS, F-42023 Saint-Etienne, France
[c] Materials Center Leoben Forschung GmbH, Roseggerstraße 12, 8700 Leoben, Austria
[d] Department Materials Science, Montanuniversität Leoben, Jahnstraße 12, 8700 Leoben, Austria
[e] Erich Schmid Institute of Materials Science, Austrian Academy of Sciences, Jahnstraße 12, 8700 Leoben, Austria

ARTICLE INFO

Keywords:
Hydrogen embrittlement
Nickel
Sulfur segregation
Intergranular cracking
Density functional theory
Micro-cantilever

ABSTRACT

Intergranular failure of nickel (Ni) single grain boundaries (GBs) owing to the segregation of sulfur (S), hydrogen (H), and their co-segregation has been investigated by employing micro-cantilever bending tests and density functional theory (DFT) calculations. A pure Ni GB shows completely plastic behavior with no fracture observed in the experiments. Electrochemical H-charging of the sample with no S present in the GB leads to a crack formed at the notch tip, which propagates by means of the mixed plastic–brittle fracture mode. Cantilever testing of the H-charged GB with S results in a clear brittle fracture of the GB. The co-segregation of S and H shifts the sudden drop in the load–displacement curves to smaller values of displacement. This is explained by the combined effect of these elements on the work of separation of the selected GB leading to severely decreased GB cohesion.

1. Introduction

Grain boundaries (GBs) are known as a common defect in metals and their alloys. As they possess higher energy compared with the bulk crystal, GBs are preferential sites for impurities to segregate. This segregation process is thermodynamically favorable if it reduces the total energy of the system. Depending on the segregation energy difference between the GB and free surface formed during fracture, segregated elements in the GB can be evaluated in terms of their influence on the GB embrittlement within the framework of the Rice–Wang theory of brittle fracture [1–3]. Fracture mode transition can occur due to (i) segregated embrittling impurities, hydrogen or alloying elements, (ii) precipitate formation and (iii) embrittling environmental species such as hydrogen adsorption to the GB [4]. Intergranular (IG) fracture is one of the most dangerous technical failures in metals and alloys which proceeds quickly owing to the interconnected network of the GBs. This type of failure is usually hard to detect prior to final rupture. The focus of this study is on nickel (Ni), one of the basic engineering materials, which has a face-centered cubic (FCC) crystal structure. Owing to the greater number of slip systems available in this structure, it is intrinsically ductile [5]. However, IG fracture of this metal can occur even at room temperature; this is usually associated with GB segregation of atoms of impurities [6,7].

Various elements can segregate to Ni GBs. Comparing the embrittling effect of the different solute elements such as Sn, Sb, P, and S to the Ni GB, it was found that S was one of the most detrimental GB segregating elements owing to its high segregation potency and its major effect on the mechanical properties of the interfaces [8–10]. Sulfur (S) segregation to GBs in Ni is reported to convert the fracture mode of the material to IG failure by changing the local cohesive strength of the GB [5]. Atomic hydrogen (H) is another detrimental element that can be introduced into the material throughout the manufacturing process or can be adsorbed under service conditions such as exposure to cathodic protection, corrosion processes, or environments containing H gas. The embrittling effect of H in Ni and Ni alloys, and the correlation between the solute H concentration and the fracture mode transition have been studied extensively [11–13] and a number of models to explain the metal-H interaction have been suggested. Some of these mechanisms such as hydrogen-enhanced decohesion (HEDE) [14] are put forward based on the H effect on the cohesive strength weakening by dilatation of interatomic bonding [15]. Since the HEDE mechanism does not consider the plastic interaction of the H with

* Corresponding author.
E-mail address: tarlan.hajilou@ntnu.no (T. Hajilou).

https://doi.org/10.1016/j.msea.2020.139967
Received 19 March 2020; Received in revised form 4 July 2020; Accepted 17 July 2020
Available online 21 July 2020
0921-5093/

dislocations, other mechanisms such as adsorption-induced dislocation emission (AIDE) and hydrogen-enhanced localized plasticity (HELP) have been proposed. Based on the AIDE mechanism weakening of the interatomic bonds due to adsorbed H results in the dislocation emission from the crack tip which leads to void nucleation and their coalescence ahead of the crack [4]. Effect of absorbed H on lattice dislocations, however, is considered in the HELP mechanism. This mechanism suggested the increased mobility of the dislocations motion and their tendency to pack closer together in the presence of H [16]. Almost all mechanisms agree with each other on the role of H in dislocation nucleation enhancement which is explained by the defectant theory [17], based upon thermodynamic considerations. This model suggests that the dislocation formation energy is reduced by H segregation to the dislocations. Beyond this step, usually a combination of the embrittling mechanisms are favored to explain the nano–micro scale phenomena behind the observed degradation effects in the presence of H. As an example, IG cracking of Ni in the presence of H is explained by HELP mediated HEDE model [18]. Plasticity enhancement by H increases the GB stress level. In addition, transport of H by dislocations to the GBs increases the GB H concentration and H accumulation in the GB facilitates the reduction of the GB cohesive strength. Other possible mechanisms are also proposed in the literature [19]. Despite the discrepancies on the involved embrittlement mechanism, there is agreement in the literature on fracture mode transition to IG fracture by increasing the H fugacity in the material [11]. Up to now, most IG failure studies investigating the effect of segregated impurities such as H or S or their co-segregation on the mechanical properties of the alloy have been confined to polycrystalline materials. Diversity in the GB type and heterogeneity of the segregated element concentration in each GB results in different critical S or H concentration amounts that can induce IG cracking [11,20]. Therefore, using polycrystalline materials, it is difficult to find a direct relationship between a selected GB type and segregation parameters and the mechanical response of that specific GB. However, a few studies can be found that have investigated a single GB. Vehoff et al. examined the effect of S and H on the GB embrittlement by growing a bi-crystal [21]. However, this approach to test a specific GB is quite difficult and also suffers from a lack of reproducibility.

Following the introduction of focused ion beam (FIB) scanning electron microscopy (SEM) technology, nowadays it is possible to make a series of identical micrometer-sized specimens in favorable positions on the material. The micro-cantilever bending test, which has drawn a lot of attention since its first use in 2005 [22], is an interesting method to explore the micro-mechanical variation of materials [23]. Putting a specific GB in the micro-cantilever makes it more convenient to study the segregation and environmental parameters on the mechanical behavior of the GB [24,25]. Combining micro-milling with an electron back-scattered diffraction (EBSD) method enables us to select a favorable GB and test a series of identical cantilevers under different testing conditions. In addition, by confining the testing size to a micrometer scale and considering a specific GB, it is possible to compare the results with atomistic calculations, which can provide a fundamental understanding of the GB segregation and quantify the segregation-induced changes in GB cohesion. One of the prominent examples is the simulation of HEDE of GB in Ni [9,26–29], which has shown that atomic H tended to segregate to the Ni GB and demonstrated the GB embrittling effect. Moreover, the synergistic effect between segregated impurities has drawn attention to the investigation of solute co-segregation at GBs, such as H–carbide co-segregation [30,31], H–Cr co-segregation in α-Fe GB [32,33], C–O co-segregation in α-Ti GB [34], C, B, O, Fe, and Hf co-segregation in Mo GB [35], or H–C and H–Mo co-segregation in Ni GB [29]. Although S is known to segregate to Ni GBs and decrease GB cohesion [10,36–39], the H–S interaction and its co-segregation effect as well as the kinetics of H–S segregation in Ni GB have not been studied sufficiently at the atomic level.

In this study, micro-mechanical testing is combined with atomistic calculations to study the co-segregation effect of S and H in selected GBs. Selected GBs are tested with the micro-cantilever method to investigate the interaction of segregated impurities in GBs and their effect on the mechanical properties. From the computational side, this study applies density functional theory (DFT) to investigate the fundamentals of segregation and co-segregation of H with S in Ni and its effect on the GB cohesive strength using the Rice–Thomson–Wang theory of interface embrittlement [3,40]. With this approach, the focus is on the HEDE mechanism of H embrittlement (HE), which is expected to be the dominant mechanism at high H concentrations [15]. Furthermore, the kinetics of H and S segregation to a Ni GB are investigated using our calculated segregation energies DFT and the McLean isotherm [1,41–43]. The results of this study can be used to strengthen Ni and its alloys via GB engineering against environmental conditions.

2. Method

2.1. Materials and characterization

Two types of Ni samples were used in this study: (i) a pure Ni sample; and (ii) a S-doped Ni sample. The polycrystalline high-purity Ni sample (99.99%) was produced by the zone refining process. Disk-shaped samples with a diameter of 12 mm and thickness of 4 mm were annealed in vacuum at 1250 °C for 72 h followed by furnace cooling as the final heat treatment step. The annealing process lead to grain growth with an average size of ~2 mm and GBs perpendicular to the surface of the sample [44]. The S-doped sample contains 5.4 wt ppm of S in solid solution condition measured by a glow discharge mass spectroscopy technique. Following casting, hot rolling and cold rolling processes were carried out to decrease the thickness of the ingot to 3 mm. Afterwards, the material was annealed 72 h at 1300 °C and 24 h at 1000 °C followed by water cooling. The average grain size of ~350 μm was obtained at this step. Equilibrating the material for 60 days at 600 °C resulted in S segregation to the GBs. Wavelength dispersive X-ray spectroscopy (WDS) measurements were conducted to detect the segregated S amount at the GBs as described in [45]. Sulfur was the only segregated element detected at the GBs. The S measurement profiles alongside the corresponding SEM images of the GBs are shown in Fig. 1. The measured S content was corrected by obtaining the GB angle relative to the sample surface using a FIB (Table 1). According to the measurements, the amount of S at the GB can vary between 27 and 57 ng cm^{-2} .

The sample surfaces were prepared by normal grinding and finally electropolished in a solution of 1 Molar methanolic H_2SO_4 to reach a maximum surface roughness of ~1 nm in a surface with an area of 100 μm^2 [46]. The electropolishing process was carried out at 30 V for 30 s. EBSD characterization was used to select the GBs of interest in both pure and S-doped Ni samples.

2.2. Micro-cantilever milling and testing

Bi-crystal micro-cantilevers were milled by the FEI Helios DualBeam™ FIB system on the GBs listed in Table 2 and highlighted by arrows in Fig. 2(a) and (b) to the dimensions presented in Fig. 2(c). The GB angle relative to the sample surface was checked to be in the range of 80–90° prior to milling of the bi-crystal beams as shown in Fig. 2(c_1) and (c_2). The tested GB in the pure Ni sample is named PNi1. For the S-doped Ni samples, one with a random GB was named NiS1 and another sample with a Σ5-type GB was named NiS2. To obtain a clean surface, the ion current density of 98 pA at 30 kV was selected during the final cleaning step. To intentionally intensify the stress concentration to the GB, a notch with the very low current density of 9.8 pA was milled aiming the GB to be positioned directly below the notch.

The micro beam bending tests were performed in two H-free and in situ electrochemical H-charged conditions using Hysitron TI 950

Table 1
Sulfur content and structural information of the selected GBs.

GB ID	WDS measured GB S content (ng cm^{-2})	GB angle vs. sample surface (°)	Corrected S content (ng cm^{-2})	Sigma	Misorientation angle (°)
GB1	56.8	82.4	56.3	–	54.2
GB2	41.9	28.8	20.2	–	3.6
GB3	27.3	92	27.3	5	35.6

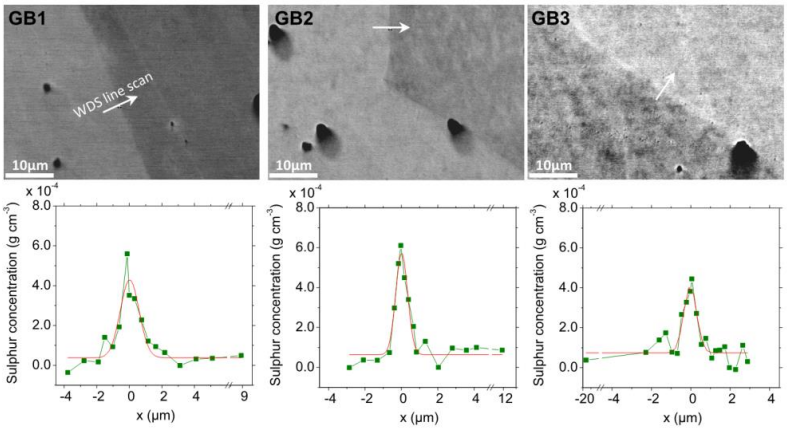

Fig. 1. Sulfur concentration profiles of three different GBs across the indicated lines in the SEM images measured by WDS on the Ni sample with 5.4 wt.ppm. bulk S, annealed 60 days at 600 °C.

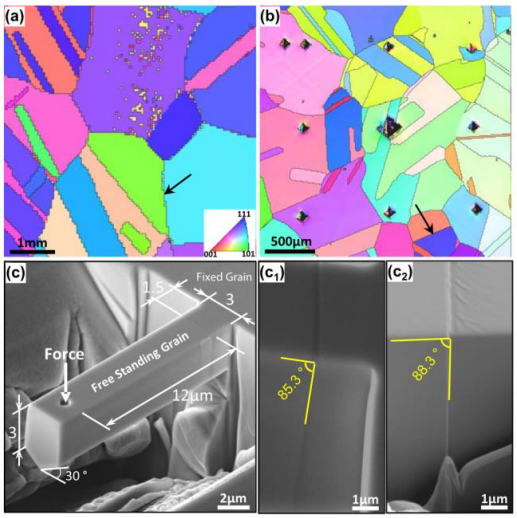

Fig. 2. Inverse pole figure map of the studied (a) pure Ni and (b) S-doped Ni samples. The selected GBs for cantilever milling are marked by black arrows. (c) Representative dimensions of the bi-crystal cantilevers. Selected GB angle to the sample surface in (c_1) pure Ni and (c_2) S-doped specimen NiS1.

TriboIndenter® system. Displacement control mode was used to bend the cantilevers with a displacement rate of 2 nm s^{-1} at room temperature. A long shaft conical tip with a nominal tip radius of 500 nm was used for bending the cantilevers in liquid. A miniaturized three-electrode electrochemical setup consisting of a platinum counter, working (test material), and Hg/$HgSO_4$ reference electrodes was used in this study. The reference electrode was connected to the cell through a double junction integrated to the TriboIndenter to perform the in situ bending tests [47,48].

The micro-beams were charged with a cathodic current density in the range of −60 to −100 μA cm^{-1} at −1450 to −1600 mV potential versus the Hg/$HgSO_4$ reference electrode. A glycerol-based solution with the composition of 1.3 M borax in glycerol mixed with 20% distilled water was used as the H-charging electrolyte [49]. Additional bending tests were performed on the GB called NiS2, which was H-charged by the glycerol-based solution with the addition of 0.002 M $Na_2S_2O_4$ to the solution as the H-recombination poison. High-resolution SEM imaging and cross-sectional slicing by FIB were used to track the crack propagation path versus the GB position.

2.3. Computational details

Spin polarized DFT calculations have been performed using the projector-augmented wave (PAW) [50,51] method as implemented in the Vienna *Ab initio* simulation package (VASP) [52,53]. The Perdew–Burke–Ernzerhof (PBE) form of generalized gradient approximation (GGA) has been used for the exchange–correlation potential [54]. The plane-wave basis set cutoff energy has been set to 400 eV. The convergence criteria of self-consistent calculations have been set to 10^{-5} eV/cell for the total energy and to 9×10^{-3} eV/Å for the atomic forces. The integration over the Brillouin zone has been done using the 4 × 4 × 1 Monkhorst–Pack *k*-mesh [55] for all slab geometry calculations and using the 4 × 4 × 4 *k*-mesh in the 3 × 3 × 3 (conventional FCC cell) bulk supercell calculations. The lattice parameter has been fixed to 3.515 Å [29] and only the ions have been allowed to relax in all slab and bulk calculations. The Ni Σ5(012) coincidence site lattice (CSL) symmetric tilt GBs has been modeled using a 76-atom GB slab with 19 layers and 4 atoms/layer [29]. The Ni Σ5(012) GB structure used in this work and an illustration of GB cleavage are shown in Fig. 3.

The site preference of H and S impurities in the bulk of FCC Ni has been studied by means of DFT calculations in a number of

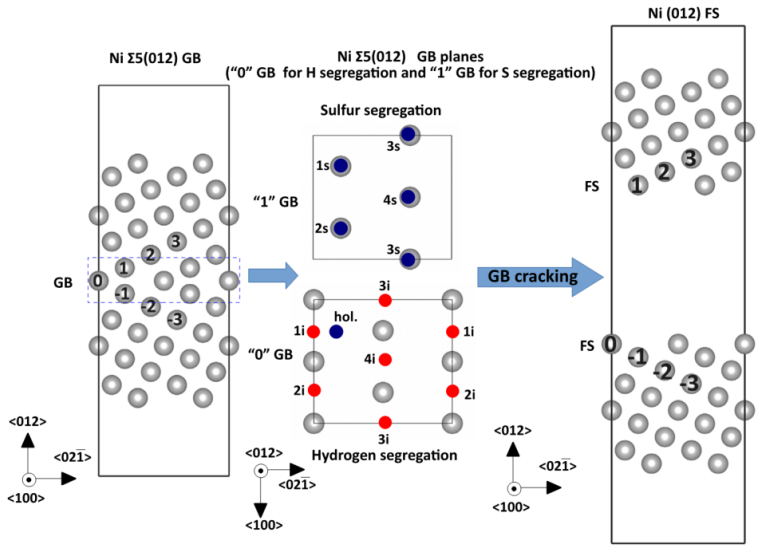

Fig. 3. Illustration of cracking at Ni Σ 5 (012) [100] symmetric tilt GB. GB layers "0" and "1" with interstitial H and substitutional S atoms are also shown.

Table 2
Measured GB misorientation angle and corresponding information in pure Ni (PNi1) and S-doped (NiS1 and NiS2) specimens.

GB ID	Misorientation angle (°)	Axis			Sigma	Plane 1 (fixed grain)			Plane 2 (free-standing grain)		
		h	*k*	*l*		*u*	*v*	*w*	*u*	*v*	*w*
PNi1	47.3	–2	12	19	–	16	19	14	–4	–29	–8
NiS1	46.6	21	5	16	–	–9	–4	4	2	–21	–12
NiS2	35.6	1	–29	1	5	18	–17	10	18	–17	9

publications [28,29,56–58]. The results have shown that H prefers to occupy the octahedral interstitial site [28,29,57,58] and S substitutes the lattice sites [56,57] in the bulk. Here, we use these results and define the GB segregation energy as the total energy difference between the bulk of the material with an impurity atom occupying the most-stable site (interstitial octahedral for H and substitutional for S) and the system with an impurity atom situated at the GB (both substitutional and interstitial sites are considered). The methodology to obtain GB segregation energies (E_{seg}^{gb}) and the work of separation W_{sep} from DFT calculations is described in detail in [10,29].

The GB enrichment of H and S at $T > 0$ has been modeled by means of a modified McLean isotherm [1,41–43], which takes as input GB segregation energy profiles from DFT calculations. In contrast to the classical equilibrium segregation isotherm, the used model considers the possible effects of grain size (solute depletion in the bulk) and the kinetics of segregation. The details of the model are given in [42,43].

The ideal work of separation W_{sep} is a fundamental thermodynamic quantity that controls the mechanical strength of an interface. It has been chosen to evaluate the resistance of the selected GB to decohesion. A reduction in W_{sep} indicates a reduction in the cohesive strength of an interface. However, it does not automatically mean that the interface will fracture in a brittle manner [3]. Another condition has to be satisfied: $W_{sep} < G_{disl}$, where G_{disl} is the minimal energy per unit area of crack advance required to emit a single dislocation. This energy can be estimated to be in the range between 1 and 3 J/m^2 for Ni depending on the applied shear stress level, orientation of the GB, temperature, and the stress rate [59]. An alternative way of estimating the brittle to ductile fracture mode is R, i.e., the ratio of W_{sep} to twice the free surface energy of the metal [60,61]:

$$R = \frac{W_{sep}}{2\gamma_{fs}^{PCP}}, \tag{1}$$

where γ_{fs}^{PCP} denotes the surface energy of the preferred cleavage plane, which for FCC metals is mainly the (111) plane [62]. Free surface energy of Ni (111) surface is obtained by $\gamma_{fs}^{PCP} = (E_{fs}\text{-}N * \epsilon_0)/2A_{fs}$, where E_{fs} is the total energy of the surface slab, N is the total number of atoms, and A_{fs} the area of surface slab. If R is close to unity, transgranular cleavage is expected, whereas for lower values IG fracture is expected.

3. Results

3.1. Bending of the bi-crystal micro-cantilevers

3.1.1. Pure nickel GB

Fig. 4(a) shows the representative load–displacement (L–D) curves of the pure Ni bi-crystal micro-beams obtained in two different experimental conditions of H-free environment and in situ electrochemical H-charging for 2 and 3 h. Although the elastic stiffness is well matched for the two sets of the curves and all the tested beams have a relatively similar yield point, there are obvious differences in the plastic regime. The cantilever bent in H-free condition shows slight hardening up to reaching the maximum load at ~2.5 μm displacement follows by gradual reduction in the flow curve to the final 5 μm displacement. From Fig. 4(a) it can also be inferred that the work hardening rate of the H-charged beams is higher than in the H-free condition. In addition,

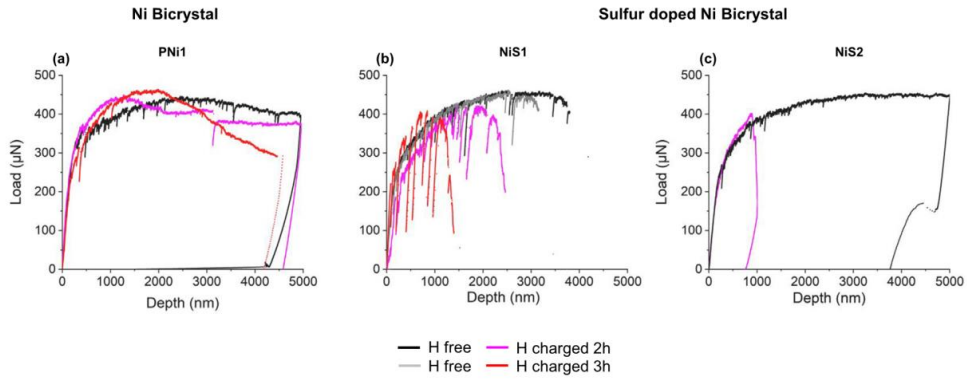

Fig. 4. Load–displacement curves of the (a) pure Ni (GB PNi1 in Table 2) and (b) and (c) S-doped (GBs NiS1 and NiS2 in Table 2, respectively) bi-crystal beams tested with H-free and in situ electrochemical H-charging conditions. (For interpretation of the references to color in this figure legend, the reader is referred to the web version of this article.)

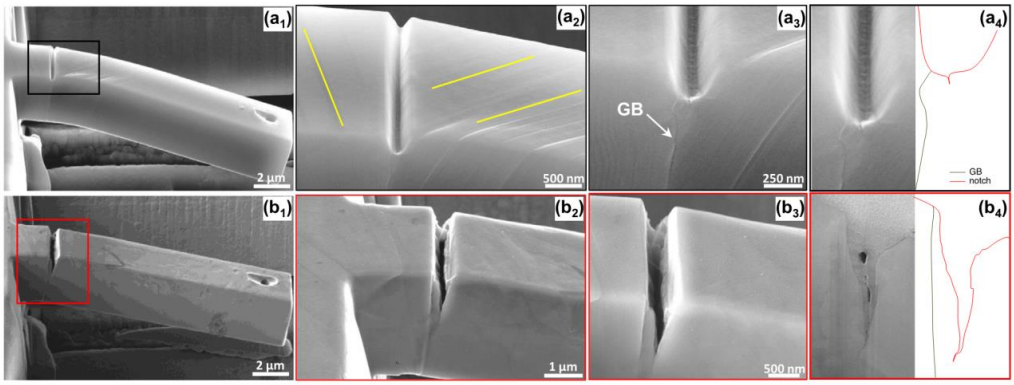

Fig. 5. Post-deformation secondary electron images from the side view of the pure Ni bi-crystal beams (GB PNi1 in Table 2) tested with H=free (a_1)–(a_3) and in situ H-charging (b_1)–(b_3) conditions. (For interpretation of the references to color in this figure legend, the reader is referred to the web version of this article.)

the maximum load of the H-charged beams reaches higher values in comparison with H-free beams. The same phenomenon is reported for Ni–H systems by others and it is believed that the interaction between H and dislocations can be the reason for such increases in load and hardening rate [63]. In the case of H-charged beams, the reduction in the flow curve place at a displacement of ~1 to 1.5 μm. The continuous decrease in the loading force of the H-charged beams can be an indication for the H-induced cracking and decrease in the cross-sectional length of the beams, which leads to a reduction in the required force for the test continuation.

Fig. 5(a_1)–(a_3) and (b_1)–(b_3) shows the post-deformation micrographs of the pure Ni bi-crystal beams bent in H-free and H-charged conditions, respectively. As is evident from Fig. 5(a_1 and a_2) for the H-free condition, the notch is blunted along abundant slip traces visible in the top and the cross-sectional surfaces in adjacent crystals of the beam. According to Schmid's law, the observed slip traces in the free-standing and the fixed side of the bi-crystal beam are due to the activation of the dislocation on the (−1 −1 1) plane in fixed-grain and the (1 −1 −1) plane with Schmid value of 0.35 and 0.48, respectively. This phenomenon demonstrates that the plasticity during the deformation is not only present in the notch area, but also spreads out to the fixed and free-standing grains in the bi-crystal beam as shown by yellow dashed lines. Fig. 5(a_3) and (a_4) exhibits the GB positioned beneath the notch withstanding the plasticity with no evidence of IG cracking. The schematic diagram shows the deviation of the GB from its original straight form, which displays a great amount of plasticity beneath the notch. The observed chain of the micro-voids in the notched area (Fig. 5(a_3)) is also a strong proof for the domination of plasticity in the H-free beams. In contrast to the beams bent in the H-free condition, crack propagation from the notch position was observed for the H-charged beams, which was the reason for the continuous decrease in the corresponding *L–D* curve in Fig. 4(a). A closer cross-sectional view of the cracked beam in Fig. 5(b_2) illustrates fewer slip traces compared with H-free tested beams, which is an indication for the lower plasticity and its confinement to the notch area in the H-charged beams. From this figure, it is also obvious that the crack did not follow the GB path as depicted in the schematic diagram. Alternatively, it has initiated from the notch itself and propagates in zigzag-shaped form in the fracture surface. Further slicing through the thickness of the beam by the FIB (Fig. 5(b_4)) has also demonstrated that the crack is not IG and it propagates to the neighboring grain.

3.1.2. Sulfur-doped GB

The *L–D* curves of the S-doped bi-crystal beams with the GB NiS1 and NiS2 are shown in Fig. 4(b) and (c), respectively. For NiS1 cantilevers, the bent beams show a rapid decrease in the load after reaching a maximum load of ~450 and ~400 μN in the H-free and H-charged environmental conditions, respectively. The sharp load reduction with considerably higher slope compared with the pure Ni results is attributed to the detrimental effect of the S impurity segregation to the

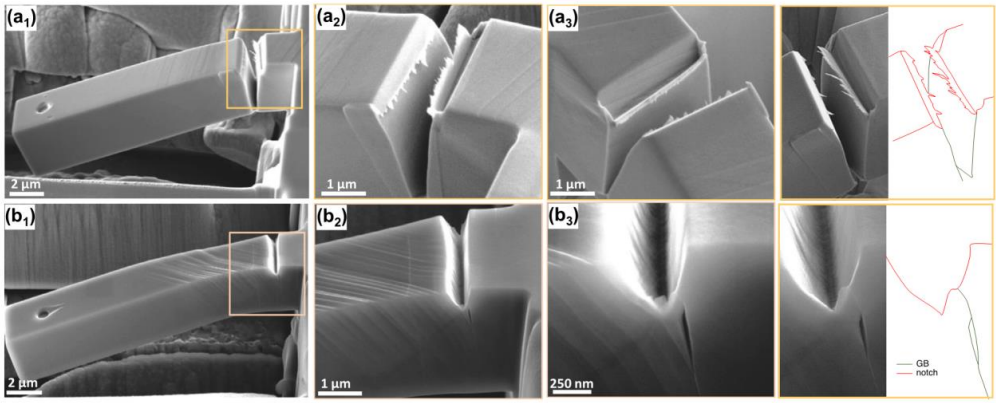

Fig. 6. Secondary electron images from the side view of the bi-crystal beams on the S-doped sample for (a_1)–(a_3) NiS1 and (b_1)–(b_3) NiS2 in Table 2 bent with H-free condition. (For interpretation of the references to color in this figure legend, the reader is referred to the web version of this article.)

GB. Testing the beams in the H-charged condition decreased the displacement to about 2.5 and 1.5 μm after 2 and 3 h of charging. However, the GB embrittling degree of the material is strongly dependent on the content of the segregated elements and also the type of the subjected GB. To investigate this, another type of GB with different misorientation angle and segregated S content was examined. Fig. 4(c) shows the *L–D* curve of the NiS2 GB with 27.3 ng cm^{-2} S. This GB is a $\Sigma 5$ type and has around 11° misorientation lower than the NiS1. In the H-free condition, no rapid load drop is observed in NiS2 in contrast to NiS1 beams and the load is leveled off on the maximum load of ~450 μN up to the final displacement of 5 μm. However, introducing H into the S-doped GB caused a distinct change in the *L–D* behavior compared with the H-free condition. A reduction in the final tolerated displacement to 1 μm is a strong indication of the combined effect of H and S atoms in weakening the GB.

Post-deformation micrographs of the beams containing the GBs of NiS1 and NiS2 bent in H-free testing condition are shown in Fig. 6(a_1)–(a_4) and (b_1)–(b_4), respectively.

The NiS1 bi-crystal beam shows a straight and sharp GB opening with a complete brittle-type fracture surface, which cut the notch area and results in the formation of a jagged-shaped cleavage pattern in the coincidence place of the GB and the notch. This is depicted in Fig. 6(a_3) and (a_4). From the figure it can also be inferred that the stress concentration in NiS1 is mostly localized at the GB and fewer slip traces can be observed in the neighboring grains. By contrast, the greater plasticity of NiS2 compared with NiS1 can be elucidated from the abundant and spread slip traces especially in the free-standing side of the beam. Although a crack nucleation can be observed in the GB (as noted in Fig. 6(b_3) and (b_4)), the notch blunting and high plasticity prevail in the deformation process. Thus, it can be deduced that in both S-doped GBs (NiS1 and NiS2), the crack is initiated from GBs rather than the notch area. However, owing to dissimilarity of the GBs, the severity of the GB opening was different. In NiS1, the GB opening reaches the notch area, whereas in NiS2, it was stopped before reaching the notch surface. The different behavior of these two GBs are more significant considering that the final displacement of the beam containing GB NiS2 was 5 μm whereas for the NiS1 sample the displacement was about 3 μm at the stage of the sharp load drop as shown in Fig. 4(b) and (c).

For both types of GBs, the co-existence of H alongside S caused the complete brittle fracture in the GB plane as shown in Fig. 7. The angled crack path in the remaining fixed side of the beams shown in Fig. 7(a_2) is an indication that the crack follows the GB. Accordingly, the sharp crack propagation in the NiS2 GB after 2 h H-charging was represented by a sudden load drop at ~1 μm displacement in the *L–D* curve as shown in Fig. 4(c). It should be noted that the used solution for H-charging of the beams with NiS2 GB contained the H recombination poison. The presence of recombination poison lead to diffusion of more H into the metal and therefore the crack nucleation and propagation happened at a very low displacement in comparison with beams tested in the poison-free solution (Fig. 4(b) and (c)).

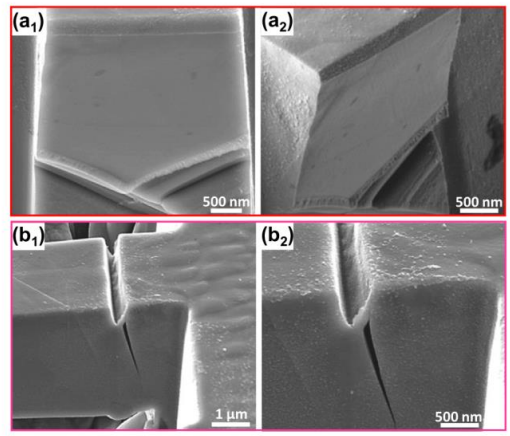

Fig. 7. Secondary electron images from the fracture surface of the beam for NiS1 (a_1) and (a_2) and the crack propagation path in NiS2 (b_1) and (b_2) bent with in situ electrochemical H-charging condition.

3.2. Computational results

3.2.1. H and S segregation to Ni GBs

The calculated GB segregation profiles of 0.25 ML of H and S impurities located in the first four GB layers as a function of distance from the GB plane are shown in Fig. 8. The results are found to be in good agreement with data available in the literature [28,29,64]. In Fig. 8, one can see that H prefers to occupy the interstitial sites within the GB layer (GB layer "0" in Fig. 3). Specifically, H prefers the "bridge" interstitial sites (shown by 1i–4i in Fig. 3). S, on the other hand, has the lowest segregation energy corresponding to its segregation to the substitutional sites (1s–4s) in the positions next to GB ("1") layer. Our results also show that there is a small energy

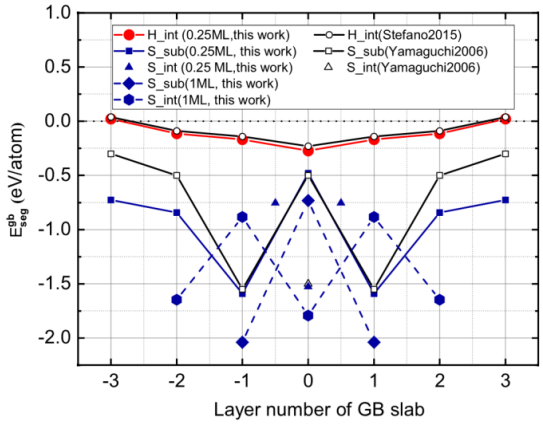

Fig. 8. H and S segregation profiles at Σ5 (012) GB in Ni compared with data from the literature [28,64]. The S segregation energies are shown for 0.25 and 1 ML coverage by using solid and dashed lines, respectively. The layer numbers corresponding to the segregation energy profiles are shown in Fig. 3.

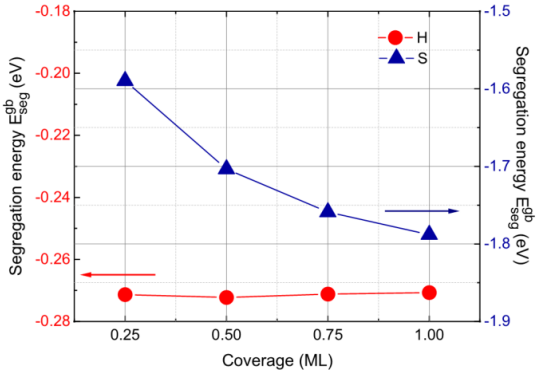

Fig. 9. Coverage effect on H and S GB segregation energies. Segregation energy per atom for coverages from 0.25 to 1 ML for interstitial H at site "0" is shown on the left *y*-axis, whereas the same for substitutional S at site "1" is shown on the right *y*-axis.

difference between the substitutional site and the "hollow" interstitial site for S (shown in Fig. 3 by *hol*. in the "0" GB layer). The calculated segregation energy of −1.59 eV/atom for S is in good agreement with previous DFT investigations [64] and experimentally measured value of −1.48 eV/atom [65]. We have also found an additional not reported earlier segregation site for S atoms located at the interstitial inter-space between layers 0 and 1 with the energy of −0.75 eV/atom.

In addition to segregation profiles, we have investigated the effect of the GB excess on the segregation energy of H and S. In Fig. 9, we show the E^{gb}_{seg} dependence on the GB excess of segregating elements ranging from 0.25 to 1 ML impurity excess for their preferred segregation site (only the minimum energy configuration for each GB excess is shown). H exhibits virtually no GB excess dependence with only a very shallow local minimum of the segregation energy at 0.5 ML GB excess, which has been observed in a number of previous DFT investigations [29,66,67]. In contrast, S atoms show an attractive interaction with approximately 0.20 eV/atom reduction in E^{gb}_{seg} when S GB excess is increased from 0.25 to 1 ML. This result is in good agreement with the theoretical results of [10,64] and the results of an experimental investigation in [68], where the observed S content at the GB was estimated to be in the range of about 1 ML. Similar interactions are present for S at other sites, as can be seen in Fig. 8 for increasing the coverage from 0.25 ML (solid lines) to 1 ML (dashed lines).

3.2.2. Interaction between segregating atoms at GB

The interaction energies between H and S atoms at the GB in Ni have been investigated by DFT calculations and the results are listed in Table 3. The interactions have been obtained for four different S and H GB excesses (0.25, 0.5, 0.75, and 1 ML) and only the minimum energy configuration for each GB excess are listed in the table. The interaction energy between the impurity atoms located at the GB E^{int} has been defined as

$$E^{\text{int}} = E^{\text{gb}}_{\text{slab}}[N-n;m;n] + (n+m-1)E^{\text{gb}}_{\text{slab}}[N;0;0] - mE^{\text{gb}}_{\text{slab}}[N;1;0] - nE^{\text{gb}}_{\text{slab}}[N-1;0,1], \quad (2)$$

where $E^{\text{gb}}_{\text{slab}}[N;m;n]$ is the total energy of the GB slab with m H atom(s) and n S atom(s) at the GB, $E^{\text{gb}}_{\text{slab}}[N;0;0]$ is the energy of a slab with no impurity atoms, $E^{\text{gb}}_{\text{slab}}[N;0;n]$ is the energy of a slab with n S atoms, and $E^{\text{gb}}_{\text{slab}}[N;m;0]$ is the energy of a slab with m H atoms. Negative values of E^{int} correspond to attractive interaction of the atoms at the GB.

Table 3
Calculated interaction energies between the segregating elements at the GB E^{int}(eV), work of separation (J/m^2), the reduction in the work of separation (%), and the ratio R calculated from Eq. (1).

GB system	GB coverage (ML)		E^{int}	W_{sep}	ΔW_{sep} (%)	R
	S	H				
Ni	–	–	–	3.508	–	0.91
Ni + H	–	0.25	–	3.414	−2.69	0.89
	–	0.50	−0.002	3.321	−5.33	0.87
	–	0.75	0.000	3.201	−8.75	0.83
	–	1.00	0.002	3.084	−12.09	0.80
Ni + S	0.25	–	–	3.187	−9.19	0.83
	0.50	–	−0.228	2.927	−16.62	0.76
	0.75	–	−0.508	2.628	−25.13	0.69
	1.00	–	−0.793	2.286	−34.88	0.60
Ni + (S & H)	0.25	0.25	0.061	3.106	−11.47	0.81
	0.50	0.25	−0.102	2.797	−20.28	0.73
	0.75	0.25	−0.296	2.524	−28.06	0.66
	1.00	0.25	−0.567	2.178	−37.93	0.57
	0.25	0.50	0.120	2.967	−15.42	0.77
	0.25	0.75	0.154	2.839	−19.08	0.74
	0.25	1.00	0.223	2.701	−22.99	0.70

The results for the interaction energy of H with itself and S with itself show the same as Fig. 9 with negligible interaction for H and significant attractive interaction for S. If we look at the interaction of H in the presence of 0.25 ML S, the interactions become repulsive. In addition, in the case of S in the presence of 0.25 ML H, the interactions are less attractive than in the case of only S interacting with itself. The results show that there are weak repulsive interactions between H and S atoms. The absolute value and the repulsive character of H–S interactions suggest that the GB segregation of S atoms should not be strongly affected by H co-segregation and vice versa. The main factor influencing S GB enrichment is the concentration of S at the GB, whereas the GB segregation of H seems to be quite inert to any GB compositional changes.

3.2.3. Kinetics of H and S segregation to Ni GB

The enrichment of the GB with S and H atoms has been calculated using the DFT segregation profiles shown in Fig. 8 (corresponding to 0.25 ML GB excess for H and 1 ML for S) and the segregation models described in [42,43]. Following the results of the previous sections, the interactions between H and S atoms have been neglected. The results on S enrichment have been obtained by concentration averaging over the interstitial and substitutional positions in the first three GB layers,

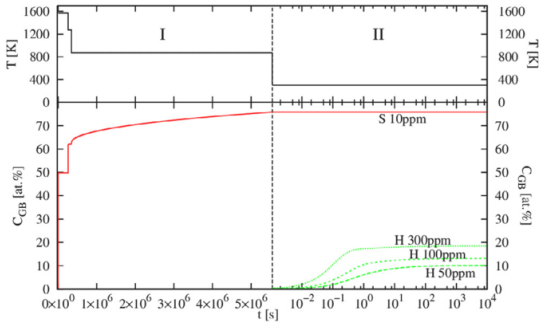

Fig. 10. Enrichment of S and H at Ni GB as a function of temperature and time. The upper panel shows temperature evolution during sample preparation and H-charging. The dashed vertical line splits the two stages of sample treatment: (I) three-step annealing and (II) H-charging. Assumed bulk concentrations of S and H in the calculations are given next to the corresponding concentration profiles. All concentrations are given in at.% and at.ppm.

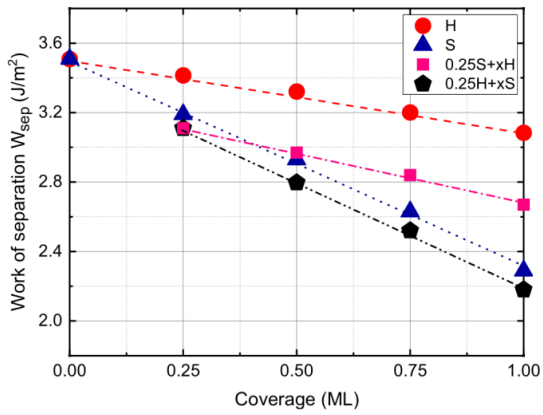

Fig. 11. Coverage change effect on the GB work of separation. The work of separation values for the coverage range of 0.25–1 ML H and S individually as well as the H–S co-segregated GB are presented.

whereas only interstitial positions have been considered in the case of H enrichment. The average grain size of 350 μm and the initial bulk amount of S equal to 5.4 wt.ppm. (10 at.ppm.) have been taken from the results of Section 2.1. The information about H content in the Ni samples during charging has been estimated to vary from 50 to 300 at.ppm. The GB width has been taken from the segregation energy profiles shown in Fig. 8 equal to 8 Å. The bulk diffusion has been taken into account via $D = D_0 \exp E_a/k_B T$ with $D_0 = 1.4 \times 10^{-4}$ m/s^2; $E_a = 2.28$ eV [69] and $D_0 = 4.47 \times 10^{-7}$ m/s^2; $E_a = 0.37$ eV [70] for S and H in Ni, respectively. The grains have been discretized into shells with a thickness of 1 μm. The information about the heat treatment history of the sample has been taken from Section 2.1 and is divided into two intervals of interest: (I) annealing; (II) H-charging.

The modeling results are shown in Fig. 10, where the left-hand side of the figure refers to the three-step annealing process (stage I) of 1300 °C for 72 h → air cooling (t' = 10 °C/s) → 1000 °C for 24 h → water cooling (t' = 100 °C/s) → 600 °C for 60 days and the right-hand side to H-charging at 300 °C for 10 h. The top panels show the evolution of temperature as a function of time. The bottom panels show the amount of S and H segregating to the GB in Ni as a function of the heat treatment time.

During the simulated three-step annealing process, S enrichment at the GB reaches 75 at.% at the end of stage I. This value is slightly below the theoretical equilibrium enrichment of S at 600 °C of 78 at.% and suggests that S has almost reached its equilibrium concentration at the GB. Note that the equilibrium S GB excess at the room temperature is about 100 at.% and the obtained amount of 75 at.% of S at the GB is a result of the instant quenching from 600 °C to room temperature at the end of stage I. The content of S remains constant during the H-charging (stage II) as diffusion is too slow at this temperature to lead to enrichment. In contrast, the amount of H diffusing into the GB after charging (stage II) varies from 10 to 18 at.%, which corresponds to the equilibrium values for the assumed H content from 50 to 300 at.ppm. in the bulk of Ni, respectively. In summary, we estimate about 75 at.% of S and 10–20 at.% of H at the GB after stages I and II of the heat treatment at the selected Σ5(210) GB.

The calculated S GB content of 75% (after stage I heat treatment in Fig. 10) can be compared with the estimated S GB concentration from the experimental WDS measurements of S segregation profiles listed in Table 1. To do so, we have converted S GB content values reported in ng/cm^2 into ML using a conversion factor reported in [68]. The theoretical prediction of S GB excess after stage I heat treatment should be close to the experimental GB S content at the GB with the highest misorientation angle, i.e., GB1 from Table 1. Indeed, our calculated value of 75% corresponding to 0.75 ML/layer on average for the given GB is in reasonably good agreement with the experimental value of 0.84 ML from the WDS experimental measurements. Here, it should be noted that GB excess of impurity atoms is highly dependent on the GB structure and the current comparison is valid under the assumption that both theoretical and experimental GB structures are close to each other.

3.2.4. GB decohesion by H and S

The effect of H and S on the W_{sep} of the Σ5(210) GB in Ni is shown in Fig. 11. Here, we show W_{sep} as a function of GB coverage x by xH, xS, 0.25S+xH, and 0.25H + xS segregating atoms. Both elements decrease W_{sep} and reduce GB resistance to decohesion. In absolute values, the effect of S on the GB decohesion is much more pronounced than that of H. In addition, variations of S GB excess (coverage) have a more pronounced effect on W_{sep} than H. However, it is the simultaneous segregation of both H and S atoms to the GB, which results in the most-pronounced GB decohesion among all considered cases. The reduction is as much as 38% (see Table 3).

As has already been mentioned in Section 2.3, reduction in W_{sep} by itself is not sufficient to describe GB embrittlement of a material. The upper estimate of G_{disl} of about 3 J/m^2 and the results presented in Fig. 11 suggest that a brittle fracture can be expected at 0.5 ML GB coverage of S atoms, whereas a significantly higher fraction of H atoms at the GB can be required to promote brittle fracture in Ni. An alternative estimate based on the calculations of the R ratio by using (1) as listed in Table 3, also demonstrates that the increase in S GB excess decreases R (reduces ductility of the GB) in a much more pronounced manner than increasing H GB excess. However, the combined effect of both H and S atoms segregating to the GB in Ni results in the most detrimental effect of all with the largest reduction in R at 1 ML of S and 0.25 ML of H GB excess. This suggests that S-rich GBs should be especially prone to HE even at low H GB concentrations. The calculated amounts of S (0.75 ML) and H (0.1–0.2 ML) at the GB after stages I and II of the heat treatment described in the previous section result in R = 0.66, which is the second lowest R value (the lowest belongs to 1 ML of S and 0.25 ML of H) with approximately 28% reduction in the work of separation (compared with pure Ni) indicating a very strong propensity towards brittle fracture of the GB.

4. Discussion

4.1. GB effect on the micro-mechanical behavior of the pure Ni bi-crystal

The presence of a GB in the microcantilever further complicates the experiment. Different grain orientations lead to activation of different slip systems to different mechanical behavior of the beam. As shown in the schematic diagram of Fig. 5(a_4), the high number of slip traces observed in the free-standing grain forced the GB to deviate from its original straight form to curved or so-called bulged shape [44] in the upper part of the beam beneath the notch. It seems that the GB acts as a sink of dislocations and all the activated slip systems end up on their pass at the GB [71]. On the other hand, the chain of micro-voids formed at the root of the blunted notch represents the commence of typical ductile fracture from the notch root. Accordingly, it appears that in the tested pure Ni bi-crystal system both the GB and notch are stress-tolerated areas with a full plastic response.

Introducing H into the system causes a distinct change in the mechanical response of the tested beams. Two clear differences between H-free and H-charged tested beams can be observed.

- First, the image contrast reveals fewer surface slip traces for the H-charged sample. A similar phenomenon has been observed by Rogne et al. on Fe26Al0.5Cr intermetallic cantilevers, where for H-charged beam the plasticity was confined to the crack area, while the slip traces spread widely far from the crack for the H-free tested beams [72]. Likewise, hydrogen assisted fatigue crack growth in pure Fe showed that the H is the main factor reducing the crack tip plasticity expansion [73]. Here it can be inferred that H confines the plasticity to the stress concentrated area at the crack tip [48,74,75]. In the H-free case, dislocations that are formed during the plastic deformation can move easily and reach the free surface of the cantilever, resulting in slip traces. In contrast, accumulation of the H atoms at the crack tip can pin the dislocations originated from the crack tip and, hence, the plastic affected zone will be confined to a small area around the crack tip. The observed phenomenon cannot be fully interpreted by the HELP mechanism. According to this mechanism, the H ingress to the system would facilitate the dislocation emission, which results in wider spreading of the plastic zone and more slip traces would reveal on the surface. It can be said that, in this case, localization of the plastic zone behind the HELP mechanism in the presence of pre-notch or pre-crack is confined to the crack tip. It is well agreed that the high hydrogen concentration at the crack tip results in a reduction of the dislocation nucleation energy. Hence, the dislocation nucleation rate at the crack tip increases. High density of dislocations alongside with the high concentration of the H, impedes the dislocation shielding and leads to their pinning at the crack tip.
- Second, in contrast to the H-free condition, the crack is initiated when the solute H was present in the material. However, the formed crack does not show fully brittle characteristics and does not follow a straight line in the same way as a brittle crack. The presence of pyramids with triangular base in the fracture surface of the created crack from the top view (Fig. 5(b_3)) is evidence that the crack propagation is accompanied by the plastic deformation. In addition, the L–D curves (Fig. 4(a)) also show not a sudden but gradual load drop during the deformation, which is also an indication of the accompaniment of the plastic deformation beside the crack propagation. The plastic growth of the crack in the H environment, which is actually a mixture of plastic blunting and cracking, has been reported a long time ago [76]. The concentration of H at the very tip of the crack lets the crack grow in a stable manner to a certain extent by micro-cleavage and then the crack growth continues by plastic deformation with the concomitant of dislocations from the crack tip up to reaching a critical H concentration for the next micro-cleavage growth [14]. The rough fracture surface in the H-charged sample can be an evidence that the H amount in the fracture process zone was not enough to induce smooth fracture surfaces. Researching on the Ni single crystal, Vehoff reports that at constant temperature, the fracture surface roughness of the sample increases as the H pressure in the testing chamber decreases [14].

Interestingly, the GB present in the bi-crystal system did not act as a crack nucleation area during the H-charging test and crack propagation stage. It seems that in this case, the GB does not act as a strong H trap. In general, unlike many body-centered cubic (BCC) metals, FCC metals have a relatively high solubility of H. In addition, knowing that the diffusivity of H is significantly lower than in BCC metals, one would expect that H enrichment is rather low in FCC metals. The study of Pu and Ooi [77] on austenitic stainless steel using a silver micro-print technique reported that the GB in FCC alloys is not an important trap for H. In the review study of McMahon on steels [78], it is suggested that H cannot induce IG cracking, unless other embrittling elements are presented in the alloy. However, some conflicting results have been published. Lassila and Birnbaum [79] reported a brittle fracture in the presence of H, but they also mentioned that as long as the H concentration is not more than the H contained in solid solution, no brittle fracture was observed. The reason behind this discrepancy in the literature can be related to the fact that the specific GB misorientation can be another factor that must be considered. It is reported that different GB misorientations tend to result in different amounts of H enrichment as well as diffusivity [80,81]. Oudriss et al. [80] suggested that the diffusible H along random GBs may be the major cause of HE. However, in our case of the random GB, the effect of H was not enough to induce complete brittle fracture. The same results were obtained by Tehranchi and Curtin [19,82]. Investigating pure Ni GB, they concluded that Ni GBs show no noticeable propensity for H to induce significant embrittlement and the presence of H creates no ductile-to-brittle transition. Another parameter that should be considered for the analysis of the results is the amount of H that is charged into the sample. The brittle type of fracture is often correlated in the literature with the amount of H dissolved in the material. Vehoff and Rothe [14] stated that the room temperature equilibrium concentration of H in the fracture process is the controlling factor for HE. The H concentration is controlled by the stress field of the plastic zone and by the type and number of traps presented in this zone. According to their results, the IG cracking may be initiated and replaced by transgranular cracking if the H activity is further enhanced by cathodic charging during the test. This point is discussed in more detail in the following sections.

4.2. GB S segregation effect on the micro-mechanical behavior of the Ni bi-crystal

S is known as a harmful impurity that if enriched at the GB, would have a detrimental effect on the mechanical properties of the GB and, consequently, the entire material. In comparison with the pure Ni beam, which shows a ductile behavior and notch blunting, the observed IG crack initiation and propagation in NiS1 and NiS2 GBs (Fig. 6) is a clear indication of the detrimental effect of the segregated S.

Several reasons have been proposed to show how the S enrichment changes the ductile behavior of a GB to a brittle IG fracture. Changes in the electronic structure that weaken the Ni–Ni bonds in the GB have been reported by Messmer et al. [83]. Yamaguchi et al. [84] suggested the large GB expansion owing to the dense S segregation can decrease the cohesive strength of the Ni GB up to one order of magnitude. It is stated that the S–S bonding formed in the GB, which is calculated to have about 24% larger distance compared with the Ni–Ni or Ni–S pairs leads to expansion in the surrounding Ni–Ni and Ni–S bonding. Consequently, this expansion in Ni–Ni or Ni–S bonds are responsible for weakening and decohesion of the GB.

The DFT results provided in Fig. 11 and Table 3 indicate that S segregation has a major effect on the decrease in W_{sep}. This increases the propensity for IG fracture if one considers the R ratio calculated in Table 3. Here, we have attempted to correlate the value of R with experimental observations of the fractured surfaces with and without H and S and concluded that the brittle fracture may occur in the materials under investigation at $R < 0.8$ (see Section 2.3 for details). Thus, the segregation of 0.5 ML of S or greater can lead to the brittle fracture.

Although both NiS1 and NiS2 show a brittle crack at the GB, the strength of the GBs against crack propagation and therefore their response to the mechanical loading presented in L–D curves were different. Three factors are proposed to explain this difference.

(a) geometry effect. The location of the GB beneath the notch and also the angle of the GB to the cantilever surface can affect the stress intensity and, hence, mechanical behavior of the system. From an experimental point of view, it is important to have a perpendicular GB plane to the specimen surface and also to the load axis. In this way, it can be assured that the activation of the slip bands, which are oriented nearly parallel to the GB plane, will be suppressed. Moreover, the tensile stress concentration will be the maximum within the GB plane assuming that the pure tensile stress dominates on the beam surface at the beginning of the test. Furthermore, the actual GB position relative to the notch should be taken into account. In order to keep the consistency of stress distribution around the GB, the notch should be milled similar in all testing beams. Small deviations in the notch position relative to the GB plane can lead to redistribution of the stresses in the plastic deformation zone. In this work (see Section 2.1), we attempted to reduce the effect of the aforementioned geometrical factors to a minimum. Comparing the notch and GB system in Fig. 6 it can be inferred that for both NiS1 and NiS2, the GB is positioned at a distance of several tens of nanometers aside from the notch root. Therefore, we assume that the geometry has a minor effect on the presented results in comparison with other parameters.

(b) structural effect. The type as well as the misorientation of the GB has been reported to have an influence on the crack initiation and propagation. High-energy random GBs are supposed to have weak resistance to the fracture whereas low-energy and low-angle GBs are more resistant [85]. In a work on Mo bi-crystals, values of fracture stress were observed to vary by a factor of six by changing the misorientation angle [86]. Thus, the different misorientation angle of the NiS1 GB compared with NiS2 can play a key role to show a nearly complete rupture of the GB to the surface. The incompatibility factor of the GB can also play a role in the observed difference. Vehoff et al. [14] showed in their experimental work on S-doped GBs that the IG cracking susceptibility increases by adding an elastic–plastic incompatibility to the bi-crystal system. Having the constant amount of S in the GBs, they investigated the effect of incompatibility by switching from a symmetrical tilt GB to an asymmetrical GB between hard and soft grains. The results confirmed that the high stress concentration associated with the incompatibility can be one of the controlling factors of the IG fracture. In our work, the NiS2 GB has a symmetric nature as an $\Sigma 5$-type GB, whereas NiS1 is an asymmetric GB. Thus, again, this factor can be another parameter to enhance embrittling potency of the NiS1 GB.

(c) chemical effect. This factor is closely related to the structural effect, as a different nature of the GB leads to a different amount of S that can segregate. In general, owing to the less-ordered arrangement of the atoms at the GB plane usually associated with an excess volume, high-angle and high-energy GBs and random GBs are deemed to be more attractive for impurity segregation [1] than low-angle, low-energy, and symmetric tilt GBs. Based on Table 1, it can be seen that high-angle GB1 with the misorientation angle of 54.2° has the largest S excess of 56.3 ng/cm^2 S, whereas the S segregation at GB2 as a low-angle GB (only 3.6°) is 20.2 ng/cm^2. The $\Sigma 5$ GB also has a low amount of S segregation (27.3 ng/cm^2). This result agrees very well with previous studies wherein it has been shown that P segregation in Fe–C alloy was three times higher for high-angle GBs rather than low-angle GBs [87]. Thus, it is reasonable to consider that the random NiS1 GB with high-angle misorientation has a higher amount of segregated S compared with the NiS2 as a symmetric $\Sigma 5$ GB. As a result, the different structure of NiS1 compared with NiS2 can be the reason for a larger S excess for NiS1 and consequently for a more-pronounced embrittlement as is confirmed from the L–D curve and fractographic investigations.

4.3. Decohesion enhancement of the GB hosting S and H

Solute H can downturn the ductility and change the fracture mode from transgranular to IG. However, H-induced IG cracking needs a number of other factors such as sufficient H content and the stress condition. Co-segregation of S alongside H to the GB can consolidate their embrittling effect [88]. Accordingly, based on the experimental results on S-doped bi-crystals, in both NiS1 and NiS2 GBs, the crack nucleates from the GB, which demonstrates that the S segregation has a weakening effect on the GB strength. Adding H to the system by cathodic charging enhanced the embrittling effect by shifting the sudden load drop to approximately 2.5 and 1 μm displacement for NiS1 and NiS2 GBs, respectively. However, it is not clear whether the co-segregation of H and S has a synergistic effect on the mechanical response of the material. For Fe it has been previously shown that the effect of S and H on the GB strength were independent and additive [89]. According to the DFT results in Fig. 11, the slope of the line related to W_{sep} for S (blue triangle line) is the same as for the case with 0.25 ML H present (black pentagon line). A similar trend can be observed for the effect of H on W_{sep} with and without 0.25 ML S (red circle and pink square lines, respectively). This result confirms the independent embrittling effect of the H and S.

On the other hand, it could be possible that the presence of S enhances the H ingress into the material owing to the detrimental effect of this impurity on the H recombination reaction [90,91], a fact that is not yet considered in DFT calculations. Preventing the recombination reaction by S can increase the local adsorption and enrichment of H at the metal GBs. Likewise, this phenomenon is reported for the Sb and Sn segregated GBs in Ni, which are also recombination poisons [12]. It is suggested that H preferentially ingressed into the Ni specimens in the proximity of GB intersections with the free surface owing to the presence of Sb and Sn, which as H recombination poisons stimulate the absorption of H by the metal. Co-segregation of S and H has also been investigated by the molecular orbital model [92]. According to this work, forming a network of S–S bonds within the GB leads to an increase in the shear stress and simultaneously reduces the cohesive strength of the GB. However, they suggested that by forming a network of bonds with incorporation of a third element such as H, the shear strength will increase while, the cohesive strength of the GB will not be affected. However, this hypothesis is not fully in line with our results. As seen in Figs. 6 and 7, the shear bands are activated in all H-free conditions, even with the presence of a high amount of S in the GBs. In the case of S-doped NiS1 GB, which cracked in a fully brittle manner, the slip lines are still observable especially on the free-standing grain, which is more favorable for dislocation movements. Thus, it is hard to see any enhancement in shear stress for S-doped specimens. In contrast, adding H to the system was more effective at hindering the dislocation movements and fewer slip lines revealed on the surface even in the pure Ni sample. Hydrogen can pin the dislocations and, hence, increase the dislocation as depicted in Fig. 12.

According to Table 3, adding 0.25 ML of S decreased the work of separation by 9.19%, whereas 2.69% reduction has been calculated for the same amount of H at the GB. The same behavior of greater effect of S is also observed for co-segregation of the S and H in Fig. 11, by considering the slopes for increasing H and S, respectively. The steeper slope for increasing S shows the greater effect of S on GB decohesion.

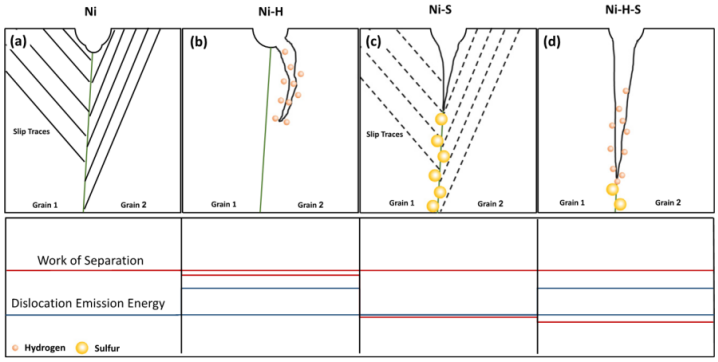

Fig. 12. Schematic representation of the crack propagation for pure Ni, H-charged, S-doped, and Ni–S–H conditions with the corresponding work of separation and dislocation emission energy level.

The GB embrittling effect of H, S, and H + S can be interpreted by considering the competition between the brittle fracture and the dislocation emission, which is schematically shown in Fig. 12. In pure Ni, the energy needed for emitting dislocations is lower than the work of separation for the GB, therefore we observe activation of slip planes near the GB (Fig. 12(a)). Adding H to the system enhances the required energy for dislocation emission along with decreasing W_{sep}. The associated energy changes in the system are still not sufficient to induce IG cracking, although H already confines the plastic zone to the notch area (Fig. 12(b)). In the case of S segregation to the Ni GB, the work of separation decreases and becomes virtually equivalent to the value of the dislocation emission energy, which results in simultaneous GB decohesion and activation of slip planes near the GB (Fig. 12(c)). Co-segregation of H and S to the GB decreases the work of separation leading to IG cracking and possibly leads to an increase in the dislocation emission energy owing to dislocation pinning by H near the GB (Fig. 12(d)). It can be said that S is more influential on the decohesion reduction, whereas H is more effective on increasing the shear stress for plastic deformation. Subsequently, the co-segregation of S + H can have a double side brittleness effect on both decohesion and shear stress.

4.4. H concentration enhancement

As mentioned previously, the H concentration is one of the main parameters controlling the mechanical response of the material. Therefore, to investigate the effect of H concentration enhancement on the GB embrittlement, 0.002 M $Na_2S_2O_4$ as H recombination poison was added to the charging glycerol-based solution for testing beams containing NiS2 GB. Owing to the poison, the adsorbed and absorbed H concentration in the material increases [93].

Comparing *L–D* curves in Fig. 4 for NiS1 and NiS2 GBs in H-free condition, it can be inferred that the NiS2 GB shows more ductility compared with NiS1. However, for 2 h of H charging, the presence of poison for bending the beam containing NiS2 GB causes more ductility loss in comparison with NiS1, which is tested without any poison. As discussed in Section 4.2, the NiS2 GB possesses lower misorientation angle and probably a lower amount of S compared with NiS1 GB. Thus, NiS2 is less prone to cracking. However, the higher content of H obtained by adding poison into the solution, can overcome the structural and chemical effect in the way that the NiS2 GB fails easier and shows enhanced embrittlement compared with NiS1 with the same H-charging time but no poison. By accumulation of a high amounts of H, the GB decohesion takes place according to the HEDE mechanism which leads to the observed GB opening. In accordance with our results, it is reported that by increasing the cathodic potential, which would enhance the H concentration in the Ni GB, the critical S concentration to cause 50% IG fracture decreases [8,20]. By applying −0.72 V (SCE) cathodic potential, the critical S segregation concentration drops to about ~2 at.%, whereas with a potential of −0.3 V (SCE) the critical S segregation concentration was 6.5 at.%. In addition, Lassia and Birnbaum [79] reported a change from ductile fracture to a mixed brittle ductile and complete IG fracture by increasing the H content from 0 at.ppm. to 60 and 600 at.ppm., respectively, for a specimen with a S concentration of 0.1 S/Ni.

Low diffusivity coupled with high solubility in Ni results in a high H concentration gradient near to the surface. This gradient may result in some structural effects close to the sample surface and accordingly a considerable change in the mechanical properties of the material. Changes in the flow stress of the H-charged Ni samples is one of these effects. As shown in Fig. 13, continuing the in situ testing in the poison-containing solution revealed a hardening effect for the beams tested after 3 h of charging. Although the sudden load drop for both 3 h and 2 h charged samples happens in the same displacement, for the 3 h charging condition the beam shows about 20% increase in the maximum tolerated load. After 3 h of charging in poisoned solution, in situ charging was stopped, the samples were taken out of the solution, rinsed with distilled water and later with ethanol, which was followed by storing them in a desiccator. Then, the beams were bent after 2, 4, and 17 h. For 2 h of being in air (H-charged 3 h + air 2 h), the same *L–D* curve as 3 h in situ charging is achieved. Giving further time to the sample in a H-free environment turns over the ductility of the tested beam up to 50% after 17 h of being in air, whereas the observed hardening effect was persistent in all *L–D* curves obtained after 3 h of charging.

The observed increase in the maximum tolerated force can be interpreted as the hardening effect caused by H-dislocation interaction. Several researchers have reported the hardening effect during H-charging in both BCC [94] and FCC materials [71]. As an example, Kimura and Birnbaum [63] observed the hardening effect when they charged the Ni samples in a solution containing H recombination poison at a current density of 0.8 mA/cm^2. Their reported current density is in a comparable range to that used in our experiment. However, there is a significant difference in the obtained results. The hardening effect reported in their work was reversible and the flow stress turned back to that recorded in the absence of H, when the cathodic potential was removed. In contrast, the maximum tolerated load enhancement in the *L–D* curves shown in Fig. 13 was persistent and did not show any decrease even after 17 h of keeping the sample in air. Hence, it seems that there are other factors playing a role in the irreversible hardening effect observed when the H-charging was stopped.

The high H concentration gradient and subsequently stress gradient at the metal sub-surface can lead to formation of the localized hydride or H clusters at the dislocation cores [95,96]. It is reported that these phases can lock the Frank–Read and other dislocation sources.

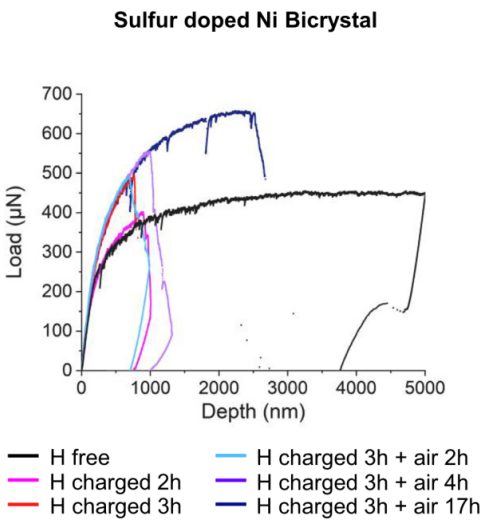

Fig. 13. Load–displacement curves of the S-doped (GB NiS2 in Table 2) bi-crystal beams tested with H-free, in situ electrochemical H-charging, and post-charging in air conditions. The H-charging electrolyte contained 0.002 M $Na_2S_2O_4$ as the H recombination poison.

Locking of the local dislocations formed at the dislocation core would lead to large dislocation pile ups resulting in surface hardening [97]. In addition, Kimura and Birnbaum showed that the hardening effect caused by Ni hydride formation is irreversible even after aging for several hours [63]. Hydride is a brittle phase and acts as a barrier to dislocation motion. Despite the thermodynamically unstable nature of Ni–H at room temperature, it is documented that if high activity of H atoms is present, hydride formation would be possible [98]. During the out gassing, although the hydride layer reverts to Ni owing to its unstable nature at room temperature [63,99], the remaining high surface dislocation density causes the residual increase in the flow curve [63].

5. Conclusions

The current work has focused on a combined experimental and theoretical investigation of the effect of S and H segregation on the mechanical properties of selected GBs. In situ micro-cantilever bending tests have been utilized to investigate the mechanical response of the GBs, whereas DFT calculations have been used to study the interaction of S and H with the GB at the atomic level. Cantilever bending tests in pure Ni samples without S segregation result in a ductile behavior accompanied by slip traces on the surface. While testing pure Ni in H-charged condition, the crack is initiated from the notch area and fewer activated slip traces are observed. The observed difference is associated with the impeding effect of H on the dislocation motion leading to the and localized plasticity at the crack tip. It is showed that the crack formed in the H-charged pure Ni beam is neither IG nor purely brittle. In this case, H concentration at the GB does not reach the critical amount to cause the IG fracture atomic associated with the HEDE mechanism. Segregation of S to GB leads to the IG cracking during the bending test. The crack reveals brittle type of fracture and propagates through the GB. Hydrogen-charging makes the IG fracture even more prominent and causes a sooner sudden drop in *L–D* curves compared with H-free conditions. Based on the DFT results, it is shown that the GB cohesion is much more reduced by S enrichment in comparison with H enrichment. Even though the co-segregation of S and H substantially reduces the cohesion of the selected GB, no interaction between S and H effects is obtained by DFT calculations.

CRediT authorship contribution statement

Tarlan Hajilou: Conceptualization, Methodology, Investigation, Writing - original draft. **Iman Taji:** Methodology, Visualization, Writing - original draft. **Frederic Christien:** Methodology, Investigation, Resources, Writing - review & editing. **Shuang He:** Methodology, DFT simulations, Writing - original draft. **Daniel Scheiber:** Methodology, Kinetic simulations, Writing - original draft. **Werner Ecker:** Conceptualization, Writing - review. **Reinhard Pippan:** Conceptualization, Supervision. **Vsevolod I. Razumovskiy:** Methodology, Supervision, Writing - review & editing. **Afrooz Barnoush:** Conceptualization, Methodology, Supervision, Funding acquisition.

Data availability

The raw/processed data required to reproduce these findings cannot be shared at this time as the data also forms part of an ongoing study.

Acknowledgments

The authors gratefully acknowledge the financial support under the scope of the COMET program within the K2 Center "Integrated Computational Material, Process and Product Engineering (IC-MPPE), Astria" (Project No. 859480). This program is supported by Equinor, Norway and Voestalpine BÖHLER Edelstahl GmbH & Co KG, the Austrian Federal Ministries for Climate Action, Environment, Energy, Mobility, Innovation and Technology (BMK) and for Digital and Economic Affairs (BMDW), represented by the Austrian Research Funding Association (FFG), and the federal states of Styria, Upper Austria, and Tyrol. The computational results presented have been obtained using the Vienna Scientific Cluster (VSC). The Research Council of Norway is acknowledged for the support to the Norwegian Micro- and Nano-Fabrication Facility, NorFab, Norway (Project No. 245963/F50). The authors express their gratitude to Dr. Mohammad Zamanzade for his constructive comments and discussion. Sondre Fossheim is also acknowledged for his contribution to producing the micro-samples.

References

[1] P. Lejček, Grain Boundary Segregation in Metals, Springer Berlin Heidelberg, Berlin, 2010.

[2] P. Lejček, M. Šob, V. Paidar, Interfacial segregation and grain boundary embrittlement: An overview and critical assessment of experimental data and calculated results, Prog. Mater. Sci. 87 (2017) 83–139, http://dx.doi.org/10.1016/j.pmatsci.2016.11.001, URL http://www.sciencedirect.com/science/article/pii/S0079642516300755.

[3] J.R. Rice, J.-S. Wang, Embrittlement of interfaces by solute segregation, Mater. Sci. Eng. A 107 (1989) 23–40, http://dx.doi.org/10.1016/0921-5093(89)90372-9, URL http://www.sciencedirect.com/science/article/pii/0921509389903729.

[4] S. Lynch, A review of underlying reasons for intergranular cracking for a variety of failure modes and materials and examples of case histories, Eng. Fail. Anal. 100 (2019) 329–350, http://dx.doi.org/10.1016/j.engfailanal.2019.02.027.

[5] S. Mahalingam, P.E.J. Flewitt, J.F. Knott, The ductile–brittle transition for nominally pure polycrystalline nickel, Mater. Sci. Eng.: A 564 (2013) 342–350, http://dx.doi.org/10.1016/j.msea.2012.11.106, URL http://www.sciencedirect.com/science/article/pii/S0921509312016589.

[6] M. Lozinsky, G. Volkogon, N. Pertsovsky, Investigation of the influence of zirconium additions on the ductility and deformation structure of nickel over a wide temperature range, Russ. Metall. 5 (1967) 65–72.

[7] A. Larere, M. Guttmann, P. Dumoulin, C. Roques-Carmes, Auger electron spectroscopy study of the kinetics of intergranular and surface segregations in nickel during annealing, Acta Metall. 30 (3) (1982) 685–693.

[8] S.M. Bruemmer, R.H. Jones, M.T. Thomas, D.R. Baer, Influence of sulfur, phosphorus, and antimony segregation on the intergranular hydrogen embrittlement of nickel, Metall. Trans. A 14 (1) (1983) 223–232, http://dx.doi.org/10.1007/bf02651619.

[9] W.T. Geng, A.J. Freeman, R. Wu, C.B. Geller, J.E. Raynolds, Embrittling and strengthening effects of hydrogen, boron, and phosphorus on a Σ5 nickel grain boundary, Phys. Rev. B 60 (1999) 7149–7155, http://dx.doi.org/10.1103/PhysRevB.60.7149, URL https://link.aps.org/doi/10.1103/PhysRevB.60.7149.

[10] V. Razumovskiy, A. Lozovoi, I. Razumovskii, First-principles-aided design of a new Ni-base superalloy: Influence of transition metal alloying elements on grain boundary and bulk cohesion, Acta Mater. 82 (Supplement C) (2015) 369–377, http://dx.doi.org/10.1016/j.actamat.2014.08.047, URL http://www.sciencedirect.com/science/article/pii/S1359645414006612.

[11] R.H. Jones, S.M. Bruemmer, M.T. Thomas, D.R. Baer, Hydrogen pressure dependence of the fracture mode transition in nickel, Metall. Trans. A 14 (8) (1983) 1729–1736, http://dx.doi.org/10.1007/bf02654401.

[12] R.M. Latanision, H. Opperhauser, The intergranular embrittlement of nickel by hydrogen: The effect of grain boundary segregation, Metall. Trans. 5 (2) (1974) 483–492, http://dx.doi.org/10.1007/BF02644118.

[13] K.M. Bertsch, S. Wang, A. Nagao, I.M. Robertson, Hydrogen-induced compatibility constraints across grain boundaries drive intergranular failure of ni, Mater. Sci. Eng. A 760 (2019) 58–67, http://dx.doi.org/10.1016/j.msea.2019.05.036, URL http://www.sciencedirect.com/science/article/pii/S092150931930658.

[14] H. Vehoff, W. Rothe, Gaseous hydrogen embrittlement in fesi-and ni-single crystals, in: Perspectives in Hydrogen in Metals, Elsevier, 1986, pp. 647–659.

[15] M.B. Djukic, G.M. Bakic, V. Sijacki Zeravcic, A. Sedmak, B. Rajicic, The synergistic action and interplay of hydrogen embrittlement mechanisms in steels and iron: Localized plasticity and decohesion, Eng. Fract. Mech. 216 (2019) 106528, http://dx.doi.org/10.1016/j.engfracmech.2019.106528.

[16] M.L. Martin, M. Dadfarnia, A. Nagao, S. Wang, P. Sofronis, Enumeration of the hydrogen-enhanced localized plasticity mechanism for hydrogen embrittlement in structural materials, Acta Mater. (2018) http://dx.doi.org/10.1016/j.actamat.2018.12.014.

[17] R. Kirchheim, Solid solution softening and hardening by mobile solute atoms with special focus on hydrogen, Scr. Mater. 67 (9) (2012) 767–770, http://dx.doi.org/10.1016/j.scriptamat.2012.07.022.

[18] M.L. Martin, B.P. Somerday, R.O. Ritchie, P. Sofronis, I.M. Robertson, Hydrogen-induced intergranular failure in nickel revisited, Acta Mater. 60 (6) (2012) 2739–2745, http://dx.doi.org/10.1016/j.actamat.2012.01.040.

[19] A. Metsue, A. Oudriss, X. Feaugas, Hydrogen solubility and vacancy concentration in nickel single crystals at thermal equilibrium: New insights from statistical mechanics and *ab initio* calculations, J. Alloys Compd. 656 (2016) 555–567, http://dx.doi.org/10.1016/j.jallcom.2015.09.252, URL http://www.sciencedirect.com/science/article/pii/S0925838815312299.

[20] J.K. Heuer, P.R. Okamoto, N.Q. Lam, J.F. Stubbins, Relationship between segregation-induced intergranular fracture and melting in the nickel sulfur system, Appl. Phys. Lett. 76 (23) (2000) 3403–3405, http://dx.doi.org/10.1063/1.126660, URL arXiv:https://doi.org/10.1063/1.126660.

[21] H. Vehoff, C. Laird, D. Duquette, The effects of hydrogen and segregation on fatigue crack nucleation at defined grain boundaries in nickel bicrystals, Acta Metall. 35 (12) (1987) 2877–2886, http://dx.doi.org/10.1016/0001-6160(87)90286-0, URL http://www.sciencedirect.com/science/article/pii/0001616087902860.

[22] D. Di Maio, S. Roberts, Measuring fracture toughness of coatings using focused-ion-beam-machined microbeams, J. Mater. Res. 20 (2) (2005) 299–302, http://dx.doi.org/10.1557/JMR.2005.0048.

[23] J. Ast, M. Ghidelli, K. Durst, M. Gken, M. Sebastiani, A.M. Korsunsky, A review of experimental approaches to fracture toughness evaluation at the micro-scale, Mater. Des. 173 (2019) 107762, http://dx.doi.org/10.1016/j.matdes.2019.107762, URL http://www.sciencedirect.com/science/article/pii/S0264127519301996.

[24] H. Dugdale, D.E.J. Armstrong, E. Tarleton, S.G. Roberts, S. Lozano-Perez, How oxidized grain boundaries fail, Acta Mater. 61 (13) (2013) 4707–4713, http://dx.doi.org/10.1016/j.actamat.2013.05.012, URL http://www.sciencedirect.com/science/article/pii/S1359645413003800.

[25] A. Stratulat, D.E.J. Armstrong, S.G. Roberts, Micro-mechanical measurement of fracture behaviour of individual grain boundaries in ni alloy 600 exposed to a pressurized water reactor environment, Corros. Sci. 104 (2016) 9–16, http://dx.doi.org/10.1016/j.corsci.2015.10.019, URL http://www.sciencedirect.com/science/article/pii/S0010938X15301189.

[26] M. Yamaguchi, M. Shiga, H. Kaburaki, Energetics of segregation and embrittling potency for non-transition elements in the ni Σ 5 (012) symmetrical tilt grain boundary: a first-principles study, J. Phys.: Condens. Matter 16 (23) (2004) 3933, http://dx.doi.org/10.1088/0953-8984/16/23/013, URL http://stacks.iop.org/0953-8984/16/i=23/a=013.

[27] M. Yamaguchi, M. Shiga, H. Kaburaki, First-principles study on segregation energy and embrittling potency of hydrogen in ni Σ 5(012) tilt grain boundary, J. Phys. Soc. Japan 73 (2) (2004) 441–449, http://dx.doi.org/10.1143/JPSJ.73.441.

[28] D.D. Stefano, M. Mrovec, C. Elssser, First-principles investigation of hydrogen trapping and diffusion at grain boundaries in nickel, Acta Mater. 98 (2015) 306–312, http://dx.doi.org/10.1016/j.actamat.2015.07.031, URL http://www.sciencedirect.com/science/article/pii/S1359645415005029.

[29] S. He, W. Ecker, R. Pippan, V.I. Razumovskiy, Hydrogen-enhanced decohesion mechanism of the special Σ5(012)[100] grain boundary in ni with mo and c solutes, Comput. Mater. Sci. 167 (2019) 100–110, http://dx.doi.org/10.1016/j.commatsci.2019.05.029, URL http://www.sciencedirect.com/science/article/pii/S0927025619303076.

[30] T. Depover, K. Verbeken, Evaluation of the effect of v4c3 precipitates on the hydrogen induced mechanical degradation in fe-c-v alloys, Mater. Sci. Eng. A 675 (2016) 299–313, http://dx.doi.org/10.1016/j.msea.2016.08.053, URL http://www.sciencedirect.com/science/article/pii/S0921509316309662.

[31] T. Depover, K. Verbeken, Hydrogen trapping and hydrogen induced mechanical degradation in lab cast fe-c-cr alloys, Mater. Sci. Eng. A 669 (2016) 134–149, http://dx.doi.org/10.1016/j.msea.2016.05.018, URL http://www.sciencedirect.com/science/article/pii/S0921509316305111.

[32] B. He, W. Xiao, W. Hao, Z. Tian, First-principles investigation into the effect of cr on the segregation of multi-H at the Fe Σ 3 (111) grain boundary, J. Nucl. Mater. 441 (1) (2013) 301–305, http://dx.doi.org/10.1016/j.jnucmat.2013.06.015, URL http://www.sciencedirect.com/science/article/pii/S0022311513008386.

[33] M. Yuasa, M. Hakamada, Y. Chino, M. Mabuchi, First-principles study of hydrogen-induced embrittlement in Fe Grain Boundary with Cr segregation, ISIJ Int. 55 (5) (2015) 1131–1134, http://dx.doi.org/10.2355/isijinternational.55.1131, URL https://www.jstage.jst.go.jp/article/isijinternational/55/5/55_1131/_pdf/-char/ja.

[34] D.A. Aksyonov, T. Hickel, J. Neugebauer, A.G. Lipnitskii, The impact of carbon and oxygen in alpha-titanium:ab initiostudy of solution enthalpies and grain boundary segregation, J. Phys.: Condens. Matter. 28 (38) (2016) 385001, http://dx.doi.org/10.1088/0953-8984/28/38/385001.

[35] D. Scheiber, L. Romaner, R. Pippan, P. Puschnig, Impact of solute-solute interactions on grain boundary segregation and cohesion in molybdenum, Phys. Rev. Mater. 2 (2018) 093609, http://dx.doi.org/10.1103/PhysRevMaterials.2.093609, URL https://link.aps.org/doi/10.1103/PhysRevMaterials.2.093609.

[36] M. Yamaguchi, M. Shiga, H. Kaburaki, Grain boundary decohesion by impurity segregation in a nickel-sulfur system, Science 307 (5708) (2005) 393–397, http://dx.doi.org/10.1126/science.1104624, arXiv:https://science.sciencemag.org/content/307/5708/393.full.pdf, URL https://science.sciencemag.org/content/307/5708/393.

[37] M. Yamaguchi, M. Shiga, H. Kaburaki, Response to comment on "grain boundary decohesion by impurity segregation in a nickel-sulfur system", Science 309 (5741) (2005) 1677, http://dx.doi.org/10.1126/science.1112218, arXiv:https://science.sciencemag.org/content/309/5741/1677.4.full.pdf, URL https://science.sciencemag.org/content/309/5741/1677.4.

[38] W.T. Geng, J.-S. Wang, G.B. Olson, Comment on "grain boundary decohesion by impurity segregation in a nickel-sulfur system", Science 309 (5741) (2005) 1677, http://dx.doi.org/10.1126/science.1112072, arXiv:https://science.sciencemag.org/content/309/5741/1677.3.full.pdf, URL https://science.sciencemag.org/content/309/5741/1677.3.

[39] G. Schusteritsch, E. Kaxiras, Sulfur-induced embrittlement of nickel: a first-principles study, Modelling Simul. Mater. Sci. Eng. 20 (6) (2012) 065007, http://dx.doi.org/10.1088/0965-0393/20/6/065007.

[40] J.R. Rice, R. Thomson, Ductile versus brittle behaviour of crystals, Phil. Mag. A 29 (1) (1974) 73–97, http://dx.doi.org/10.1080/14786437408213555.

[41] D. McLean, Grain Boundaries in Metals, Clarendon Press, Oxford, 1957.

[42] D. Scheiber, L. Romaner, F. Fischer, J. Svoboda, Kinetics of grain boundary segregation in multicomponent systems – The example of a Mo-C-B-O system, Scr. Mater. 150 (2018) 110–114, http://dx.doi.org/10.1016/j.scriptamat.2018.03.011, URL http://linkinghub.elsevier.com/retrieve/pii/S1359646218301635.

[43] D. Scheiber, T. Jechtl, J. Svoboda, F. Fischer, L. Romaner, On solute depletion zones along grain boundaries during segregation, Acta Mater. (2019) http://dx.doi.org/10.1016/j.actamat.2019.10.040, URL http://www.sciencedirect.com/science/article/pii/S1359645419307025.

[44] N. Kheradmand, H. Vehoff, A. Barnoush, An insight into the role of the grain boundary in plastic deformation by means of a bicrystalline pillar compression test and atomistic simulation, Acta Mater. 61 (19) (2013) 7454–7465.

[45] F. Christien, P. Risch, Cross-sectional measurement of grain boundary segregation using wds, Ultramicroscopy 170 (2016) 107–112.

[46] A. Barnoush, H. Vehoff, Recent developments in the study of hydrogen embrittlement: Hydrogen effect on dislocation nucleation, Acta Mater. 58 (16) (2010) 5274–5285.

[47] A. Barnoush, H. Vehoff, In situ electrochemical nanoindentation: A technique for local examination of hydrogen embrittlement, Corros. Sci. 50 (1) (2008) 259–267, http://dx.doi.org/10.1016/j.corsci.2007.05.026, URL http://www.sciencedirect.com/science/article/pii/S0010938X07001655.

[48] T. Hajilou, Y. Deng, B.R. Rogne, N. Kheradmand, A. Barnoush, In situ electrochemical microcantilever bending test: A new insight into hydrogen enhanced cracking, Scr. Mater. 132 (2017) 17–21, http://dx.doi.org/10.1016/j.scriptamat.2017.01.019, URL http://www.sciencedirect.com/science/article/pii/S1359646217300295.

[49] T. Hajilou, M.S. Hope, A.H. Zavieh, N. Kheradmand, R. Johnsen, A. Barnoush, In situ small-scale hydrogen embrittlement testing made easy: An electrolyte for preserving surface integrity at nano-scale during hydrogen charging, Int. J. Hydrog. Energy 43 (27) (2018) 12516–12529, http://dx.doi.org/10.1016/j.ijhydene.2018.04.168, URL http://www.sciencedirect.com/science/article/pii/S0360319918313570.

[50] P.E. Blöchl, Projector augmented-wave method, Phys. Rev. B 50 (24) (1994) 17953, http://dx.doi.org/10.1103/PhysRevB.50.17953, URL https://link.aps.org/doi/10.1103/PhysRevB.50.17953.

[51] G. Kresse, D. Joubert, From ultrasoft pseudopotentials to the projector augmented-wave method, Phys. Rev. B 59 (3) (1999) 1758, http://dx.doi.org/10.1103/PhysRevB.59.1758, URL https://link.aps.org/doi/10.1103/PhysRevB.59.1758.

[52] G. Kresse, J. Hafner, *Ab initio* molecular dynamics for open-shell transition metals, Phys. Rev. B 48 (1993) 13115–13118, http://dx.doi.org/10.1103/PhysRevB.48.13115, URL http://link.aps.org/doi/10.1103/PhysRevB.48.13115.

[53] G. Kresse, J. Furthmüller, Efficiency of ab-initio total energy calculations for metals and semiconductors using a plane-wave basis set, Comput. Mater. Sci. 6 (1) (1996) 15–50, http://dx.doi.org/10.1016/0927-0256(96)00008-0, URL http://www.sciencedirect.com/science/article/pii/0927025696000080.

[54] J.P. Perdew, K. Burke, M. Ernzerhof, Generalized gradient approximation made simple, Phys. Rev. Lett. 77 (1996) 3865–3868, http://dx.doi.org/10.1103/PhysRevLett.77.3865, URL https://link.aps.org/doi/10.1103/PhysRevLett.77.3865.

[55] H.J. Monkhorst, J.D. Pack, Special points for brillouin-zone integrations, Phys. Rev. B 13 (1976) 5188–5192, http://dx.doi.org/10.1103/PhysRevB.13.5188, URL https://link.aps.org/doi/10.1103/PhysRevB.13.5188.

[56] D. Kandaskalov, D. Monceau, C. Mijoule, D. Conntable, First-principles study of sulfur multi-absorption in nickel and its segregation to the ni(100) and ni(111) surfaces, Surf. Sci. 617 (2013) 15–21, http://dx.doi.org/10.1016/j.susc.2013.06.019, URL http://www.sciencedirect.com/science/article/pii/S003960281300191X.

[57] D. Connétable, É. Andrieu, D. Monceau, First-principles nickel database: Energetics of impurities and defects, Comput. Mater. Sci. 101 (2015) 77–87, http://dx.doi.org/10.1016/j.commatsci.2015.01.017.

[58] R. Nazarov, T. Hickel, J. Neugebauer, Ab initio study of H-vacancy interactions in fcc metals: Implications for the formation of superabundant vacancies, Phys. Rev. B 89 (14) (2014) 144108, http://dx.doi.org/10.1103/PhysRevB.89.144108, URL https://link.aps.org/doi/10.1103/PhysRevB.89.144108.

[59] L. Wang, H. Bei, T. Li, Y. Gao, E. George, T. Nieh, Determining the activation energies and slip systems for dislocation nucleation in body-centered cubic mo and face-centered cubic ni single crystals, Scr. Mater. 65 (3) (2011) 179–182, http://dx.doi.org/10.1016/j.scriptamat.2011.03.036, URL http://www.sciencedirect.com/science/article/pii/S1359646211001680.

[60] A.P. Sutton, R.W. Balluffi, A. Sutton, Interfaces in Crystalline Materials, Clarendon Press Oxford, 1995.

[61] D. Scheiber, R. Pippan, P. Puschnig, L. Romaner, Ab initio calculations of grain boundaries in bcc metals, Modelling Simul. Mater. Sci. Eng. 24 (3) (2016) 035013, http://dx.doi.org/10.1088/0965-0393/24/3/035013.

[62] A. Pineau, A. Benzerga, T. Pardoen, Failure of metals i: Brittle and ductile fracture, Acta Mater. 107 (2016) 424–483, http://dx.doi.org/10.1016/j.actamat.2015.12.034, URL http://www.sciencedirect.com/science/article/pii/S1359645415301403.

[63] A. Kimura, H. Birnbaum, The effects of cathodically charged hydrogen on the flow stress of nickel and nickel-carbon alloys, Acta Metall. 35 (5) (1987) 1077–1088.

[64] M. Yamaguchi, M. Shiga, H. Kaburaki, Grain boundary decohesion by sulfur segregation in ferromagnetic iron and nickel - a first-principles study, Mater. Trans. 47 (11) (2006) 2682–2689, http://dx.doi.org/10.2320/matertrans.47.2682.

[65] A. Winkler, K.D. Rendulic, Measurements of bulk concentration in the ppm-Region by means of surface segregation: The system sulphur-nickel, in: M. Grasserbauer, M.K. Zacherl (Eds.), Zehntes Kolloquium ÜBer Metallkundliche Analyse, Springer Vienna, Vienna, 1981, pp. 321–327.

[66] A. Alvaro, I.T. Jensen, N. Kheradmand, O. Lvvik, V. Olden, Hydrogen embrittlement in nickel, visited by first principles modeling, cohesive zone simulation and nanomechanical testing, Int. J. Hydrog. Energy 40 (47) (2015) 16892–16900, http://dx.doi.org/10.1016/j.ijhydene.2015.06.069, Special issue on 1st International Conference on Hydrogen Storage, Embrittlement and Applications (Hy-SEA 2014), 26-30 October 2014, Rio de Janeiro, Brazil. URL http://www.sciencedirect.com/science/article/pii/S0360319915015542.

[67] I.J.T. Jensen, V. Olden, O.M. Løvvik, Decohesion energy of Σ5(012)grain boundaries in ni as function of hydrogen content, Metall. Mater. Trans. A 50 (1) (2019) 451–456, http://dx.doi.org/10.1007/s11661-018-4982-8.

[68] M. Allart, F. Christien, R.L. Gall, P. Nowakowski, C. Grovenor, A multi-technique investigation of sulfur grain boundary segregation in nickel, Scr. Mater. 68 (10) (2013) 793–796, http://dx.doi.org/10.1016/j.scriptamat.2013.01.028, URL http://www.sciencedirect.com/science/article/pii/S135964621300050X.

[69] H. Mehrer, N. Stolica, Diffusion in solid metals and alloys, in: Landolt-Börnstein Numerical Data and Functional Relationships in Science and Technology, Group III, in: Landolt-Börnstein - Group III Condensed Matter, vol. 26, Springer-Verlag, Berlin/Heidelberg, 1990, http://dx.doi.org/10.1007/b37801, URL http://materials.springer.com/bp/docs/978-3-540-46109-8.

[70] M. Hill, E. Johnson, The diffusivity of hydrogen in nickel, Acta Metall. 3 (6) (1955) 566–571, http://dx.doi.org/10.1016/0001-6160(55)90116-4, URL https://www.sciencedirect.com/science/article/pii/0001616055901164.

[71] J. Kacher, B.P. Eftink, B. Cui, I.M. Robertson, Dislocation interactions with grain boundaries, Curr. Opin. Solid State Mater. Sci. 18 (4) (2014) 227–243, http://dx.doi.org/10.1016/j.cossms.2014.05.004, URL http://www.sciencedirect.com/science/article/pii/S1359028614000217http://ac.els-cdn.com/S1359028614000217/1-s2.0-S1359028614000217-main.pdf?_tid=2ce37376-bdfc-11e5-984e-00000aacb362&acdnat=1453132828_ba5498edb0319e0341917ce59a77bac1.

[72] B.R.S. Rogne, N. Kheradmand, Y. Deng, A. Barnoush, In situ micromechanical testing in environmental scanning electron microscope: A new insight into hydrogen-assisted cracking, Acta Mater. 144 (2018) 257–268.

[73] Y. Ogawa, D. Birenis, H. Matsunaga, A. Thgersen, Prytz, O. Takakuwa, J. Yamabe, Multi-scale observation of hydrogen-induced, localized plastic deformation in fatigue-crack propagation in a pure iron, Scr. Mater. 140 (2017) 13–17, http://dx.doi.org/10.1016/j.scriptamat.2017.06.037.

[74] Y. Deng, A. Barnoush, Hydrogen embrittlement revealed via novel in situ fracture experiments using notched micro-cantilever specimens, Acta Mater. 142 (2018) 236–247, http://dx.doi.org/10.1016/j.actamat.2017.09.057, URL http://www.sciencedirect.com/science/article/pii/S1359645417308273.

[75] D. Wan, Y. Deng, J.I.H. Meling, A. Alvaro, A. Barnoush, Hydrogen-enhanced fatigue crack growth in a single-edge notched tensile specimen under in-situ hydrogen charging inside an environmental scanning electron microscope, Acta Mater. 170 (2019) 87–99, http://dx.doi.org/10.1016/j.actamat.2019.03.032, URL http://www.sciencedirect.com/science/article/pii/S1359645419301752.

[76] H. Vehoff, P. Neumann, Crack propagation and cleavage initiation in fe-2.6%-si single crystals under controlled plastic crack tip opening rate in various gaseous environments, Acta Metall. 28 (3) (1980) 265–272, http://dx.doi.org/10.1016/0001-6160(80)90161-3.

[77] S. Pu, S. Ooi, Hydrogen transport by dislocation movement in austenitic steel, Mater. Sci. Eng. A (2019) 138059.

[78] C. McMahon Jr, Hydrogen-induced intergranular fracture of steels, Eng. Fract. Mech. 68 (6) (2001) 773–788.

[79] D. Lassila, H. Birnbaum, The effect of diffusive hydrogen segregation on fracture of polycrystalline nickel, Acta Metall. 34 (7) (1986) 1237–1243.

[80] A. Oudriss, J. Creus, J. Bouhattate, E. Conforto, C. Berziou, C. Savall, X. Feaugas, Grain size and grain-boundary effects on diffusion and trapping of hydrogen in pure nickel, Acta Mater. 60 (19) (2012) 6814–6828.

[81] M. Zamanzade, C. Müller, J.R. Velayarce, C. Motz, Susceptibility of different crystal orientations and grain boundaries of polycrystalline ni to hydrogen blister formation, Int. J. Hydrog. Energy 44 (14) (2019) 7706–7714.

[82] A. Tehranchi, W. Curtin, Atomistic study of hydrogen embrittlement of grain boundaries in nickel: I. fracture, J. Mech. Phys. Solids 101 (2017) 150–165.

[83] R. Messmer, C. Briant, The role of chemical bonding in grain boundary embrittlement, Acta Metall. 30 (2) (1982) 457–467.

[84] M. Yamaguchi, M. Shiga, H. Kaburaki, Grain boundary decohesion by impurity segregation in a nickel-sulfur system, Science 307 (5708) (2005) 393–397.

[85] T. Watanabe, The impact of grain boundary character distribution on fracture in polycrystals, Mater. Sci. Eng. A 176 (1–2) (1994) 39–49.

[86] S. Tsurekawa, T. Tanaka, H. Yoshinaga, Grain boundary structure, energy and strength in molybdenum, Mater. Sci. Eng. A 176 (1–2) (1994) 341–348.

[87] A. Akhatova, F. Christien, V. Barnier, B. Radiguet, E. Cadel, F. Cuvilly, P. Pareige, Investigation of the dependence of phosphorus segregation on grain boundary structure in fe-p-c alloy: ross comparison between atom probe tomography and auger electron spectroscopy, Appl. Surf. Sci. 463 (2019) 203–210.

[88] D.H. Lassila, H.K. Birnbaum, Intergranular fracture of nickel: the effect of hydrogen-sulfur co-segregation, Acta Metall. 35 (7) (1987) 1815–1822, http://dx.doi.org/10.1016/0001-6160(87)90127-1, URL http://www.sciencedirect.com/science/article/pii/0001616087901271.

[89] K. Shin, M. Meshii, Effect of sulfur segregation and hydrogen charging on intergranular fracture of iron, in: Perspectives in Hydrogen in Metals, Elsevier, 1986, pp. 693–700.

[90] H. Jarmolowicz, M. Smialowski, Effect of catalytic poisons on the production of nickel hydride by electrolytic charging of nickel with hydrogen, J. Catal. 1 (2) (1962) 165–170.

[91] M. Abd Elhamid, B. Ateya, K. Weil, H. Pickering, Effect of thiosulfate and sulfite on the permeation rate of hydrogen through iron, Corrosion 57 (5) (2001) 428–432.

[92] M. Eberhart, K. Johnson, R. Latanision, A molecular orbital model of intergranular embrittlement, Acta Metall. 32 (6) (1984) 955–959.

[93] M.A. Kappes, Evaluation of Thiosulfate as a Substitute for Hydrogen Sulfide in Sour Corrosion Fatigue Studies (Ph.D. thesis), The Ohio State University, 2011.

[94] S. Asano, R. Otsuka, The lattice hardening due to dissolved hydrogen in iron and steel, Scr. Metall. 10 (11) (1976) 1015–1020.

[95] D.P. Abraham, C.J. Altstetter, The effect of hydrogen on the yield and flow stress of an austenitic stainless steel, Metall. Mater. Trans. A 26 (11) (1995) 2849–2858.

[96] H.K. Birnbaum, P. Sofronis, Hydrogen-enhanced localized plasticity—a mechanism for hydrogen-related fracture, Mater. Sci. Eng. A 176 (1–2) (1994) 191–202.

[97] D. Ulmer, C. Altstetter, Hydrogen-induced strain localization and failure of austenitic stainless steels at high hydrogen concentrations, Acta Metall. Mater. 39 (6) (1991) 1237–1248.

[98] E. Wollan, J. Cable, W. Koehler, The hydrogen atom positions in face centered cubic nickel hydride, J. Phys. Chem. Solids 24 (9) (1963) 1141–1143.

[99] E. Lunarska-Borowiecka, N.F. Fiore, Hydride formation in a ni-base superalloy, Metall. Trans. A 12 (1) (1981) 101–107.

Paper IV: Intergranular Corrosion and Passive Layer Properties of Alloy 725 Modified with Boron and Copper Micro-alloying

Iman Taji[a,*], Tarlan Hajilou[a], Shabnam Karimi[a], Afrooz Barnoush[a,b], Roy Johnsen[a]

[a]Department of Mechanical and Industrial Engineering, Norwegian University of Science and Technology, No. 7491 Trondheim, Norway

[b]Qatar Environment and Energy Research Institute, P.O. Box 34110, Doha, Qatar

Abstract

In this study the effect of B and Cu alloying on corrosion properties of Alloy 725 is investigated. Mod A sample was prepared as a control sample with conventional standard heat treatment. Then two other samples were prepared by adding 250 to 350 ppmw B, named Mod B and Mod C with B content lower than 100 ppm plus 2.3 wt.% Cu. The samples were subjected to intergranular corrosion testing, Mott-Schottky and X-ray photoelectron (XPS) analysis. Intergranular corrosion tests showed continious corrosion at the grain boundaries (GB) in Mod A while Mod C remains completely intact without any corrosion attack. Mod B corroded in the areas around the Mo-rich boride phases formed due to abundant of B element in this alloy. Mod C showed the least defect density in the passive layer while the passive layer of Mod B was thicker. The incorporation of Mo in Mod C was proposed to be responsible for less defect density of Mod C compared to Mod B. Mod A on the other hand had the most defect density and showed higher passive current density in potentiodynamic polarization test.

Keywords

Intergranular corrosion, Mott-Schottky analysis, XPS, Alloy 725, B and Cu addition

This paper is not yet published and is therefore not included

ISBN 978-82-326-6371-2 (printed ver.)
ISBN 978-82-326-5952-4 (electronic ver.)
ISSN 1503-8181 (printed ver.)
ISSN 2703-8084 (online ver.)

NTNU

Norwegian University of
Science and Technology